Mechanism and Function of Nascent Protein Modification in Bacteria

Thesis by

Chien-I Yang

In Partial Fulfillment of the Requirements for
the degree of
Doctor of Philosophy

CALIFORNIA INSTITUTE OF TECHNOLOGY

Pasadena, California

2023

(Defended June 28, 2022)

Chien-I Yang
ORCID: 0000-0001-8606-5013

ACKNOWLEDGMENTS

The past few years at Caltech have been an adventurous and incredible journey. I could not have arrived at this point without the support of numerous people.

First, I would like to thank my Ph.D. advisor, Professor Shu-ou Shan, for her patience, guidance, and unconditional support. She is truly my role model in my scientific career. Her passion and dedication to research inspired me since day one and will continue to do so. I also want to thank my M. Sc. advisor at NTU, Professor Jerry Chun Chung Chan, who encouraged and continues to support me in pursuing research.

I thank my thesis committee, Professor Dennis Dougherty, Professor Linda Hsieh-Wilson, and Professor Alex Varshavsky for their advice and feedback during the committee meetings. Special thanks to Alex, who generously shared many cell strains and plasmids essential to my projects. I want to express my gratitude to the wonderful collaborators, Professor Tsui-Fen Chou, Jeff Jones, and Brett Lomenick, for their tremendous help in the proteomics work.

The people in the Shan lab are not only colleagues but also friends and families. I am thankful for all the advice, support, and company from the current and past Shan lab members that I've worked with: Sowmya Chandrasekar, Meera Rao, George Liang, Camille McAvoy, Un Seng Chio, Yu-Hsien Hwang Fu, Jae Ho Lee, Hyunju Cho, Shuai Wang, Alex Siegel, Hao-Hsuan Hsieh, Yumeng Liu, Zikun Zhu, Arpit Gupta, Jiwoo Kim, and Ruilin Qian. I

treasure every moment spent with them throughout the years. Special thanks to Shuai Wang and Hyunju Cho, the best mentors who introduced me to the essential lab practice and biochemistry techniques that became my precious assets.

I am also grateful for the fruitful discussions with experts from various fields. I thank Professor Tom Miller and Matthew Zimmer for their suggestions on kinetic modeling, Shan Li and Feng Wang for their help in MS sample preparation and data analysis, and Professor Dianne Newman for her insights into bacterial physiology.

I want to thank all my friends who shared the ups and downs of my life in graduate school. I cherish the time I spent at Caltech with Hyunju Cho, Sowmya Chandrasekar, Yu-Hsien Hwang Fu, Zi-Yu Huang, Yun-Ting Cheng, Yu-Li Ni, Chien Han Lin, and all my friends in the Association of Caltech Taiwanese. I enjoy the fantastic get-togethers with Anna Chen, Che-Fan Huang, Jhe-Hao Li, Hua-Chia Tai, Jonathan Lee, Shaking Yao, and Timothy Wang. I am also grateful for the support overseas from Tsai-Yi Hou, Elle Liu, Rosa Chu, Shu-Hao Wan, Chia-An Shen, and Yu-Ting Hsiao.

I thank my aunt Ivy Tseng for her help in my everyday life away from my home country. Finally, my ultimate gratitude goes to my parents, Min-Nan Yang and Li-Chin Tseng, and my brother, Shih-Hung Yang, for their unconditional love and support, as always.

ABSTRACT

Newly synthesized proteins undergo multiple modifications to ensure proper biogenesis and acquire their functions. N-terminal methionine excision (NME), mediated by the sequential actions of peptide deformylase (PDF) and methionine aminopeptidase (MAP), is an essential and the most prevalent N-terminal protein modification in the bacterial proteome. Despite the extensive studies on enzymatic catalysis, how NME impacts various cellular functions and how the enzymes achieve timing and selectivity under complex cellular conditions have been long-standing puzzles.

In this work, we use a combination of biochemical analyses, computational modeling, and *in vivo* measurements to investigate the molecular mechanisms and physiological functions of cotranslational NME reactions. We show that the interactions between the ribosome, the nascent chain, the NME enzymes, and other ribosome-associated protein biogenesis factors dramatically remodel the kinetics and specificity of NME reactions under physiological conditions. In addition, we apply time-resolved, system-wide analyses on the translatome and steady-state proteome to study how the inhibition of PDF influences diverse cellular pathways in bacteria. The results unveil the impact of NME on the biogenesis of nascent proteins and highlight the role of the membrane in coupling the biochemical activities of NME enzymes to cellular physiology.

PUBLISHED CONTENT AND CONTRIBUTIONS

Yang, C.-I., Hsieh, H.-H., Shan, S.-o. (2019). "Timing and specificity of cotranslational nascent protein modification in bacteria." In: *Proc. Natl. Acad. Sci. U.S.A.* 116, pp. 23050–23060. doi: 10.1073/pnas.1912264116.

C.-I.Y. designed research with S.-o.S., performed research, and analyzed data. C.-I.Y. and S.-o.S. wrote the paper.

Yang, C.-I., Kim, J., Shan, S.-o. (2022). "Ribosome-nascent Chain Interaction Regulates N-terminal Protein Modification." In: *Journal of Molecular Biology* 434, pp. 167535. doi: 10.1016/j.jmb.2022.167535.

C.-I.Y. and S.-o-S designed research. C.-I.Y performed research and analyzed data with J.W. and wrote the paper with S.-o.S.

Yang, C.-I., Zhu, Z., Jones, J., Lomenick, B., Chou, T.-F., Shan, S.-o. (2022). "System-wide analyses reveal essential roles of N-terminal protein modification in bacterial membrane integrity" In: *iScience, Accepted*.

C.-I.Y. and S.-o-S designed research. C.-I.Y performed research and analyzed data with Z.Z., J.J., and B.L. and wrote the paper with S.-o.S.

TABLE OF CONTENTS

LIST OF ILLUSTRATIONS AND TABLES

Figures

Tables

Datasets

NOMENCLATURE

ACT. Actinonin.

BMB. 1,4-bismaleimidobutane.

CAM. Chloramphenicol.

CCCP. Carbonyl cyanide m-chlorophenyl hydrazone.

Cm. 7-hydroxycoumaryl ethylglycine.

DAVID. The Database for Annotation, Visualization and Integrated Discovery.

DTT. Dithiothreitol.

EDTA. Ethylenediaminetetraacetic acid.

EMD. Electron microscopy databank.

ETC. Electron transport chain.

FA. Fusidic acid.

FC. Fold change.

fMet. Formylmethionine.

FMT. Formyltransferase.

GO. Gene Ontology.

GRAVY. Grand average of hydropathy.

iMet. Initiator methionine.

IPTG. Isopropyl-β-D-thiogalactoside.

IVT. *in vitro* translation.

LC-MS/MS. Liquid chromatography-tandem mass spectrometry

MAP. Methionine aminopeptidase.

MTT. Methylthiazolyldiphenyl-tetrazolium bromide.

NADPH. Reduced nicotinamide adenine dinucleotide phosphate.

NC. Nascent chain.

NME. N-terminal methionine excision

NTE. N-terminal extension.

OD. Optical density

PDB. Protein data bank.

PDF. Peptide deformylase.

PES. Phenazine ethosulfate.

PMSF. Phenylmethylsulfonyl fluoride.

POI. Protein of interest.

RNC. Ribosome-nascent chain complex.

ROS. Reactive oxygen species.

RPB. Ribosome-associated protein biogenesis factor.

RPM. Reads per million.

S.D. Standard deviation.

SD. Shine-Dalgarno sequence.

SDS-PAGE. Sodium dodecyl sulfate–polyacrylamide gel electrophoresis.

SDS. Sodium dodecyl sulfate.

SEM. Standard error of the mean.

SILAC. Stable isotope labeling by amino acids in cell culture.

SRP. Signal recognition particle.

SUMO. Small Ubiquitin-like Modifier.

TCA cycle. Tricarboxylic acid cycle.

TCA. Trichloric acetic acid.

TCEP. Tris(2-carboxyethyl) phosphine.

TF. Trigger factor.

TFA. Trifluoroacetic acid.

THF. Tetrahydrofolate.

ThT. Thioflavin T.

TLC. Thin layer chromatography.

TMD. Transmembrane domain.

TMR. Tetramethylrhodamine.

TMT. Tandem mass tag.

Ub. Ubiquitin.

Chapter 1

INTRODUCTION

Proteins accomplish the majority of cellular functions. Upon the emergence from the ribosome exit, newly synthesized proteins undergo multiple maturation steps, collectively termed protein biogenesis (Kramer et al., 2019). N-terminal methionine excision (NME), a ubiquitous protein modification conserved in all kingdoms of life, is among the earliest protein biogenesis events encountered by nascent proteins (Giglione et al., 2004). NME is essential for cell viability in bacteria and implicated in multiple cellular functions in higher eukaryotes, including mitochondria activity, angiogenesis, and cell cycle (Giglione et al., 2004; Griffith et al., 1998; Hu et al., 2006; Li and Chang, 1995; Mazel et al., 1994). As a result, NME has become an important target for developing antibiotics and cancer therapeutics.

In bacteria, where the protein synthesis is initiated with a formylated methionine (fMet), NME is mediated by the sequential actions of peptide deformylase (PDF) and methionine aminopeptidase (MAP), two enzymes that act on over 90% and 50% of the bacterial proteome, respectively (Bienvenut et al., 2015; Giglione et al., 2004; Solbiati et al., 1999). For decades, extensive studies of the structures and enzymology of PDF and MAP have provided rich information on their catalytic mechanisms. However, how NME takes

place in the complex cellular context and impacts various cellular functions have been outstanding questions in the field.

Emerging evidence shows that NME, along with a multitude of protein biogenesis processes, begins early while the nascent protein is still being synthesized (Kramer et al., 2019). In Chapters 2 and 3, we investigate the mechanistic details of NME on the ribosome. We used a combination of biochemical analyses and computational modeling to demonstrate that the ribosome enables rapid association of MAP with the nascent chain, allowing efficient methionine excision of optimal substrates within a biologically relevant time scale. The crowded environment at the ribosome tunnel exit, at which other protein biogenesis factors bind, selectively limits the processing time window for suboptimal substrates during the continuous translation elongation, ensuring the specificity of NME on nascent proteins. Moreover, the ribosome actively regulates NME by specific interactions with a subset of hydrophobic nascent polypeptides, leading to the retention of fMet on a significant fraction of membrane proteome. Together, the work provides an excellent example of how specificity and speed are balanced in an enzymatic reaction, which is intricately regulated by the associated macromolecular environment via multiple mechanisms.

Despite the absolute requirement for cell viability, the physiological roles of NME have been elusive. In Chapter 4, we applied time-resolved, system-wide analyses on the translatome and steady-state proteome to investigate how PDF inhibition impacts diverse

cellular pathways in bacteria. Upon the treatment by a PDF inhibitor, the cells rapidly induced protein folding and membrane stress responses at the membrane, followed by the remodeling of the membrane proteome and the perturbation of various metabolic pathways involved in redox homeostasis. The results provide direct evidence for the role of NME in the proper biogenesis of nascent proteins and strongly suggest that NME inhibition directly targets the plasma membrane, which couples the NME-linked protein biogenesis defects to cellular metabolism. Our work thus clarifies the link between the biochemical activity of PDF and its physiological significance and reveals the functional impact of a ubiquitous N-terminal protein modification.

N-terminal modifications constitute a significant branch of protein biogenesis, and how specific modifications impact protein functions and cellular physiology has only recently started to be explored. The work in this dissertation unravels the mechanisms and functions of a ubiquitous cellular pathway and contributes to the comprehensive understanding of the functional roles of N-terminal protein modifications.

Chapter 2

TIMING AND SPECIFICITY OF COTRANSLATIONAL NASCENT PROTEIN MODIFICATION IN BACTERIA

A version of this chapter was first published as: Yang, C.-I., Hsieh, H.-H., Shan, S.-o. (2019). "Timing and specificity of cotranslational nascent protein modification in bacteria." In: *Proc. Natl. Acad. Sci. U.S.A.* 116, pp. 23050–23060. doi: 10.1073/pnas.1912264116.

The nascent polypeptide exit site of the ribosome is a crowded environment where multiple ribosome-associated protein biogenesis factors (RPBs) compete for the nascent polypeptide to influence their localization, folding, or quality control. Here we address how N-terminal methionine excision (NME), a ubiquitous process crucial for the maturation of over 50% of the bacterial proteome, occurs in a timely and selective manner in this crowded environment. In bacteria, NME is mediated by two essential enzymes: peptide deformylase (PDF) and methionine aminopeptidase (MAP). We show that the reaction of MAP on ribosome-bound nascent chains approaches diffusion-limited rates, allowing immediate methionine excision of optimal substrates after deformylation. Specificity is achieved by kinetic competition of NME with translation elongation and by regulation from other RPBs, which selectively narrow the processing time window for suboptimal substrates. A

mathematical model derived from the data accurately predicts cotranslational NME efficiency in the cytosol. Our results demonstrate how a fundamental enzymatic activity is reshaped by its associated macromolecular environment to optimize both efficiency and selectivity, and provides a platform to study other cotranslational protein biogenesis pathways.

2.1. Introduction

Emerging evidence shows that protein biogenesis begins early, while the nascent protein is still being synthesized by the ribosome. As a nascent polypeptide emerges from the ribosome tunnel exit, a variety of ribosome-associated protein biogenesis factors (RPBs) bind at overlapping docking sites near the tunnel exit and compete for the nascent protein to influence its folding, localization, maturation, and quality control (Bhakta et al., 2019; Bornemann et al., 2014; Kramer et al., 2009, 2019). Efficient and accurate selection of nascent proteins into their proper biogenesis pathways is crucial, but how this is achieved in the crowded environment of the ribosome exit site is not well understood.

N-terminal methionine excision (NME) is an essential and ubiquitous process conserved across all kingdoms of life. NME generates essential functional groups for some enzymes (Bearne, 1996; Brannigan et al., 1995; Kim et al., 1996) and introduces diverse N-termini for cellular proteins to enable their quality control via the N-degron pathways (Nguyen et al., 2019; Varshavsky, 2011, 2019). In eukaryotic cells, NME also allows

subsequent N-terminal modifications such as N-acetylation, which can serve as a degron to enable protein quality control (Hwang et al., 2010; Shemorry et al., 2013), and N-myristoylation, which enables localization of the protein to membrane compartments for participation in signal transduction pathways (Giglione et al., 2015; Gordon et al., 1991). In bacteria and prokaryote-derived organelles, where protein synthesis initiates with formyl methionine, NME is carried out by two essential enzymes: peptide deformylase (PDF) and methionine aminopeptidase (MAP). Over 90% of the proteome in bacteria is deformylated, while ~50% of the proteins are subject to methionine excision (Giglione et al., 2015). Classic enzymological studies of PDF and MAP, based on short peptide substrates, provided rich information on the NME process (Frottin et al., 2006; Hu et al., 1999; Ragusa et al., 1999; Xiao et al., 2010). Deformylation by PDF is required for methionine excision by MAP (Solbiati et al., 1999). PDF displays relaxed sequence specificity except for the initiator methionine (Hu et al., 1999; Ragusa et al., 1999), whereas MAP strongly favors substrates with small amino acid side-chains at the second position (Boissel et al., 1988; Frottin et al., 2006; Hirel et al., 1989; Xiao et al., 2010). These results were corroborated by studies in cell lysate and *in vivo* (Bienvenut et al., 2015; Boissel et al., 1988; Hirel et al., 1989), providing useful tools for the qualitative prediction of NME (Frottin et al., 2006; Martinez et al., 2008; Meinnel and Giglione, 2008). Nevertheless, the MAP reactions on peptide substrates are slow, with k_{cat}/K_m values of ~10^3–10^5 $M^{-1}s^{-1}$ even for optimal substrates (Frottin et al., 2006),

raising questions as to how cotranslational NME could occur effectively for ~50% of the proteome.

NME is one of the earliest events encountered by nascent proteins during their biogenesis and could occur cotranslationally as soon as the nascent chain reaches 44–48 residues (Sandikci et al., 2013). Earlier works have demonstrated the interaction between the ribosome and the NME enzymes in bacteria and eukaryotes (Bhakta et al., 2019; Bornemann et al., 2014; Fujii et al., 2018; Ranjan et al., 2017; Raue et al., 2007; Sandikci et al., 2013). Recent measurements showed that *E. coli* PDF and MAP bind the ribosome with apparent equilibrium dissociation constants (K_d) of 1.8 μM and 2.4 μM, respectively (Bingel-Erlenmeyer et al., 2008; Sandikci et al., 2013). Ribosome binding of PDF is mediated by its C-terminal helix, which docks in a groove between uL22 and bL32 near the ribosome exit site (Bhakta et al., 2019; Bingel-Erlenmeyer et al., 2008). The same site also mediates ribosome binding of MAP via a positively charged loop at the periphery of the active site (Fig. S2.1 and (Bhakta et al., 2019; Sandikci et al., 2013)). Disruption of the ribosome interactions of PDF or MAP led to inefficient NME in cell extract and defective cell growth, suggesting the importance of the ribosome interaction for enzymatic activity (Bingel-Erlenmeyer et al., 2008; Sandikci et al., 2013). However, whether and how the ribosome influences the NME reactions of the nascent protein was only recently explored for PDF (Ranjan et al., 2017) and remains elusive for MAP.

In addition to MAP and PDF, multiple other RPBs also engage newly synthesized proteins near the ribosome exit site. In bacteria, these include the Signal recognition particle (SRP) and the SecA ATPase that mediate the cotranslational targeting of membrane and secretory proteins (Akopian et al., 2013; Huber et al., 2011; Singh et al., 2014; Rawat et al., 2015; Wang et al., 2017), and trigger factor (TF) that cotranslationally chaperones numerous cytosolic, secretory, and outer membrane proteins (Deuerling et al., 1999; Fedyukina and Cavagnero, 2011; Beck et al., 2000; Oh et al., 2011). The binding sites of the RPBs overlap heavily with one another on the ribosome (Fig. S2.1 and (Kramer et al., 2009, 2019)). SRP binds free ribosomes at uL23 and uL29 near the ribosome exit site (Gu et al., 2003; Schaffitzel et al., 2006) and, upon the emergence of a transmembrane domain (TMD) or signal sequence on the nascent polypeptide, further contacts bL32, uL22, and uL24, resulting in substantial overlaps with the PDF and MAP binding sites (Bhakta et al., 2019; Bingel-Erlenmeyer et al., 2008; Schaffitzel et al., 2006). The TF binding site on the ribosome spans uL22, uL23, and uL29, which partially overlaps with those of SRP, PDF, and MAP (Bhakta et al., 2019; Ferbitz et al., 2004). SecA also contacts the ribosome via uL23 (Huber et al., 2011; Singh et al., 2014), where both SRP and TF can bind. The molecular crowding at the ribosome exit necessitates spatial and temporal coordination between the multiple RPBs, which must compete for not only ribosome-binding but also access to the nascent polypeptide.

Recent works began to explore the interplay between the RPBs at the crowded ribosome exit site. Excess PDF or MAP reduces the ribosome occupancy of one another (Sandikci et al., 2013). On the other hand, a recent structural study showed that PDF and MAP can co-bind at the ribosome, with MAP relocalizing to a secondary binding site near uL23 and uL29 in the presence of PDF (Bhakta et al., 2019). Pairwise co-binding has also been observed for TF and SRP with one another and with PDF or MAP on the ribosome and ribosome-nascent chain complex (RNC) (Ariosa et al., 2015; Bhakta et al., 2019; Bornemann et al., 2014). In addition, TF modestly reduced NME efficiency *in vivo* and *in vitro* (Oh et al., 2011; Sandikci et al., 2013), and SRP slows the deformylation of RNCs bearing a TMD or a hydrophobic signal sequence on the nascent chain *in vitro* (Ranjan et al., 2017). These results demonstrate the ability of RPBs to influence the activity of one another. Finally, the PDF reaction became slower when the nascent chain elongates from 75 to 100 amino acids (Ranjan et al., 2017), and TF strongly inhibited SRP function when the nascent polypeptide exceeds a critical length (Ariosa et al., 2015). These observations suggest that translation elongation could act as a competing branch that limits the action of individual RPBs. Nevertheless, how the crowded environment at the ribosome exit site and competition with ongoing protein synthesis impact the timing, activity, and selectivity of nascent protein modification remains an outstanding question.

In this work, we combined pre-steady-state kinetic measurements and numerical simulations to address these questions. We showed that the MAP reaction on ribosome-

bound nascent chains is 2–4 orders of magnitude faster than previously measured on peptide substrates, allowing the NME for optimal substrates to occur upon each encounter of MAP with the translating ribosome. TF and SRP are critical for ensuring the specificity of nascent protein modification, by selectively narrowing the window for the reactions of MAP on suboptimal substrates during translation. Our experimental data allowed the construction of a computational model for cotranslational NME that accurately predicts the cotranslational NME efficiency of model substrates under near *in vivo* conditions.

2.2. Results

MAP reaction on ribosome-bound nascent chains is diffusion-limited.

To characterize the NME reactions in the context of ribosomes, we generated and purified translation-arrested RNCs displaying FtsQ, an inner membrane protein with a 27-residue N-terminal extension (NTE) preceding its TMD. The unstructured NTE minimizes potential effects of nascent chain folding on enzymatic processing, and the N-terminal sequence of FtsQ (MSQAA) is predicted to be favored by both PDF and MAP (Hu et al., 1999; Frottin et al., 2006). A C-terminal 8-amino acid translation stall sequence, Ms-sup1 (Yap and Bernstein, 2009), allows generation of RNCs with defined nascent chain lengths (Fig. 2.1A and Fig. S2.2A). ^{35}S-Met-labeled RNCs were generated by *in vitro* translation in E. coli S30 extract in the presence of actinonin (ACT), a PDF inhibitor, to prevent NME by endogenous PDF and MAP, and purified by sucrose-gradient centrifugation.

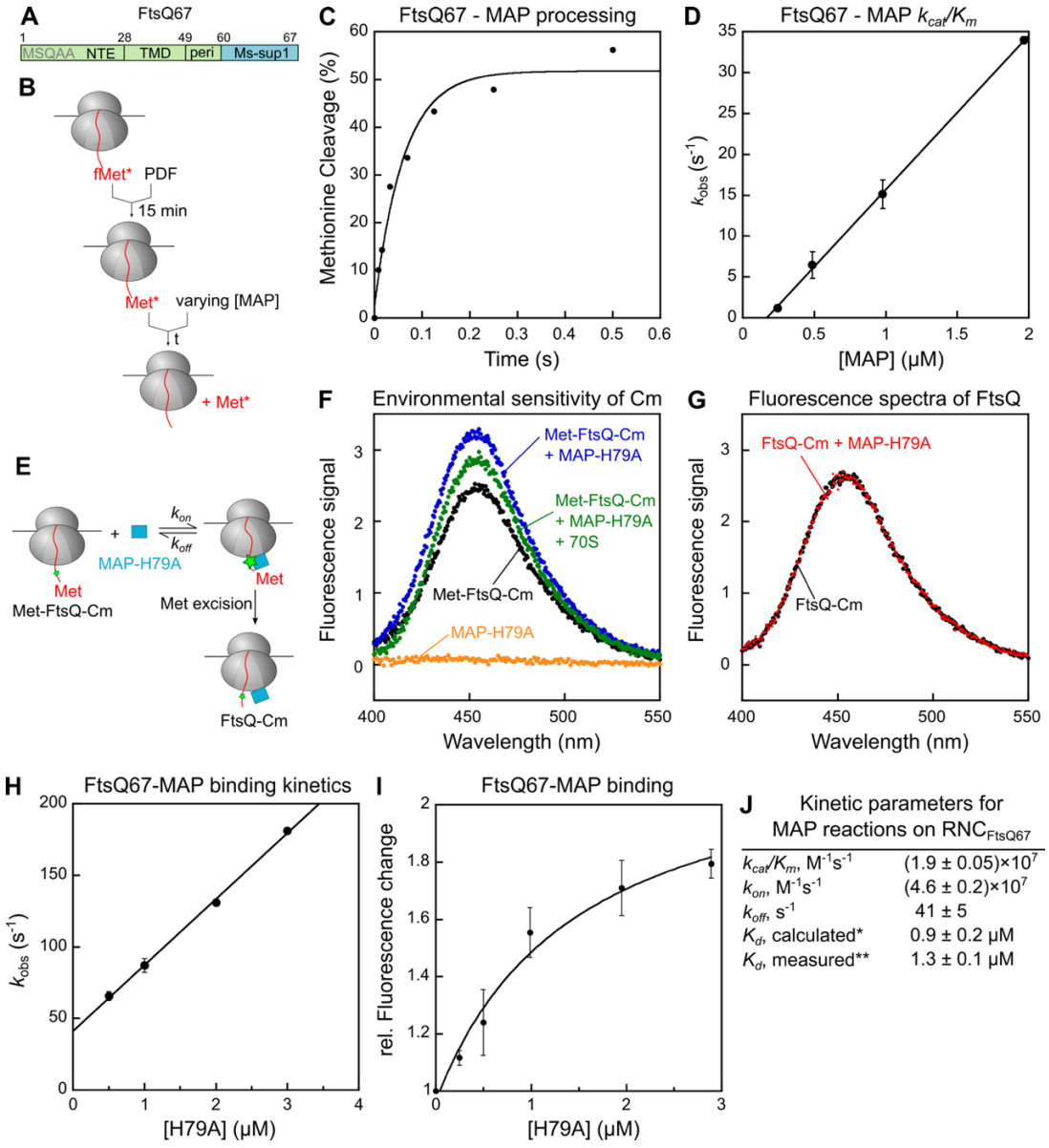

Figure 2.1. MAP-mediated methionine excision of nascent chains on the ribosome is diffusion-limited.

(A) Scheme of the model substrate FtsQ67 for generation of RNC, which contains the N-terminal extension (NTE), transmembrane domain (TMD), and part of the periplasmic region (peri) followed by the Ms-sup1 translation stall sequence. The N-terminal sequence

is indicated. **(B)** Scheme of the methionine cleavage assay to measure the rate constant of the MAP reaction. Purified RNC with a single ^{35}S-labeled N-terminal methionine was pre-incubated with PDF for 15 minutes, before initiation of reaction by addition of MAP. Reactions contained 10 nM RNC, 50 nM PDF, and varying concentrations of MAP. **(C)** A representative time trace for cleavage of 10 nM $RNC_{Met\text{-}FtsQ67}$ by 1 μM MAP. Single exponential fit of the data (Eq. 1 in the Methods) gave a k_{obs} value of 16.4 s^{-1}. **(D)** The observed rate constants for methionine cleavage of $RNC_{Met\text{-}FtsQ67}$ were plotted as a function of effective MAP concentration. The line is a linear fit of the data, and the obtained k_{cat}/K_m value is summarized in panel (J). (E) Scheme of the fluorescence-based assay to measure the binding between $RNC_{Met\text{-}FtsQ67}^{Cm}$ and MAP. The FtsQ67 nascent chain was labeled with coumarin (Cm) at the fifth residue. (F) Fluorescence emission spectra to demonstrate the enhancement of Cm fluorescence upon binding of $RNC_{Met\text{-}FtsQ67}^{Cm}$ to MAP-H79A. Where indicated, reactions contained 8 nM deformylated $RNC_{Met\text{-}FtsQ67}^{Cm}$, 0.5 μM MAP-H79A, and 1.4 μM 70S ribosome. (G) MAP-H79A does not affect the fluorescence emission spectra of RNC_{FtsQ67}^{Cm} after methionine excision. $RNC_{Met\text{-}FtsQ67}^{Cm}$ was pre-treated with 20 nM wild-type MAP to yield RNC_{FtsQ67}^{Cm}, and fluorescence emission spectra were recorded before and after the addition of 0.5 μM MAP-H79A. (H) Observed rate constants (k_{obs}) of RNC-MAP association, measured using the fluorescence assay in (E), was plotted as a function of MAP-H79A concentration. The reactions contained 8 nM $RNC_{Met\text{-}FtsQ}^{Cm}$ and indicated concentrations of MAP-H79A. The line is a linear fit of the data to Eq. 6 in the Supplementary Methods, and the obtained k_{on} and k_{off} values are summarized in panel (J). (I) Equilibrium titration to measure the binding affinity of $RNC_{Met\text{-}FtsQ}^{Cm}$ for MAP-H79A. The data was fit to Eq. 4 in the Supplementary Methods, and the obtained K_d value is summarized in (J). (J) Summary of the kinetic parameters obtained from the measurements in (D), (H), and (I). *: calculated from $K_d = k_{off}/k_{on}$. **: K_d measured from the equilibrium titration in panel (I). All values are reported as mean ± S.D., with n = 2.

We first measured methionine cleavage by MAP on RNC_{FtsQ} with a nascent chain length of 67 residues (Figs. 2.1B–D). As deformylation is a pre-requisite for the MAP reaction, we pre-incubated RNC_{FtsQ67} with PDF to ensure complete removal of the formyl group on ^{35}S-labeled N-terminal methionine. We then carried out the reaction under single turnover conditions with purified MAP in excess of RNC_{FtsQ67}, and quantified the reaction extent at indicated times by scintillation counting of free ^{35}S-methionine released from the

nascent chain (Gottesman et al., 1998). The reaction rate rises linearly up to 2 μM MAP with no indication of saturation, giving estimated limits for K_m of >>2 μM and k_{cat} of >>34 s^{-1}. The MAP concentration dependence of the observed rate constants gave a k_{cat}/K_m value of $(1.9 \pm 0.05) \times 10^7$ $M^{-1}s^{-1}$. Measurements on RNC bearing luciferase, a cytosolic protein with an unstructured N-terminus, gave a comparable k_{cat}/K_m value of $(1.9 \pm 0.06) \times 10^7$ $M^{-1}s^{-1}$ (Fig. S2.2B). These rate constants on RNC substrates are 10^2–10^4 fold faster than those on peptide substrates (k_{cat}/K_m values of 10^3–10^5 $M^{-1}s^{-1}$) measured here (Fig. S2.2C) and previously (D'Souza V and Holz, 1999; Frottin et al., 2006; Xiao et al., 2010). The MAP-K226E mutation, which weakens the binding of MAP to the ribosome (Sandikci et al., 2013), reduced the reaction rate of RNC_{FtsQ67} ~20-fold but affected the reaction of a tetra-peptide substrate <2-fold (Figs. S2.2C and D), supporting an important contribution of the ribosome in enhancing the efficiency of the MAP reaction (Sandikci et al., 2013).

The k_{cat}/K_m value of the MAP reaction on RNC substrates approaches the rate constants of protein associations, suggesting that this reaction follows Briggs-Haldane kinetics where the reaction is rate-limited by enzyme-substrate association (Fersht, 1998). To test this model, we developed a fluorescence-based assay to directly measure the binding of MAP and RNC_{FtsQ} (Fig. 2.1E). To specifically probe the interaction between MAP and the substrate, we used mutant MAP-H79A, which reduced the rate of the chemical step >10^4-fold but has only minor effects on the binding of peptide substrates (Lowther et al., 1999; Watterson et al., 2008) and the 70S ribosome (Figs. S2.2E–G). A fluorescent amino acid, 7-

hydroxycoumaryl ethylglycine (Cm), was incorporated at the fifth residue of the FtsQ nascent chain via amber suppression (Saraogi et al., 2011). Binding of MAP-H79A led to enhanced fluorescence intensity of RNC_{FtsQ}^{Cm}. The addition of excess ribosome reduced the fluorescence enhancement, in agreement with the competition of ribosomes with RNC for MAP binding (Fig. 2.1F). Importantly, removal of the N-terminal methionine on the nascent chain abolished the MAP-induced fluorescence enhancement of the Cm dye (Fig. 2.1G). This demonstrates that the fluorescence enhancement is specific to the interaction of MAP with the uncleaved nascent chain, and suggests that the nascent chain is released from the substrate-binding pocket of MAP after methionine excision.

Using this fluorescence assay, we measured the observed rate constants for MAP-RNC_{FtsQ67} assembly as a function of MAP-H79A concentration. Linear fit of the concentration dependence gave an association rate constant, k_{on}, of $(4.6 \pm 0.2) \times 10^7$ $M^{-1}s^{-1}$ and an extrapolated dissociation rate constant, k_{off}, of 41 ± 5 s^{-1} (Fig. 2.1H). The value of k_{on} is comparable to the value of k_{cat}/K_m measured from the enzymatic reaction, supporting the model that the MAP reaction is rate-limited by the assembly of the MAP-RNC complex. Independent equilibrium titrations using the fluorescence assay gave an equilibrium dissociation constant (K_d) of 1.3 ± 0.1 μM for the MAP-RNC_{FtsQ67} complex, in good agreement with the K_d value of 0.9 ± 0.2 μM calculated from k_{off} / k_{on} (Figs. 2.1I and J). Considering the sub- to low-millimolar K_m values of MAP for peptide substrates (D'Souza V and Holz, 1999; Frottin et al., 2006) and the apparent K_d value of 2.4 ± 0.4 μM for MAP-

ribosome binding (Sandikci et al., 2013), these results indicate that MAP-RNC binding is dominated by interaction with the ribosome, with a modest contribution from the nascent chain.

Collectively, the results in this section showed that the MAP reaction for nascent proteins on the ribosome is substantially accelerated compared to peptide substrates and is rate-limited by the association between MAP and RNC for optimal substrates such as RNC_{FtsQ67}. The diffusion-controlled kinetics implies that MAP can successfully process nascent chains on the RNC upon every encounter and thus ensures efficient NME of nascent proteins.

The PDF reaction is rate-limiting for NME of optimal substrates.

To measure PDF-mediated deformylation, the prerequisite for methionine excision, we designed two independent assays that use methionine excision as the readout. In the Actinonin-quench assay, we quenched the PDF reaction at specified times using actinonin, and released the deformylated methionine with excess MAP for quantification (Fig. 2.2A). In the coupled assay, limiting PDF and excess MAP were added simultaneously to initiate the reaction (Fig. 2.2B); this assay leverages the faster kinetics of the MAP than the PDF reaction and was only used for RNCs bearing optimal MAP substrates. The results from the two assays agreed well (Fig. 2.2D) and together, the two assays allowed us to measure the kinetics of the PDF reaction on a variety of substrates.

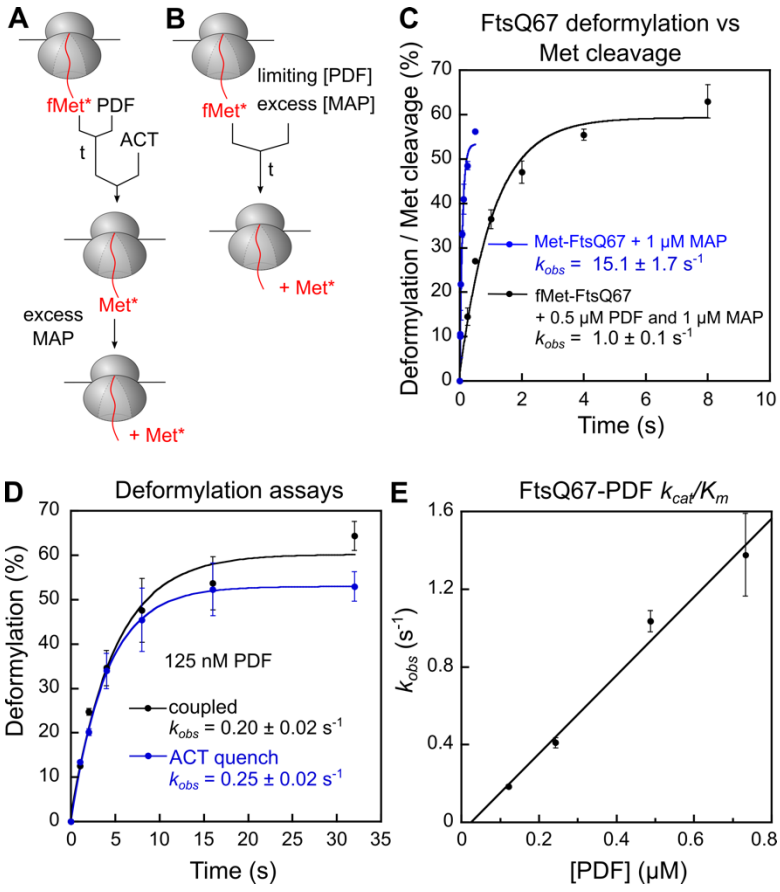

Figure 2.2. The PDF reaction is ~10-fold slower than the MAP reaction.

(A) Scheme of the Actinonin-quench based deformylation assay. The reaction was initiated by adding PDF to $RNC_{fMet\text{-}FtsQ67}$ and quenched with 40 μM actinonin at specified time points. MAP (100 nM for FtsQ-S2) was added thereafter to cleave the deformylated N-terminal methionine, allowing the reaction to be analyzed via scintillation counting of free ^{35}S-methionine. **(B)** Scheme of the coupled deformylation assay. Indicated concentrations of PDF was added together with excess MAP (1 μM) to initiate NME of 10 nM $RNC_{fMet\text{-}FtsQ67}$, and the generation of free ^{35}S-methionine was monitored during the time course. **(C)** Comparison of the time courses for methionine excision of $RNC_{fMet\text{-}FtsQ67}$, measured using the coupled deformylation assay in (B), with that of deformylated $RNC_{Met\text{-}FtsQ67}$ by MAP. **(D)** Comparison of the PDF reaction time courses measured by the coupled assay (black) and Actinonin-quench assay (blue). The reactions used 10 nM $RNC_{fMet\text{-}FtsQ67}$, 125 nM PDF, and 1 μM and 100 nM MAP in the coupled and Actinonin-quench assay, respectively. The data were fit to Eq. 1 in the Methods, and the obtained rate constants are indicated. **(E)**

Observed rate constants for deformylation of $RNC_{fMet\text{-}FtsQ67}$ are plotted as a function of effective PDF concentration. Linear fit of the data gave a k_{cat}/K_m value of $(2.0 \pm 0.4) \times 10^6$ $M^{-1}s^{-1}$. All values are shown as mean ± S.D., with n = 2–3.

The observed methionine cleavage in the coupled PDF-MAP reaction with formylated RNC_{FtsQ} was >10-fold slower than the MAP reaction with deformylated RNC_{FtsQ67} (Fig. 2.2C), suggesting that deformylation is rate-limiting in the coupled reaction. Varying the concentration of MAP from 0.5 to 2 μM did not affect the observed reaction rates (Fig. S2.2H), providing an independent indication that the MAP reaction is not rate-limiting in the coupled assay. Using the coupled assay, the k_{cat}/K_m value for deformylation of RNC_{FtsQ67} was measured to be $(2.0 \pm 0.4) \times 10^6$ $M^{-1}s^{-1}$ (Fig. 2.2E), in good agreement with previous measurements by Ranjan et al. (Ranjan et al., 2017). These values are ~10-fold lower than that of the MAP reaction, indicating that deformylation is the rate-limiting step for the overall NME of optimal MAP substrates.

Compromised specificity of NME with nascent proteins on the ribosome.

A prominent determinant of NME efficiency is the second residue on the nascent polypeptide (Bienvenut et al., 2015; Boissel et al., 1988; Frottin et al., 2006; Hirel et al., 1989; Xiao et al., 2010). To test whether and how the ribosome modulates second residue specificity of NME, we prepared $RNC_{FtsQ67\text{-}X2}$ in which Ser2 on the FtsQ nascent chain is mutated to different amino acids. Consistent with previous *in vivo* observations and *in vitro* studies using peptide substrates (Bienvenut et al., 2015; Ragusa et al., 1999), PDF remained

insensitive to the second residue among all the RNC substrates tested, except for a moderate 3-fold rate reduction with $RNC_{FtsQ67\text{-}N2}$ (Fig. 2.3A).

In contrast to PDF, proteomics studies and previous kinetic measurements based on peptide substrates showed that the MAP reaction depends critically on the size of the second residue. Peptides with medium-sized side chains at the second residue (T, V) define a 'twilight zone' that display k_{cat}/K_m values 10^2 and 10^3 fold lower, respectively, than those of optimal substrates (G, A, S, P, C), and substrates with even larger second residues (N, K, R, etc.) reacts $>10^5$ fold more slowly ((Frottin et al., 2006) and Fig. 2.3B, magenta). In contrast to the observations with peptide substrates, the impact of second residues on the MAP reaction was substantially smaller for RNC substrates. Compared to optimal substrates such as $RNC_{FtsQ67\text{-}A2}$ and $RNC_{FtsQ67\text{-}S2}$, the k_{cat}/K_m value was comparable with $RNC_{FtsQ67\text{-}T2}$ and reduced only 10-fold with $RNC_{FtsQ67\text{-}V2}$ (Fig. 2.3B). $RNC_{FtsQ67\text{-}N2}$, previously considered a very weak substrate, was still processed by MAP with a k_{cat}/K_m of $\sim 10^5$ $M^{-1}s^{-1}$ (Fig. 2.3B).

The reduced specificity of the MAP reaction for RNCs can be attributed to the diffusion-limited nature of this reaction. As described in Figure 2.1, the reaction of MAP with optimal substrates is rate-limited by its association with RNC, which would mask reductions in the rate of subsequent peptide bond hydrolysis. The slower rate of deformylation than methionine excision is expected to further reduce the specificity of overall NME. This is because modest rate reductions in the MAP reaction would be masked

as long as the PDF reaction is rate-limiting, and the MAP reaction becomes rate-limiting only for substrates with second residues larger than valine (cf. k_{cat}/K_m values in Fig. 2.3B, dark bars versus Fig. 2.2E). Both of these factors are expected to severely compromise the specificity of the NME reaction for nascent chains on the ribosome.

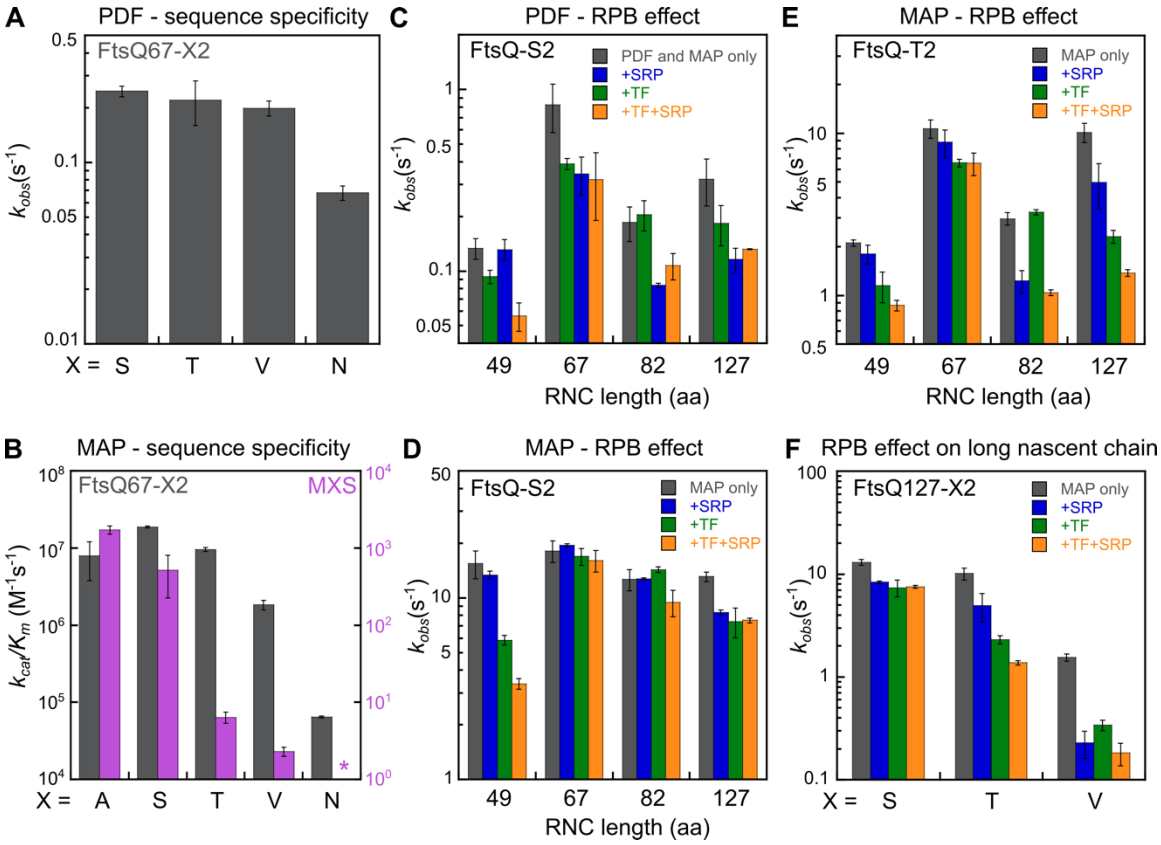

Figure 2.3. Compromised second residue specificity of the NME reactions on RNCs is restored by length-dependent regulation from the RPBs.

(A) Observed deformylation rate constants of $RNC_{fMet\text{-}FtsQ67}$ with indicated amino acids at the second residue. Reactions were measured using the Actinonin-quench assay (Fig. 2.2A) and contained 0.125 μM PDF. To release the deformylated methionine, 100 and 250 nM MAP were used for FtsQ-S2/T2 and FtsQ-V2/N2, respectively. **(B)** Comparison of MAP

specificity towards the second residue for reactions with $RNC_{FtsQ67\text{-}X2}$ (gray bars) versus tripeptide substrates (MXS, magenta bars; replotted from Frottin *et al* (Frottin et al., 2006)). The k_{cat}/K_m values for $RNC_{FtsQ67\text{-}X2}$ were measured as in Fig. 2.1D. The asterisk denotes a k_{cat}/K_m value of <0.01 $M^{-1}s^{-1}$ for the MNS peptide. **(C), (D)** Effects of TF and SRP on the deformylation (C) and methionine cleavage (D) of RNCs bearing FtsQ-S2 nascent chains of the indicated lengths. Observed PDF rate constants were measured with 10 nM RNCs and 0.5 μM PDF using the coupled assay. Observed MAP rate constants were measured with 10 nM RNCs and 1 μM MAP. **(E), (F)** Effects of TF and SRP on methionine cleavage of RNCs bearing FtsQ-T2 nascent chains of the indicated lengths (E) and RNCs bearing FtsQ-127 nascent chains with the indicated second residue side chains (F). Observed rate constants were measured with 10 nM RNCs, 1 μM MAP, and 5 μM TF and 400 nM SRP where indicated. All values are shown as mean ± S.D., with n = 2–3.

Nascent chain length and RPBs define an optimal window for NME to restore specificity.

We reasoned that two factors could help restore the specificity of cotranslational NME. First, on actively translating ribosomes, NME must kinetically compete with elongation of the nascent polypeptide; this could impose a limited time window for NME if the reactions of these enzymes are sensitive to nascent chain length. Second, additional RPBs such as TF, SRP, and SecA are recruited to the ribosome exit site during translation and could modulate the reaction kinetics of the NME enzymes.

In vitro translation of stalled RNCs in cell extracts showed that the minimum nascent chain length required for NME is ~45 residues (Figs. S2.3A, B), in agreement with previous reports (Sandikci et al., 2013) and with the predicted distances between the exit site and the actives sites of PDF and MAP (~35 and ~30 Å, respectively; (Bingel-Erlenmeyer et al., 2008; Sandikci et al., 2013)). To define the optimal window for NME, we performed single-

turnover measurements of the PDF and MAP reactions on purified RNCs with different nascent chain lengths. The k_{cat}/K_m value for the PDF reaction of $RNC_{FtsQ\text{-}S2}$ rose 20-fold when the nascent chain elongates from 45 to 67 amino acids, and became 2-3 fold slower at longer nascent chain lengths (Fig. S2.3C and Fig. 2.3C, grey bars). The MAP reaction varied <2-fold beyond a nascent chain length of 49 residues for an optimal substrate, $RNC_{FtsQ\text{-}S2}$ (Fig. S2.3D and Fig. 2.3D, grey bars), but became more sensitive to nascent chain length for substrates in the 'twilight zone', $RNC_{FtsQ\text{-}T2}$ and $RNC_{FtsQ\text{-}V2}$ (Fig. 2.3E, gray bars and Fig. S2.3E). Thus, both the PDF and MAP reactions showed modest dependences on nascent chain length, and for MAP, this length dependence is larger for suboptimal substrates.

To test the effect of RPBs, we measured the length-dependent reactions of PDF and MAP in the presence of saturating concentrations of TF (Fig. S2.4A) and SRP. The combination of TF and SRP largely reproduced the effect of the cytosol on the MAP reaction, and the additional presence of SecA had minimal effects on both reactions (Figs. S2.4B and C). The PDF reaction was slowed ~2-fold across all the tested nascent chain lengths by the combination of both factors (Fig. 2.3C, orange bars). A previous work reported a much larger inhibitory effect of SRP on the PDF reaction with membrane proteins (Ranjan et al., 2017), because the TMD or signal sequence was much closer to the N-termini of the substrates used in that study compared to FtsQ, in which the TMD is preceded by a 27 amino acid NTE. In contrast to PDF, the effects of RPBs on the MAP reactions are larger and more substrate-dependent. For an optimal substrate ($RNC_{FtsQ\text{-}S2}$), SRP and TF reduced the rate of the MAP

reaction 5-fold when the nascent chain is short (49 amino acids), but affected the reaction <2-fold at longer nascent chain lengths (Fig. 2.3D). For a suboptimal substrate, $RNC_{FtsQ\text{-}T2}$, SRP and TF together slowed the MAP reaction ~3-fold at both short (49 residues) and intermediate (82 residues) nascent chain lengths, and ~10-fold when the nascent chain reached 127 amino acids (Figs. 2.3E and F). The inhibitory effects of SRP and TF on methionine excision of both short and long nascent chains were also observed with an SRP-independent cytosolic protein, luciferase (Fig. S2.5). Finally, the inhibitory effect of TF or SRP on long-chain RNCs was larger with an even slower MAP substrate, FtsQ-V2 (Fig. 2.3F). Thus, RPBs selectively inhibit the MAP reaction on long nascent chains for RNCs bearing suboptimal MAP substrates.

Together, the results in this section show that the reactions of both PDF and MAP on the RNC are sensitive to the length of the nascent polypeptide, generating an optimal window for NME when the nascent chain is 49–82 amino acids long. For the MAP reaction, this window is largely imposed by the action of RPBs, which selectively inhibits methionine excision on suboptimal MAP substrates (Figs. 2.3D–F) and therefore contributes to the restoration of NME specificity.

A kinetic model for cotranslational NME emphasizes the contribution of RPBs to NME specificity.

To quantitatively understand how the multiple factors that modulate the activity of NME enzymes impact the cotranslational N-termini modification of nascent proteins, we constructed an analytical kinetic model (Fig. 2.4A). Modeling of cotranslational NME in cell lysate is enabled by several features of this assay that simplifies its mathematical description. First, ribosomes translating the reporter protein are at much lower concentrations compared to the NME enzymes in the lysate, rendering the reaction single turnover and directly comparable to the single-turnover rate constants measured using purified RNCs. In addition, the concentration of NME enzymes are ~10-fold lower than their K_d values for the ribosome and therefore sub-saturating. This allows the NME reaction at a given nascent chain length to be described by pseudo-first-order rate constants for deformylation (k^{PDF}) and methionine excision (k^{MAP}; Table S2.1) based on the experimentally determined or extrapolated k_{cat}/K_m values and enzyme concentrations determined by quantitative western blot analyses in the E. coli lysate (Fig. S2.6). The effect of ongoing protein synthesis is described by an estimated rate constant of translation elongation (k_{trans}). Based on differential equations constructed from this model, we used numerical integration to simulate the cumulative fraction of nascent proteins of n residues that successfully undergo deformylation and methionine excision (Figs. S2.7A–D). The robustness of the kinetic model was tested by applying an experimental error of 20% in enzyme concentrations and reaction rate constants, which were randomly selected from normal distributions. The resulting deviations in simulation results were ~10% (error bars in Figs. S2.7A–D), confirming the reliability of the simulation.

We first asked how fast NME occurs during translation. Simulation based on the kinetic model showed that NME is 90% complete for FtsQ-S2 before ~150 amino acids are synthesized (Fig. S2.7A). As expected from the ~10-fold faster reaction with MAP than with PDF for this substrate, methionine excision closely followed deformylation (Fig. S2.7A). When the second residue is threonine and valine, methionine excision increasingly lagged behind deformylation (Figs. S2.7B and C). When the second residue is asparagine, deformylation was 90% complete when the nascent chain reached 250 amino acids, but no significant methionine excision occurred (Fig. S2.7D). Notably, the MAP reaction profiles of both FtsQ-T2 and FtsQ-V2 exhibited biphasic behavior, with a steep rise before the nascent chain reached ~80 residues followed by a slow phase (Figs. S2.7B and C), owing to the inhibition of MAP reactions at longer nascent chain lengths. Thus, the MAP reaction becomes increasingly rate-limiting for overall NME with increasing size of the second residue.

To dissect the contributions of different factors to the efficiency of cotranslational NME, we further tested whether and how the simulation outcome is sensitive to variations in the individual parameters in the kinetic model (Figs. 2.4, B–E and Fig. S2.8). The tested parameters include the translation rate (solid red lines) and the concentrations of MAP or PDF (solid black and blue lines), which affect the enzymatic reaction rates at all nascent chain lengths. The sensitivity test revealed a strong influence of translation elongation rate on NME efficiency (Figs. 2.4, B–E, red lines and Figs. S2.8, A–D), because faster translation

shortens the time window available for the actions of PDF and MAP. This effect is substantial for all the substrates tested and emphasizes the kinetic rivalry between NME and nascent chain synthesis.

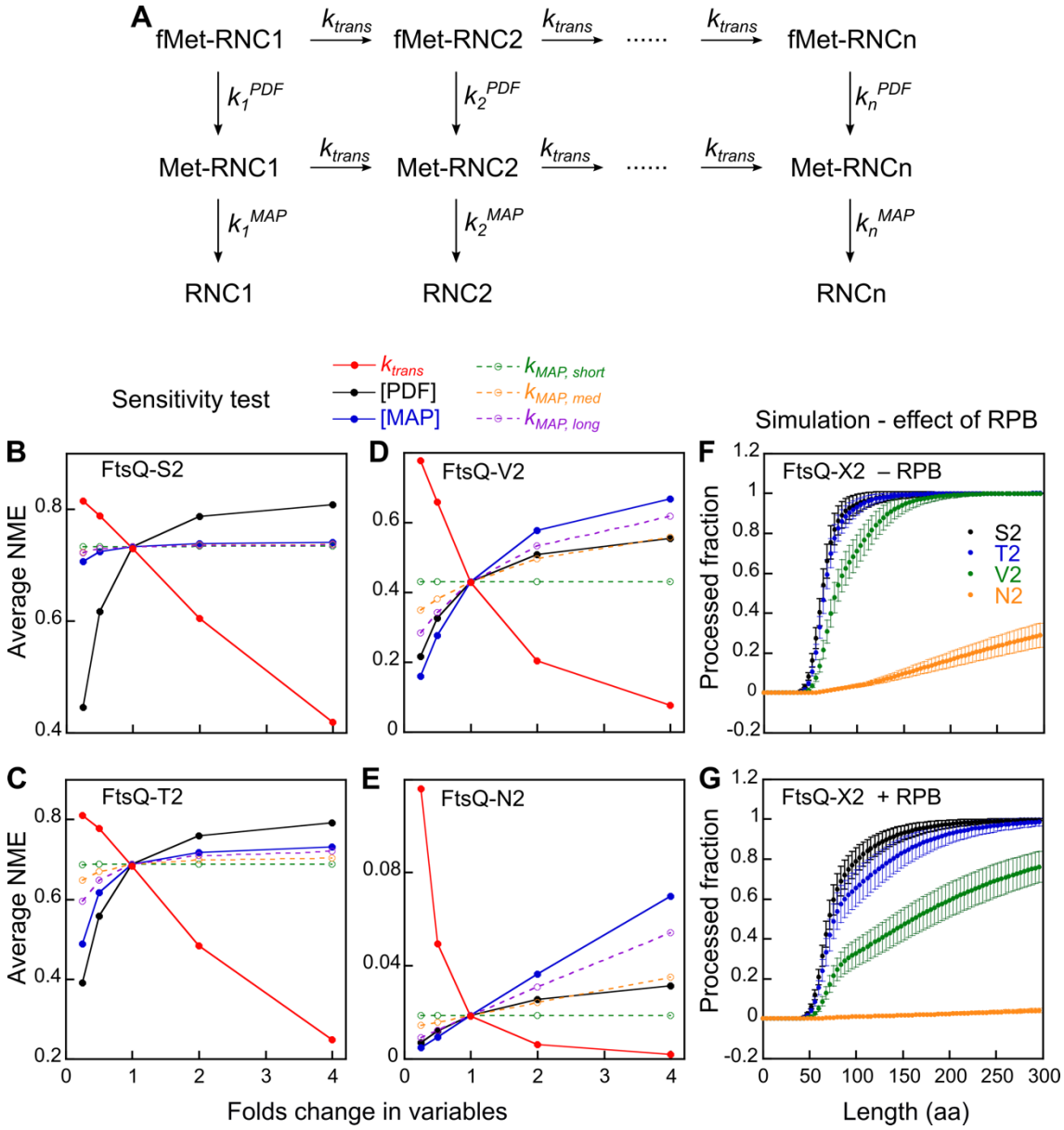

Figure 2.4. A kinetic model simulates cotranslational NME during protein synthesis. **(A)** A kinetic model for the cotranslational NME of a nascent protein with *n* amino acids. k_{trans} is the translation elongation rate. The PDF and MAP rate constants at nascent chain length *i* (k_i^{PDF} and k_i^{MAP}) are the products of effective enzyme concentration and k_{cat}/K_m values and, unless otherwise indicated, are also modulated by RPBs. The parameters used in the simulation are summarized in Table S2.1. **(B)–(E)** Sensitivity test of the simulation results for FtsQ-X2. Each indicated parameter was varied independently by 2^{-2} – 2^2 folds of the value in Table S2.1. "Average NME' denotes the mean value for the fraction of methionine-cleaved nascent chains throughout the reaction profile before 300 residues are synthesized. **(F), (G)** Simulated cotranslational NME profiles for RNC_{FtsQ} with different second residue side chains in the absence (F) and presence (G) of the regulatory effects of RPBs. Results from 100 runs were shown as mean ± S.D.

On the other hand, the sensitivity of cotranslational NME to changes in enzyme concentration is substrate-dependent (Figs. 2.4, B–E, black and blue lines and Fig. S2.8E–L). The NME efficiency of the optimal substrate, FtsQ-S2, is significantly affected only by reductions in PDF concentration (Figs. 2.4B and S1.8E, I). For suboptimal substrates such as FtsQ-T2, FtsQ-V2 and FtsQ-N2, NME efficiency can be modulated by changes in both PDF and MAP levels in both directions, and the MAP concentration becomes more dominant in dictating NME efficiency with increasing size of the second residue on the nascent chain (Figs. 2.4C–E and Figs. S2.8F–H, J–L). These results reinforce the notion that the rate-limiting step of cotranslational NME shifted from the PDF to the MAP reaction, as predicted from Figs. S2.7A–D. As the MAP reaction is dependent on nascent chain length, we individually varied the MAP reaction rates for RNCs with short (45–56 residues), medium (56–82 residues), and long (>82 residues) nascent chains (Figs. 2.4B–E, dashed lines). The

simulation results showed that tuning $k_{MAP,long}$ had the largest effect on NME efficiency, and this effect is specific to FtsQ-V2 and FtsQ-N2.

Finally, we tested whether and how the RPBs, which reduce the MAP reaction rates in a substrate-dependent manner when the nascent chain exceeds 82 amino acids, impact the cotranslational NME profile (Figs. 2.4F–G). The simulation results showed that the presence of RPBs moderately delayed the cotranslational NME of FtsQ-S2, which can be attributed to the 2-fold global effect of RPBs on the PDF reaction rate (Fig. 2.3C). On the other hand, the slow phase during the cotranslational processing of FtsQ-T2 and FtsQ-V2 becomes more prominent in the presence of RPBs, resulting in significantly delayed processing of FtsQ-T2 and incomplete NME of FtsQ-V2 for nascent chains up to 300 residues in length. These predictions are consistent with a previous study, which observed an inhibitory effect of TF on the cotranslational NME of barnase in cell lysate (Sandikci et al., 2013). By integrating the NME reaction kinetics with translation elongation, the kinetic model demonstrated how the presence of other RPBs improves the specificity of NME.

Cotranslational NME in cell extracts agrees with predictions from kinetic simulation.

To experimentally test the predictions from the kinetic model, we designed a cotranslational NME assay to measure the extent of NME during active translation. We fused the N-terminal extension and TMD of FtsQ to thioredoxin (TrxA), an unrelated E. coli cytosolic protein (Fig. 2.5A). *In vitro* translation of this 171 amino acid reporter protein in

the E. coli S30 extract allowed us to assess its cotranslational NME by endogenous PDF and MAP in the presence of RPBs (Fig. 2.5B). The extent of NME was monitored by SDS-PAGE and autoradiography analyses of substrates labeled with a single ^{35}S-methionine at the N-terminus. Substrates with Ser and Thr at the second residue showed >80% NME (Fig. 2.5C). In contrast, over half of FtsQ-V2-TrxA retained the N-terminal ^{35}S-methionine, and FtsQ-N2-TrxA was resistant to NME (Fig. 2.5C). These data agreed well with the simulation results for the individual substrates (Fig. 2.5D).

Another prediction from the kinetic model is that the extent of NME is sensitive to the length of the protein, especially at 50–100 amino acids where NME products accumulate quickly (Fig. 2.4). To test this prediction, we varied the length of the reporter protein by truncating or removing thioredoxin (Fig. 2.5A). In agreement with predictions from the simulation, the extent of NME for substrates with Thr and Val at the second residue reduced with shorter protein length (Figs. 2.5E and F). Finally, we tested the prediction that NME is sensitive to translation elongation rate by using fusidic acid (FA), which binds to EF-G and attenuates translation elongation (Dai et al., 2017; Okura et al., 1971). Increasing amount of fusidic acid inhibited the translation of FtsQ-V2-TrxA while giving rise to more efficient NME (Figs. 2.5G and H). The increase of overall NME from ~50% to ~80% was in good agreement with the simulation results for this substrate (cf Figs. 2.5H and 2.4D), and supports the notion that slower elongation provides a longer time window for the reactions of PDF and MAP.

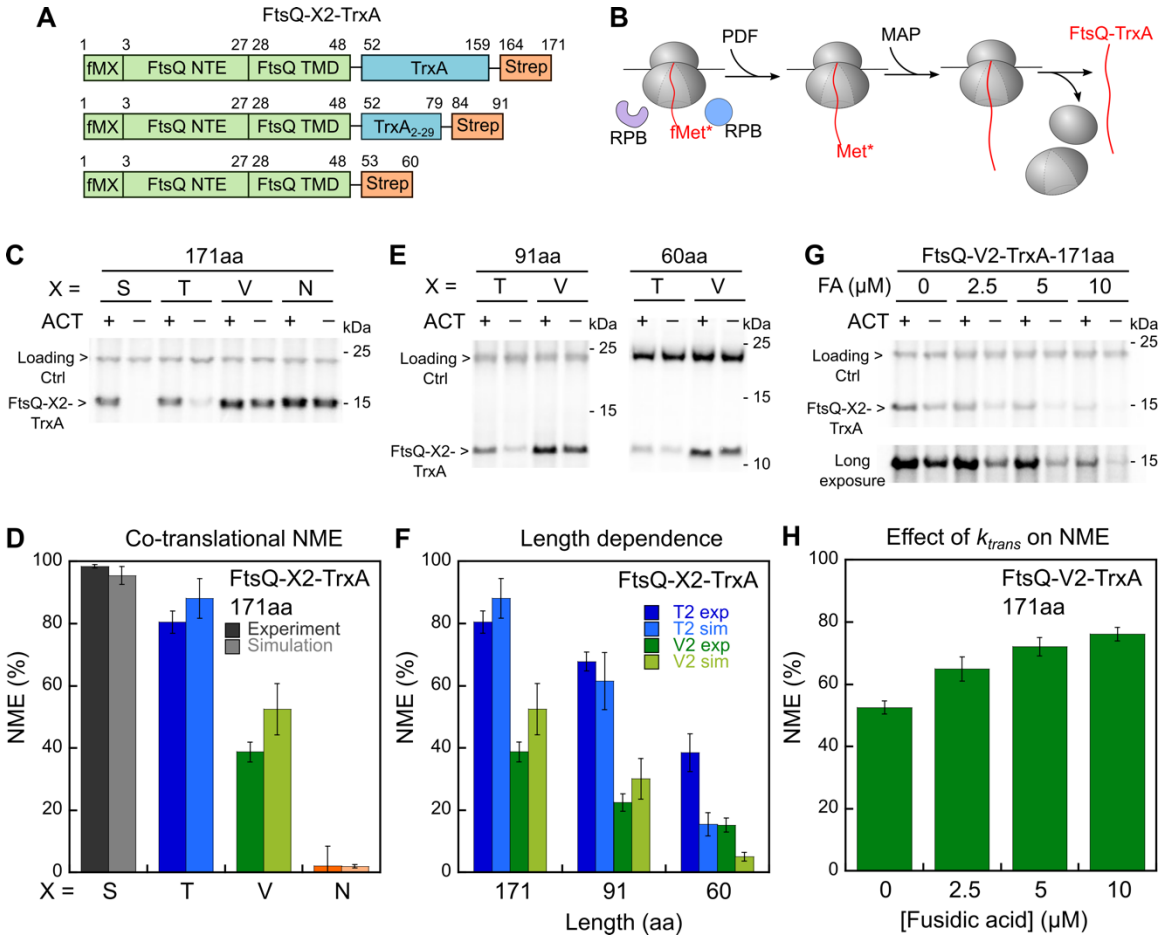

Figure 2.5. Measurement of cotranslational NME in cell lysate reproduces predictions from kinetic simulations.

(A) Scheme of the model substrates used in the cotranslational NME assay. The 171 amino acid reporter protein contains full-length thioredoxin (TrxA), and the 60 amino acid reporter contains no thioredoxin. To generate the reporter with 91 residues, 80 residues were removed from the C-terminus of thioredoxin. **(B)** Scheme of the cotranslational NME assay. FtsQ-X2-TrxA was translated in the S30 extract and processed by endogenous PDF and MAP during translation. **(C)** Representative SDS-PAGE and autoradiography analysis of the cotranslational NME of FtsQ-X2-TrxA (171 aa) in the S30 extract, measured as depicted in (B). The reactions with actinonin (ACT, 5 μM) provide controls for the intensity of the FtsQ-X2-TrxA band without NME. **(D)** NME efficiency for FtsQ-X2-TrxA (171 aa) bearing different second-site residues. The values are from quantification of the data in (C)

and their replicates (dark colors). The simulated data are from Fig. 2.4G at a nascent chain length of 171 aa (light colors). **(E)** Representative SDS-PAGE and autoradiograph of the cotranslational NME of shorter reporter proteins, measured as depicted in (B). The second site residues are indicated. **(F)** Summary of the cotranslational NME efficiency for FtsQ-T2-TrxA (dark blue) and FtsQ-V2-TrxA (dark green) with different lengths. The values are from quantification of the data in (C), (E) and their replicates. The simulated data (light blue and light green bars) are from Fig. 2.4G at the corresponding nascent chain lengths. **(G)** Representative SDS-PAGE and autoradiograph of cotranslational NME of FtsQ-V2-TrxA (171 aa) with indicated amount of fusidic acid (FA), which inhibits translation elongation. **(H)** Quantification of the data in (G) and their replicates. All values are reported as mean ± S.D., with n = 3.

In conclusion, the results from the cotranslational NME assay agreed well with the predictions from the computational model, suggesting that kinetic modeling based on rate constants measured with translation-arrested RNCs provides an accurate description of cotranslational NME in the complex cytosolic environment.

2.3. Discussion

The majority of newly-synthesized proteins undergo multiple maturation steps to ensure their proper function, localization, and turnover. As one of the earliest modification events during protein biogenesis, NME takes place in the crowded environment of the ribosome exit site where multiple other RPBs compete for access to the nascent polypeptide. In this work, kinetic analyses demonstrate that NME is actively regulated by the ribosome, nascent chain length, and other RPBs at the ribosome tunnel exit. These factors, together with kinetic competition with translation elongation, dictate the efficiency, timing, and specificity of NME. Our results shed light on how the RPBs coordinate at the ribosome exit

and demonstrate how a fundamental enzymatic reaction can be profoundly reshaped by its macromolecular environment. Moreover, our work provides a useful framework to conceptualize other cotranslational protein biogenesis events.

Our results show that the MAP reactions on RNCs are accelerated 102–104 fold compared to reactions with peptide substrates. This rate enhancement is likely due to the micromolar-affinity MAP binding site provided by the ribosome, which is ~102–103-fold tighter than the affinity of MAP for peptides (D'Souza V and Holz, 1999; Frottin et al., 2006). This interaction increases the local concentration of MAP and possibly pre-orients MAP to facilitate its access to the nascent chain, allowing methionine excision to proceed in a diffusion-limited manner for optimal substrates. Together with the rapid MAP-RNC association kinetics, over 90% of the nascent protein can be processed before ~150 amino acids are synthesized under physiologically-relevant conditions. However, the enhanced efficiency comes with a tradeoff in specificity, as any reductions in intrinsic reactivity would be masked by other steps that are rate-limiting, such as MAP-ribosome binding and deformylation (Fig. 2.6A). We found here that specificity is restored by other RPBs at the ribosome exit site, which selectively attenuate MAP reactions on suboptimal substrates when the nascent chain exceeds 82 amino acids. This imposes a limited time window on the NME of suboptimal substrates during translation, thus effecting their rejection (Fig. 2.6B and Fig. 2.6A, dashed lines). These results exemplify the trade-off between efficiency and specificity

in biological systems, and reveal an unexpected role of the crowded environment at the ribosome exit in optimizing the balance between these two key parameters.

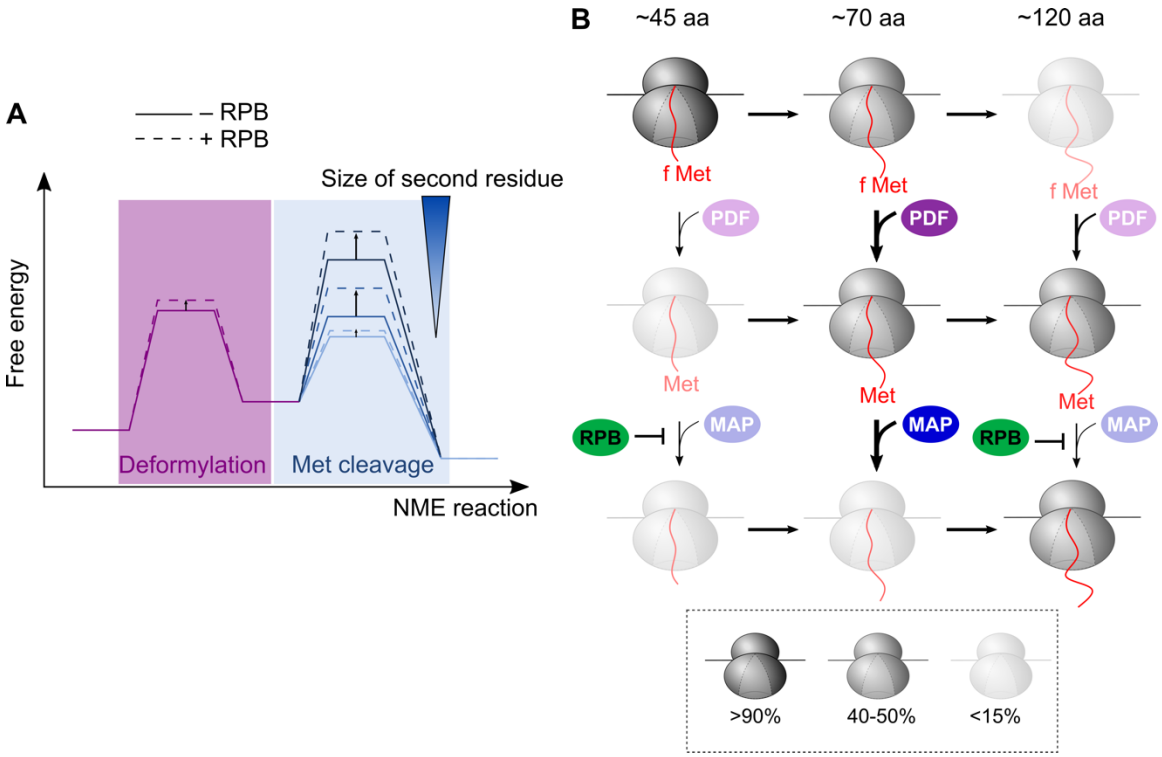

Figure 2.6. Model for cotranslational NME mediated by PDF and MAP.

(A) Free energy profiles to depict the change in rate-limiting step during cotranslational NME, due to both the sequence specificity of MAP and regulation by RPBs. As the second residue on the nascent protein becomes larger, the rate-limiting step shifts from deformylation to methionine cleavage. The RPBs moderately slows the PDF reaction, but significantly and selectively reduces the rates of the MAP reaction for substrates with larger second residue side chains. **(B)** RPBs define an optimal window for NME during translation. The relative abundance of individual ribosomal species at each nascent chain length was simulated during the cotranslational NME of FtsQ-V2 using the mathematical model and depicted using the indicated coloring scheme. PDF and MAP can act on the nascent proteins as soon as 45 residues are translated. PDF has an intrinsic preference for

substrates of ~70 residues in length (second row). The optimal window for the reaction of MAP is similar, but is imposed by the effects of RPBs (third row).

The results here also illustrate multiple mechanisms by which the RPBs coordinate in time and space at the ribosome exit site to ensure the proper functions of one another. First, given previous observations that TF and SRP can co-bind with MAP or PDF on the ribosome (Bornemann et al., 2014; Sandikci et al., 2013), the regulation observed here likely occurs allosterically rather than through exclusion of NME enzymes from the ribosome. This regulation could involve repositioning of these enzymes on the ribosome by TF or SRP that changes the access or orientation of the nascent chain relative to the enzyme active site. This model is consistent with the observation that the regulatory effects of TF and SRP on the MAP reaction are substrate-specific, whereas MAP-RNC binding is dominated by interaction with the ribosome. Second, TF regulates both NME enzymes when nascent proteins are as short as 49 amino acids. Given the enrichment of TF on nascent proteins longer than 100 amino acids in ribosome profiling data (Oh et al., 2011), our observation suggests that TF can begin regulating protein biogenesis before it stably engages with nascent polypeptides. Third, TF and SRP regulate the MAP reaction both when the nascent polypeptide is short (49 residues) and long (127 residues), but not at intermediate chain lengths (67 residues). This suggests a remarkable degree of dynamics in the interplay between RPBs, which can adjust their relative positioning and/or accessibility to the nascent chain during translation. Most importantly, the length- and substrate-dependent regulation of

RPBs defines an optimal time window for NME during translation and helps enhance its specificity, as discussed above. Analogous ‘timing’ mechanisms that enhance fidelity was also observed between SRP with TF (Ariosa et al., 2015; Bornemann et al., 2014), and could provide a general and effective mechanism to coordinate the different cotranslational biogenesis pathways.

Analogous to previous computational models that describe cotranslational protein folding (Ciryam et al., 2013; O’Brien et al., 2012, 2014), the kinetic model described here demonstrates how multiple parameters together contribute to NME, including enzyme concentration, nascent chain length, rivalry with translation elongation, and regulation by RPBs. Our simulation successfully predicted the NME efficiency of model substrates during active translation in cell extracts, as well as regulation of NME by the rates and duration of translation, demonstrating that the computational model derived from measurements on translation-arrested RNCs faithfully recapitulates cotranslational nascent protein modification by the NME enzymes. This model further predicts additional layers of control over NME that await to be tested, such as changes in the cellular level or activity of PDF during environmental changes (Somerville et al., 2003; Wilkins et al., 2001), SRP-induced inhibition of deformylation on nascent chains with TMDs or signal sequences close to the N-terminus (Ranjan et al., 2017), and diverse factors that regulate translation elongation, including codon usage, translation stall sequences, and small molecule ligands that regulate this stalling (Buskirk and Green, 2017; Rodnina, 2016; Seip and Innis, 2016). Importantly,

quantitative kinetic measurements coupled to computational modeling under physiologically relevant conditions provide a powerful approach to elucidate how cotranslational protein biogenesis occurs in the crowded and complex cellular environment, and may be useful for understanding other biochemical pathways.

2.4. Materials and Methods

Plasmid and strain construction

The expression vector pET28a was used for the cloning of PDF, MAP, MAP-H79A, and MAP-HA. MAP-H79A contains a cleavable N-terminal $(His)_6$-SUMO tag and a C-terminal GLPATGG extension, which does not affect the activity of MAP. For *in vitro* transcription and translation of RNCs, DNA sequences coding the FtsQ or luciferase nascent chains were subcloned via Gibson cloning (Gibson et al., 2009) into pUC19 containing T7 promoter and the ribosome-binding site (Norrander et al., 1983; Schaffitzel and Ban, 2007). The Ms-sup1 stalling sequence was fused to the C-termini of nascent chain sequences via Fastcloning (Li et al., 2011). For the cotranslational NME assay, DNA fragments coding thioredoxin-fusion proteins were cloned into the pK7 plasmid (Jewett and Swartz, 2004) between the T7 promoter and T7 terminator using Gibson cloning. To construct the strain harboring C-terminal HA tagged MAP for preparation of S30 extract, the genomic MAP in KC6 (A19 ΔendA met+ ΔtonA ΔspeA ΔtnaA ΔsdaA ΔsdaB ΔgshA (Calhoun and Swartz, 2006)) was modified using λ-red recombination (Datsenko and Wanner, 2000).

Protein expression and purification

PDF was purified as described (Ragusa et al., 1998). Briefly, BL21 star (DE3) cells (Invitrogen) at OD_{600} = 0.5 were induced with 0.5 mM IPTG at 30 °C for 4 h, and lysed by sonication in buffer A (50 mM Hepes-KOH and 20 mM $NiSO_4$, pH 7.5) containing ProBlock Gold protease inhibitor cocktail (GoldBio). Clarified lysate was dialyzed overnight against buffer A. After ultracentrifugation for 30 min at 55,000 rpm, 4 °C in a Ti 70 rotor (Beckmann Coulter), the supernatant was loaded onto MonoQ 10/100 GL (GE Healthcare) equilibrated with buffer B (50 mM Hepes-KOH, 10% glycerol and 5 mM $NiSO_4$, pH 7.5) and eluted with a linear gradient of 0–500 mM KCl. Fractions containing single PDF band were collected and dialyzed against buffer C (50 mM Hepes-KOH, 100 mM NaCl, and 0.2 mM $CoCl_2$, pH 7.5) before storage at –80 °C.

Wild-type MAP, MAP-K226E, and MAP-HA were purified as described (Frottin et al., 2006). BL21 star (DE3) cells at OD_{600} = 0.6 were induced with 0.5 mM IPTG at 30 °C for 3 h, and lysed by sonication in buffer D (50 mM Hepes-KOH, 10% glycerol and 0.2 mM $CoCl_2$, pH 7.5) containing protease inhibitor. Protein in clarified lysate was precipitated with 0–80% ammonium sulfate. The pellet was resuspended with buffer D, dialyzed overnight against buffer D, and loaded onto Q Sepharose Fast Flow column (GE Healthcare). For wild-type MAP and MAP-K226E, proteins were eluted with buffer C and further purified with MonoQ 10/100 GL using a linear gradient of 0–200 mM NaCl. Purified proteins were

supplemented with 20% glycerol before storage at –80 °C. MAP-HA was eluted from Q Sepharose with a linear gradient of 0–500 mM NaCl, and fractions containing purified proteins were supplemented with 20% glycerol and stored at –80 °C.

To express MAP-H79A, BL21 star (DE3) cells at OD_{600} = 0.6 were induced with 0.5 mM IPTG at 30 °C for 3 h, and lysed by sonication in buffer D containing protease inhibitor. Clarified cell lysates were loaded onto Ni-NTA equilibrated with buffer E (50 mM Hepes-KOH, 500 mM NaCl, 10% glycerol and 20 mM imidazole, pH 7.5). Proteins were eluted with buffer F (50 mM Hepes-KOH, 150 mM NaCl, 10% glycerol and 500 mM imidazole, pH 7.5), incubated with His_6-Ulp1protease and dialyzed overnight against buffer G (50 mM Hepes-KOH, 50 mM NaCl, 10% glycerol, pH 7.5). Tag-free proteins were passed through Ni-NTA, and further purified with MonoQ using a linear gradient of 0–200 mM NaCl. Purified proteins were supplied with 0.2 mM $CoCl_2$ and 20% glycerol before storage in –80 °C.

RNC purification

Radiolabeled RNCs were generated by *in vitro* translation in *E. coli* S30 extract supplemented with ^{35}S-Met as described previously (Saraogi et al., 2011). In brief, plasmids coding for nascent peptide sequence were transcribed and translated in 0.5 mL of mixture containing 12 mM magnesium glutamate, 10 mM ammonium glutamate, 175 mM potassium glutamate, 1.2 mM ATP, 0.86 mM each of GTP, CTP, and UTP, 34 μg/mL folinic acid, 0.17

mg/mL *E. coli* tRNA (Roche), 2 mM each of amino acids except methionine, 10 μM methionine, 0.44 μM ^{35}S-methionine, 33 mM phosphoenolpyrovate, 0.33 mM β-nicotinamide adenine dinucleotide, 0.26 mM CoA, 2.7 mM sodium oxalate, 1.5 mM spermidine, 1 mM putrescine, 4 μM anti-ssr1 oligonucleotide, 28% (vol/vol) S30 extract, 5 μM actinonin, and 2 μM T7 RNA polymerase, pH 7.8, at 30 °C for 1.5 h. The reaction was loaded onto a 40 mL sucrose gradient (10–50% sucrose in 50 mM Hepes-KOH, 500 mM KOAc, 100 mM $Mg(OAc)_2$, 0.1% Triton X-100, 1 μM actinonin, and 1 mM TCEP, pH 7.5) and centrifuged for 15 h at 23,000 rpm, 4 °C in a SW32 Ti rotor (Beckmann Coulter). Monosome fractions were collected and centrifuged for 2 h at 100,000 rpm, 4 °C in a TLA 100.3 rotor (Beckmann Coulter). Pellets were washed and dissolved in assay buffer (50 mM Hepes-KOH, 150 mM KOAc, 10 mM $Mg(OAc)_2$, and 1 mM TCEP, pH 7.5), and stored at –80 °C. To prepare Cm-labeled RNCs, 75 μM Cm, 12 μM RF1 aptamer, and 12 μM coumarine synthetase were included in the translation reaction, methionine was increased to 2 mM, and ^{35}S-methionine was omitted. The nascent peptide concentrations were determined by scintillation counting or fluorescence measurement. For the RNC used in this study, 7–15% of the ribosomes contained the nascent peptide.

RNC NME assays

Methionine cleavage assay. Pre-steady state kinetic measurements were carried out under single-turnover condition using an RQF-3 Quench-flow instrument (KinTek). To

remove the formyl group prior to measuring methionine cleavage, 20 nM RNC labeled with a single ^{35}S methionine at the N-terminus was incubated with PDF (100 nM) in assay buffer (50 mM Hepes-KOH, 150 mM KOAc, 10 mM $Mg(OAc)_2$, and 1 mM TCEP, pH 7.5) with 0.1 mM $CoCl_2$ at room temperature for at least 15 min. The reaction was initiated by rapidly mixing deformylated RNC with an equal volume of MAP solution at varying concentrations, and quenched with 10% TCA at specified time points. Quenched reactions were centrifuged at 18,000 g, 4 °C for 10 min to precipitate the proteins. The supernatant containing released ^{35}S-methionine was subjected to scintillation counting for quantification. The amount of free methionine was normalized against the total amount of nascent chain, and the data was fit to Eq. 1,

$$\frac{[Met]}{[RNC]_0} = C(1 - e^{-k_{obs}t}) \quad (1)$$

where k_{obs} is the observed rate constant, and C is the maximum fraction of RNC that can be processed.

Coupled deformylation assay. 20 nM RNC labeled with a single ^{35}S methionine at the N-terminus was rapidly mixed with an equal volume of enzyme solution containing 2 μM MAP and varying concentrations of PDF. The reaction was quenched with 10% TCA and quantified as described above.

ACT-quench deformylation assay. 20 nM RNC labeled with a single ^{35}S methionine at the N-terminus was mixed with varying concentrations of PDF to initiate the reaction. For substrates FtsQ-S2 and FtsQ-T2, the reaction was quenched with 40 μM of ACT at specified times, and the deformylated methionine on the nascent chain was released by incubation with 0.1 μM MAP for 10 s. For FtsQ-V2 and FtsQ-N2, 80 μM ACT was used to quench the reaction, followed by a 5 min incubation with 0.25 μM MAP. The reaction was quenched with 10% TCA and quantified as described above.

Kinetic analysis. To determine the kinetic parameters under single-turnover conditions, the following enzymatic reaction scheme was considered:

$$E + S \underset{k_{-1}}{\overset{k_1}{\rightleftharpoons}} E \bullet S \xrightarrow{k_2} E \bullet P$$

The expression for the observed rate constant of the reaction (k_{obsd}) at a given enzyme concentration was derived using the Cleland method (Cleland, 1975):

$$k_{obsd} = \frac{k_2[E]}{\frac{k_{-1} + k_2}{k_1} + [E]} = \frac{k_{cat}[E]}{K_M + [E]} \tag{2}$$

where $k_{cat} = k_2$, $K_M = \frac{k_{-1}+k_2}{k_1}$, and $k_{cat}/K_m = \frac{k_1 k_2}{k_2+k_{-1}}$. Under k_{cat}/K_m conditions, [E] $\rightarrow$ 0, which gives us:

$$k_{obsd} = \frac{k_1 k_2}{k_2 + k_{-1}}[E] = k_{cat}/K_m[E] \quad (3)$$

k_{cat}/K_m was obtained from a linear fit of k_{obs} values against effective enzyme concentration (see next paragraph) at sub-saturating enzyme concentrations. We note that the expression for k_{cat}/K_m is the same, regardless of whether single or multiple turnover conditions are used.

To correct for the effect of enzyme depletion by vacant ribosomes (~50–100 nM) in the reactions, we calculated the concentration of ribosome-bound PDF and MAP concentrations (Table S2.1) using quadratic equations derived from the following equilibria:

$$\begin{aligned} \text{ribosome} + \text{PDF} &\overset{K_d^{PDF}}{\rightleftharpoons} \text{ribosome} \cdot \text{PDF} \\ \text{ribosome} + \text{MAP} &\overset{K_d^{MAP}}{\rightleftharpoons} \text{ribosome} \cdot \text{MAP} \end{aligned} \quad (4)$$

in which the values of K_d^{PDF} and K_d^{MAP} were 1.8 μM and 2.4 μM, respectively, as reported previously (Bingel-Erlenmeyer et al., 2008; Sandikci et al., 2013). The effective enzyme concentration was calculated by subtracting ribosome-bound enzyme from total enzyme concentration.

MAP peptidase activity assay

The peptidase activity of purified MAP on a peptide substrate, Met-Gly-Met-Met, was measured by a coupled assay as described (Frottin et al., 2006). Briefly, the N-terminal

methionine released by MAP was oxidized by *L*-amino-acid oxidase and peroxidase, resulting in changes in absorbance at 440 nm. Each reaction (100 μL) contained 50 mM Hepes-KOH (pH 7.5), 0.2 mM $CoCl_2$, 0.1 mg/mL *o*-dianisidine (Sigma), 3 units of horseradish peroxidase (Sigma), 0.5 units of *L*-amino-acid oxidase (Sigma), 0.2 μM MAP and varying concentrations of Met-Gly-Met-Met (Genscript). The substrate concentration dependence of initial velocities was fit to the Michaelis-Menten equation to obtain the k_{cat} and K_m values.

Fluorescence labeling of MAP and MAP-H79A

MAP and MAP-H79A containing a C-terminal GLPATGG tag were labeled with BODIPY-FL (Invitrogen) at the C-termini using sortase-mediating reactions (Guimaraes et al., 2013). The labeling reactions contained 50 μM MAP, 120 μM His_6-tagged sortase A and 250 μM GGGC-BODIPY peptide, and incubated at room temperature for 4 h. Sortase A was removed by incubation with Ni-NTA resin, and excess peptides were removed using Sephadex G25 (Sigma) gel filtration column. The labeling efficiency was estimated to be >90%.

Fluorescence measurement

All fluorescent measurements were carried out at room temperature in assay buffer containing 0.1 mM $CoCl_2$. Emission spectrum and equilibrium titrations were measured on

a Fluorolog-3 spectrofluorometer (HORIBA) using an excitation wavelength of 360 nm. Cm-labeled RNC (8 nM) was deformylated with 100 nM PDF for at least 15 min and incubated with indicated proteins before the measurement. For equilibrium titrations, the fluorescent signals were normalized to the signal without MAP-H79A, and fit to Eq. 5,

$$F_{obsd} = F_{max} \cdot \frac{[RNC] + [MAP] + K_d - \sqrt{([RNC] + [MAP] + K_d)^2 - 4[RNC][MAP]}}{2[RNC]} \quad (5)$$

in which [RNC] and [MAP] are input values as described, F_{obsd} is the normalized fluorescent signal, F_{max} is the signal at saturating MAP concentration, and K_d is the equilibrium dissociation constant of the RNC-MAP complex. The association rate constant (k_{on}) of the RNC-MAP complex was measured on a Kintek stopped-flow apparatus. Cm-labeled RNC (16 nM) was deformylated with 200 nM PDF for at least 15 min before the measurement, and mixed with an equal volume of various concentrations of MAP-H79A to initiate the reaction. The fluorescent signals (I) were monitored over time, and the time courses were fit to Eq. 6,

$$I(t) = I_0 + (I_{max} - I_0) \cdot \left(1 - e^{-k_{app}t}\right) \quad (6)$$

where I_0 is the signal at t = 0, I_{max} is the signal at t = ∞, and k_{app} is the observed rate constant for complex assembly. The values of k_{app} were plotted against [MAP-H79A] and fit to Eq. 7,

$$k_{app} = k_{on} \cdot [MAP] + k_{off} \quad (7)$$

where k_{on} and k_{off} are the association and dissociation rate constants for the RNC-MAP complex, respectively.

Cotranslational NME assay

PCR fragments encoding T7 promoter and FtsQ-X2-TrxA were transcribed and translated in 10 μL of mixture containing 12 mM magnesium glutamate, 10 mM ammonium glutamate, 175 mM potassium glutamate, 1.2 mM ATP, 0.86 mM each of GTP, CTP, and UTP, 34 μg/mL folinic acid, 0.17 mg/mL *E. coli* tRNA (Roche), 2 mM each of amino acids except methionine, 2% (v/v) ^{35}S-methionine, 33 mM phosphoenolpyrovate, 0.33 mM β-nicotinamide adenine dinucleotide, 0.26 mM CoA, 2.7 mM sodium oxalate, 1.5 mM spermidine, 1 mM putrescine, 4 μM anti-ssr1 oligonucleotide, 28% (v/v) S30 extract, 1 unit/μL RNase inhibitor (NEB), and 6 μM T7 RNA polymerase, pH 7.8, at 30 °C for 30 min. Where indicated, the control reactions contained 5 μM actinonin. Reactions were quenched with SDS sample loading buffer (60 mM Tris-HCl, 1.6% SDS, 30 mM EDTA, 2.6 M urea, 30 mM DTT, 15% glycerol, pH 6.8) and analyzed by SDS-PAGE and autoradiography.

Preparation of ribosome-free cell extracts

S30 extracts were supplemented with 500 mM KOAc and ultra-centrifuged in TLA120.2 (Beckman-Coulter) rotor at 100,000 rpm, 4 °C for 1 h to sediment the ribosomes. The supernatant was dialyzed against buffer containing 10 mM Tris-HCl (pH 8.2), 150 mM KOAc, and 14 mM $Mg(OAc)_2$.

Western blots for protein quantification in cell extracts

The concentrations of purified proteins were determined by the absorption at 280 nm (Strep-Sbh1) or Bradford assay (PDF and MAP-HA). Rabbit anti-PDF (MBS2547699; MyBiosource), mouse anti-HA (Genscript), and mouse anti-Strep (Genscript) are commercially available. IRDye 800CW goat anti–rabbit IgG (925-32211; LI-COR Biosciences) or IRDye 800CW goat anti–mouse IgG (925-32210; LI-COR Biosciences) were used for detection, and the signals were quantified by the Odyssey CLx imaging system (LI-COR Biosciences).

Simulation modeling for cotranslational NME

A kinetic framework was constructed to describe the cotranslational NME of an *n*-residue nascent protein under single turnover conditions (Fig. 2.4A). This describes the reactions during *in vitro* translation in S30 lysate, in which the concentration of ribosome is in excess of actively translated nascent proteins (Fig. S2.5A). The scheme in Fig. 2.4A can

be described by the following differential equations for every nascent chain length *i*, ranging from 1 to *n*:

$$\frac{d}{dt}fmRNC(i,t) = k_{trans}fmRNC(i-1,t) - k_{trans}fmRNC(i,t) - k_i^{PDF}fmRNC(i,t) \quad (8)$$

$$\frac{d}{dt}mRNC(i,t) = k_{trans}mRNC(i-1,t) - k_{trans}mRNC(i,t) + k_i^{PDF}fmRNC(i,t) - k_i^{MAP}mRNC(i,t) \quad (9)$$

$$\frac{d}{dt}RNC(i,t) = k_i^{MAP} \cdot mRNC(i,t) \quad (10)$$

where *fmRNC*, *mRNC,* and *RNC* represent the concentrations of unprocessed, deformylated, and demethionylated RNCs, respectively. Note that at the start of translation elongation (*i* =1), *fmRNC* (*i*-1, *t*) = *mRNC* (*i*-1, *t*) = 0. At translation termination (*i* = *n*), the terms k_{trans}*fmRNC* (*i*, *t*) and k_{trans}*mRNC* (*i*, *t*) were omitted.

The rate constants and other parameters used in the simulation are summarized in Table S2.1. The elongation rate constant (k_{trans}) was set to 2 residues per second, as reported previously (Underwood et al., 2005). k_i^{PDF} and k_i^{MAP} are the pseudo-first-order rate constants for the PDF and MAP reactions at chain length i, respectively, and were calculated from $(k_{cat}/K_m)^{PDF}$[PDF] and $(k_{cat}/K_m)^{MAP}$[MAP]. We assumed that NME initiated when the nascent

chain length reached 45 residues; hence $(k_{cat}/K_m)^{PDF}$ and $(k_{cat}/K_m)^{MAP}$ were set to zero for nascent chains that are 0-44 amino acids long. Values of $(k_{cat}/K_m)^{PDF}$ and $(k_{cat}/K_m)^{MAP}$ at nascent chain lengths 45, 49, 67, 82, and 127 were experimentally measured, those at in-between nascent chain lengths were linearly interpolated from experimental data, and those for nascent chains longer than 127 residues were set to be the same as for $RNC_{FtsQ127}$. The total concentrations of PDF and MAP were determined to be ~300 nM by quantitative western blot in S30 extract (Fig. S2.5B, C). We found that the activity of endogenous MAP in the cell extract was ~2 fold lower than that of the recombinant enzyme (Figs. S2.5E–F); hence, a two-fold correction was made to the absolute MAP concentration to obtain an effective MAP concentration. Depletion of enzyme due to interaction with non-translating ribosome (2.6 μM in S30 extract) was corrected by the same method as in measurements of reactions using purified RNCs (see Eq 4 under "*Kinetic analysis*").

A Matlab script was used to simulate the time-dependent concentration of each species using the numerical integration method. The initial concentrations at t = 0 were set to 1 for *fmRNC* (1,0) and 0 for all other species. A step size of 0.05 s was used to simulate the cotranslational NME of a 300-residue nascent protein (n = 300) over the time-course of 150 s. The time-course was extended to 600 s for the simulations with k_{trans} = 0.5 and 1 s^{-1} in Figs. 2.4B–E and Figs. S2.7A–D. To estimate the contribution of experimental errors to the simulation result, the enzyme concentrations, dissociation constants, and the values of k_{cat}/K_m

were randomly selected from normal distributions described by the mean value and relative S.D., and the simulation was repeated 100 times.

2.5. Supplementary Figures and Tables

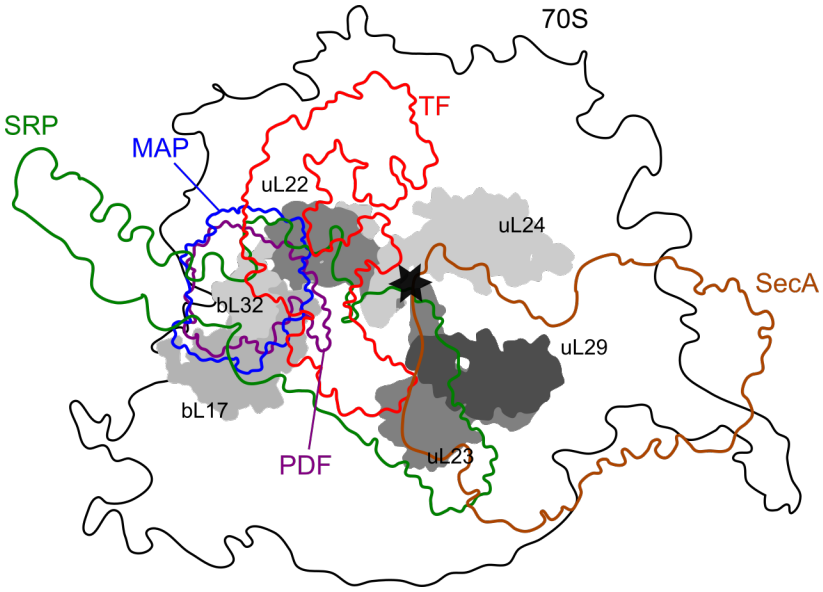

Figure S2.1. Structure projections of various RPBs on the ribosome.

PDF (purple), MAP (blue), TF (red), SRP (green) and SecA (brown) were shown as outlines of the projections on 70S ribosome from the view of the large subunit, based on reported structures and models (PDB-4V4Q, EMD-9750, EMD-9751, EMD-1499, EMD-1250, and EMD-2564) (Schuwirth et al., 2005; Bhakta et al., 2019; Merz et al., 2008; Schaffitzel et al., 2006). Projections of ribosomal proteins near the exit site (star) were indicated.

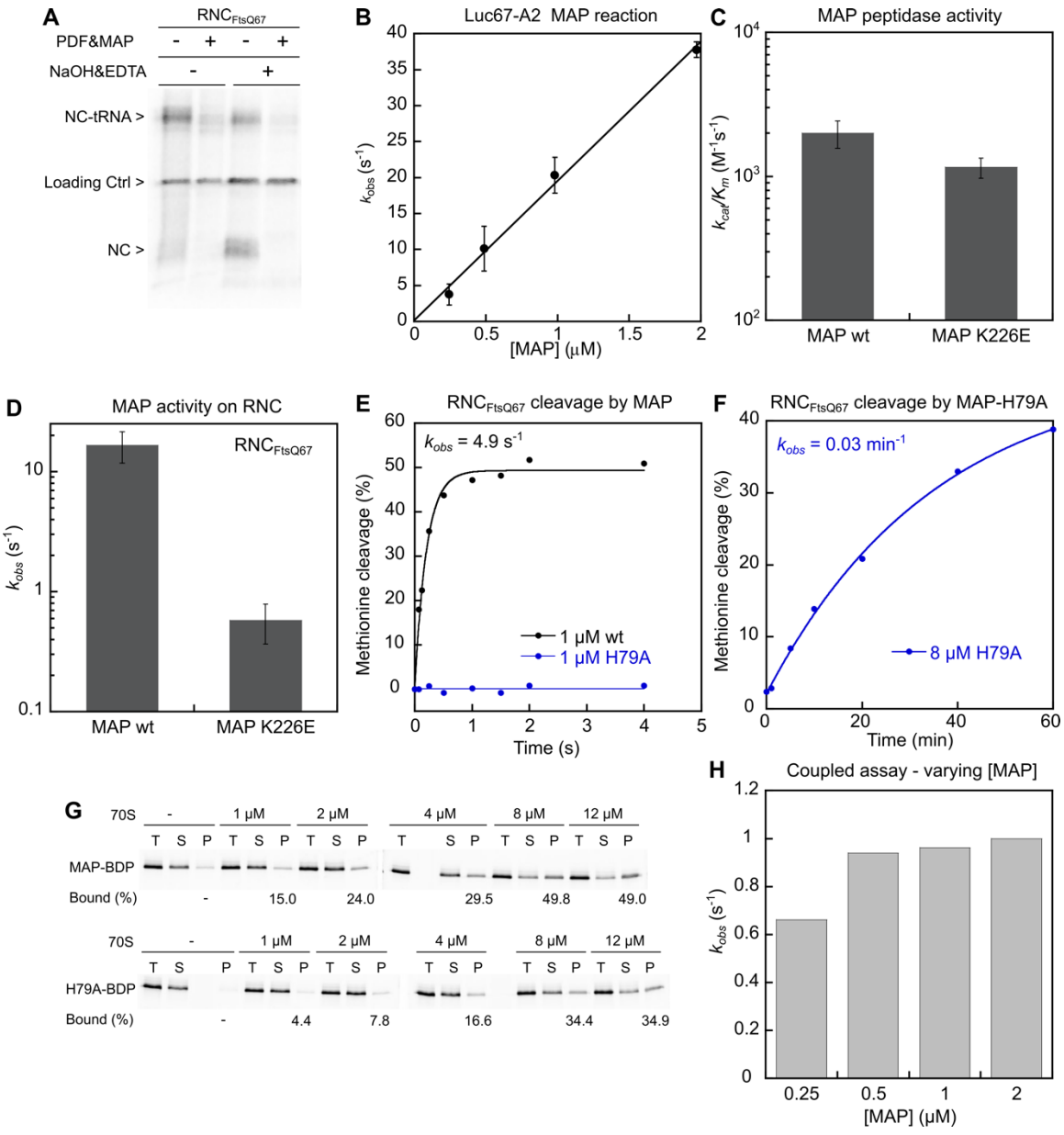

Figure S2.2. Validations of the assays for MAP and PDF reactions.

(A) Autoradiograph of purified RNC$_{FtsQ67}$. The N-terminal methionine on the nascent chain (NC) was ^{35}S-labeled and was cleaved by incubation with 3 μM PDF and MAP ('+' lanes). The NC-tRNA conjugate was verified by hydrolysis with 100 mM NaOH and 25 mM

EDTA (42 °C, 30 min) after the reaction (lanes 3 and 4). **(B)** The MAP concentration dependence of observed rate constants for methionine cleavage of RNC bearing the N-terminal 67 residues of luciferase (Luc). The second residue (Asn) of luciferase is mutated to alanine such that the N-terminal sequence (MADAK) allows cleavage by PDF and MAP. Linear fit of the data gave a k_{cat}/K_m value of (1.9± 0.06) × 10^7 $M^{-1}s^{-1}$. Data are shown as mean ± S.D., with n = 2. **(C)** Comparison of the peptidase activities between wildtype MAP and MAP-K226E, using a tetra-peptide (MGMM) as substrate. Data are shown as mean ± S.D., with n = 2. **(D)** Observed rate constants of wildtype MAP and MAP-K226E for methionine excision on RNC_{FtsQ67}. The reactions were measured as in Fig. 2.1B with 10 nM RNC_{FtsQ67}, 50 nM PDF, and 1 μM wildtype MAP or MAP-K226E. Data are shown as mean ± S.D., with n = 3. **(E)** Representative time traces for the cleavage of 10 nM $RNC_{Met\text{-}FtsQ67}$ by 1 μM wildtype MAP (black) or mutant MAP-H79A (blue). **(F)** The cleavage of $RNC_{Met\text{-}FtsQ67}$ by MAP-H79A (8 μM) was carried out over a longer time course to measure the observed reaction rate constant for this mutant. **(G)** Representative image for the binding of wildtype MAP and MAP-H79A to 70S ribosome, measured by the co-sedimentation assay. 1 μM BODIPY-labeled MAP or MAP-H79A was incubated with indicated concentrations of 70S ribosomes at room temperature for 20 min in binding buffer (50 mM Hepes-KOH, 50 mM KOAc, 10 mM $Mg(OAc)_2$, 0.1 mM $CoCl_2$, pH 7.5). 40 μL of the reaction was loaded onto 80 μL of 20% sucrose in binding buffer, and centrifuged in TLA100 rotor (Beckman Coulter) at 80,000 rpm, 4 °C for 75 min. The ribosome pellet was resuspended with 40 μL of SDS sample loading dye (50 mM Tris-HCl, 1% SDS, 10% glycerol, 100 mM DTT, pH 6.8). Total reaction (T), supernatant (S) and pellet (P) were analyzed by SDS-PAGE and quantified with Typhoon FLA7000 fluorescence imager. The values underneath are the amount of ribosome-bound MAP, determined by the fluorescence intensities in the pellet lane to the corresponding total lane. **(H)** The observed rate constant for deformylation of $RNC_{fMet\text{-}FtsQ67}$, measured using the coupled assay in Figure 2.2B, was determined with 1 μM PDF and indicated concentrations of MAP. The observed rate constant did not change significantly at MAP concentrations above 0.5 μM, indicating that the MAP reaction is not rate-limiting under these conditions.

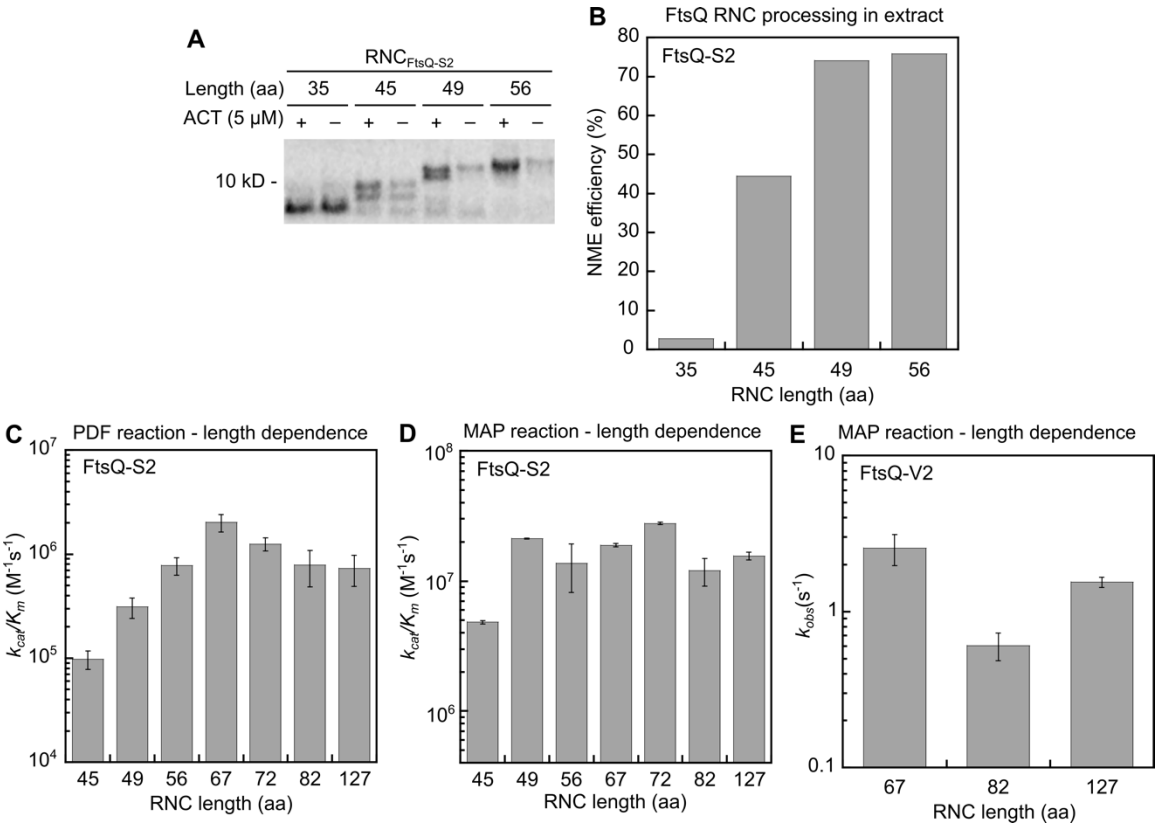

Figure S2.3. Length dependence of NME reactions.

(A) NME of RNC_{FtsQ} with different nascent chain lengths in cell extract. RNCs bearing FtsQ nascent chains containing a single N-terminal ^{35}S-Methionine were generated by *in vitro* translation in the S30 extract and allowed to be processed by endogenous PDF and MAP during a 1-h translation ('– actinonin' lanes). The '+ actinonin' lanes provide controls for the amount of RNC without NME. The extent of NME was analyzed by SDS-PAGE and autoradiography. **(B)** Quantification of the data in (A) by normalizing the nascent peptide signals in the '– actinonin' lanes relative to parallel translations in the '+ actinonin' lanes. **(C)**, **(D)** Summary of the k_{cat}/K_m values of the PDF (C) and MAP (D) reactions for RNCs bearing FtsQ-S2 nascent chains of the indicated lengths. The PDF reaction rate constants were measured using the coupled deformylation assay (Fig. 2.2B). **(E)** Observed rate constants of MAP reactions on $RNC_{FtsQ-V2}$ at the indicated nascent chain lengths. Reactions were measured with 10 nM $RNC_{FtsQ-V2}$ and 1 μM MAP. Values in (C)–(E) are shown as mean ± S.D., with n = 2–3.

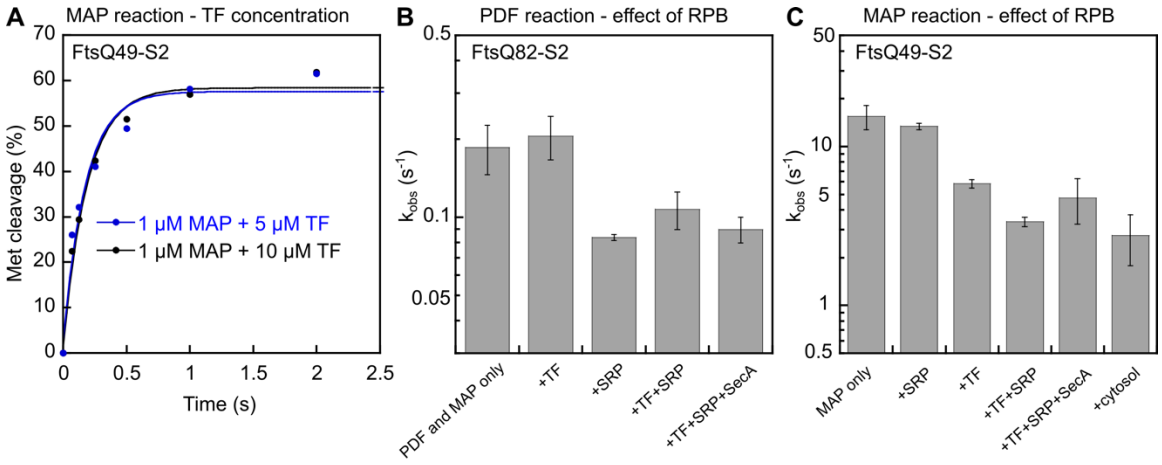

Figure S2.4. RPB effects on NME reactions.

(A) Time traces for cleavage of 10 nM $RNC_{FtsQ49\text{-}S2}$ by 1 μM MAP in the presence of 5 μM (blue) or 10 μM (black) TF. The data were fit to Eq. 1 and gave k_{obs} values of 5.6 and 5.3 s^{-1}, respectively, indicating the saturation of TF effect on the MAP reaction. **(B)** Effects of TF, SRP and SecA on the deformylation of $RNC_{FtsQ49\text{-}S2}$. Observed rate constants were measured with 10 nM $RNC_{FtsQ82\text{-}S2}$, 0.5 μM PDF and 1 μM MAP using the coupled assay. Where indicated, the reactions also contained 5 μM TF, 400 nM SRP, and 1 μM SecA. **(C)** Effects of TF, SRP, SecA, or ribosome-free cytosol on methionine cleavage of $RNC_{FtsQ49\text{-}S2}$ by MAP. Observed rate constants were measured with 10 nM $RNC_{FtsQ49\text{-}S2}$ and 1 μM MAP. The '+cytosol' reaction contained 28% (v/v) of ribosome-free S30 extract with ~110 nM endogenous MAP (see Materials and Methods and Fig. S2.7D). The data in (B) and (C) are shown as mean ± S.D., with n = 2.

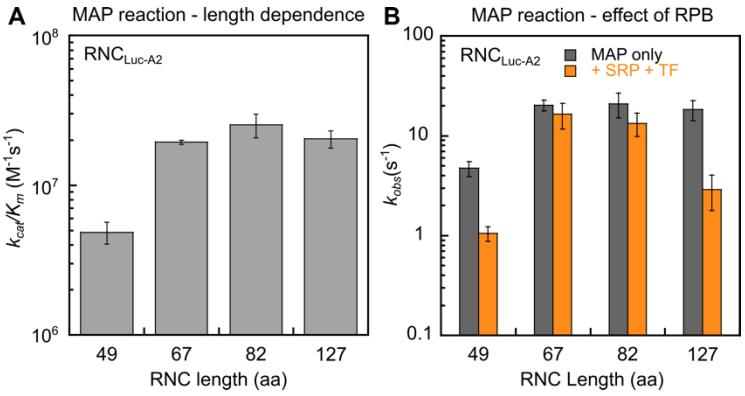

Figure S2.5. Length dependence and RPB effect on MAP reactions of RNC$_{Luc}$.

(A) Summary of the k_{cat}/K_m values of the MAP reaction for RNCs bearing the luciferase nascent chain of indicated lengths. **(B)** Effects of TF and SRP on methionine cleavage of RNCs bearing the luciferase nascent chains of indicated lengths. Observed rate constants were measured with 10 nM RNCs and 1 μM MAP. All data are shown as mean ± S.D., with n = 2.

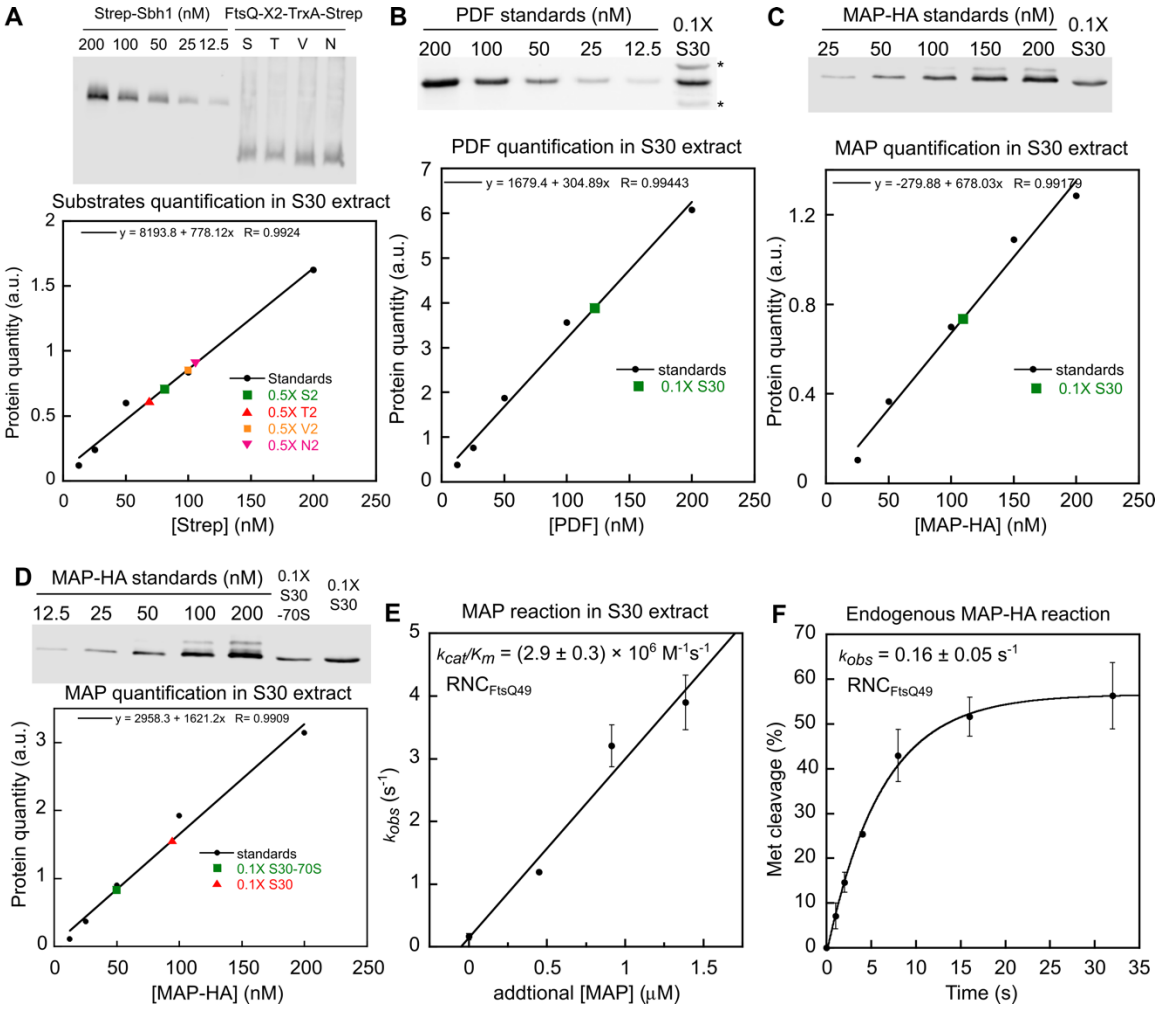

Figure S2.6. Characterization of endogenous PDF and MAP-HA in cell extracts.

(A) Anti-Strep immunoblot (upper panel) to measure the concentrations of the substrates for the cotranslational NME assay, FtsQ-X2-TrxA-Strep, translated for 30 min at 30 °C in S30 extract. Known concentrations of a purified Strep-tagged protein, Sbh1, were used to construct a standard curve for the quantification (lower panel, black line). The substrate concentrations were determined to be 150–200 nM; as ribosomes were being turned over during translation, these values are upper limits of the substrate concentration during cotranslational NME. (B) A representative anti-PDF immunoblot (upper panel) to measure the endogenous level of PDF in S30 extract. Known concentrations of purified PDF were used to construct a standard curve for quantification (lower panel). The PDF concentration

was determined to be 320 ± 20 nM (S.D., n = 3) in the *in vitro* translation (IVT) reactions, which contained 28% (v/v) of S30 extract. The asterisks denoted non-specific bands. (C) Representative western blot (upper panel) to determine the endogenous level of MAP in S30 extract. To facilitate quantification, an HA tag was engineered C-terminal to the genomic MAP. The activity of MAP-HA in the cell extract was comparable to that of wild-type MAP (Fig. S2.9). Known concentrations of purified MAP-HA were used to construct a standard curve for the quantification (lower panel). The concentration of MAP-HA was determined to be 250 ± 50 nM (S.D., n = 4) under IVT conditions. (D) A representative anti-HA immunoblot to measure the endogenous level of MAP-HA in S30 extract and in ribosome-free cytosol (S30–70S) used in the reactions shown in Figures S2.7E, S2.7F, and S2.3C. The concentration of MAP-HA in the ribosome-free extract was determined to be 110 ± 40 nM (S.D., n = 2) under IVT conditions. (E) Observed rate constants for methionine cleavage of $RNC_{FtsQ67\text{-}S2}$ in the presence of ribosome-free cytosol were plotted as a function of MAP concentration. The reactions contained 10 nM RNC, 28% (v/v) ribosome-free S30 extract with ~110 nM endogenous MAP (measured in (D)), and indicated concentrations of purified MAP. The line is a linear fit of the data, and the obtained k_{cat}/K_m value is indicated. (F) Time course for methionine cleavage of $RNC_{FtsQ67\text{-}S2}$ by endogenous MAP-HA in the S30 extract. The reaction contained 10 nM RNC and 28% (v/v) ribosome-free S30 extract containing ~110 nM endogenous MAP. The data were fit to single exponential function and gave a k_{obs} value of 0.16 ± 0.05 s^{-1}, ~2-fold slower than that expected based on the k_{cat}/K_m value measured in Fig. S2.7E, suggesting that endogenous MAP has 2-fold lower activity than purified MAP. Values in (E) and (F) are shown as mean ± S.D., with n = 2.

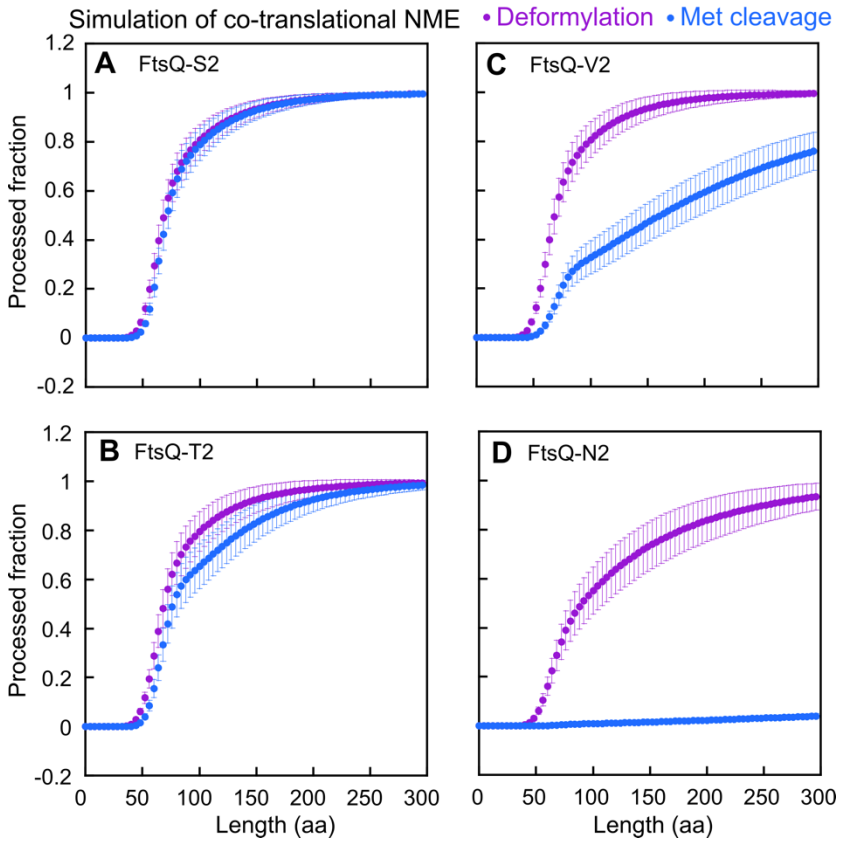

Figure S2.7. Comparison of the simulated reaction profiles for cotranslational deformylation (magenta) and methionine cleavage (blue) of FtsQ-X2 in the presence of RPBs.

The profiles were plotted as the cumulative fraction of processed RNCs over time, which was converted to the nascent chain length being synthesized. For each independent run, the enzyme concentrations and the processing rates were randomly selected from normal distributions with a relative S.D. of 20%. Results from 100 runs were shown as mean ± S.D.

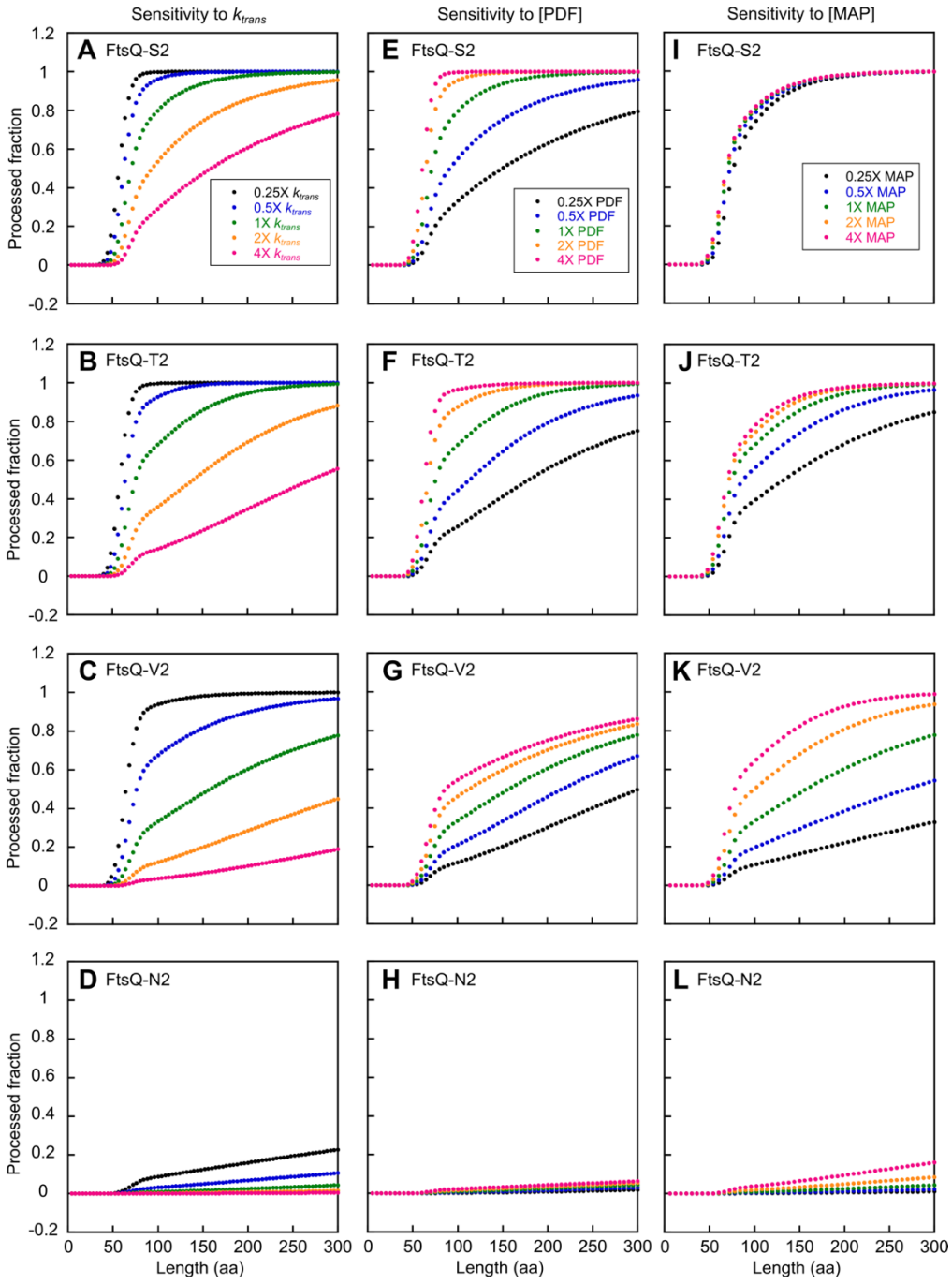

Figure S2.8. The individual NME reaction profiles generated during the sensitivity test shown in Figs. 2.4B–E.

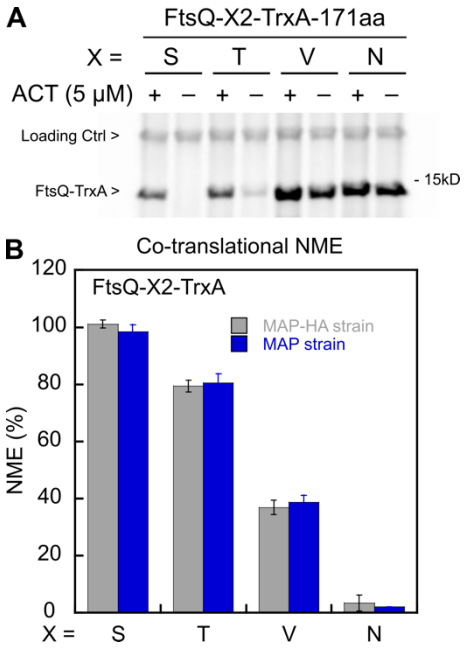

Figure S2.9. The C-terminal HA tag did not affect MAP function.

(A) Representative SDS-PAGE and autoradiography analysis of cotranslational processing of FtsQ-X2-TrxA in the S30 extract prepared from *E. coli* strain harboring MAP-HA. (B) Quantification of the cotranslational NME efficiency from the data in (A) and replicates, and comparison with the NME efficiency from the S30 extract from the wild-type strain (Fig. 2.5D).

Table S2.1. Parameters used in the kinetic simulation model.

All values are represented as mean ± S.D., and the relative S.D. are indicated in parentheses. The RPB effect is represented as folds decrease relative to the condition without RPBs. The effects of second residues and nascent chain length for T2, V2, N2 are represented as folds reduction relative to S2.

ribosome	2.6 ± 0.3 μM (10%)	Free [PDF] = 130 ± 25 nM (20%) Free [MAP] = 63 ± 15 nM (20%)
[PDF]	320 ± 20 nM (10%)	
[MAP]	130 ± 25 nM (20%)	
K_d^{PDF}	1.8 ± 0.5 μM (30%)	
K_d^{MAP}	2.4 ± 0.4 μM (20%)	
k_{trans}	2 aa/s	

k_{PDF} (20%)	Length	45	49	56	67	72	82	127
	k_{cat}/K_m (10^6 $M^{-1}s^{-1}$)	0.098	0.31	0.76	2.0	1.3	0.78	0.73
	RPB effect	2						
	Second residue effect	S2: 1 T2: 1 V2: 1 N2: 2						

k_{MAP} (20%)	Length	45	49	56	67	72	82	127
	k_{cat}/K_m (10^7 $M^{-1}s^{-1}$)	0.14	2.1	1.4	1.9	2.8	1.2	1.6
	RPB effect for S2	4.6	4.6	3.2	1.1	1.1	1.3	1.7
	RPB effects for T2, V2, N2	2.4	2.4	2	1.6	2	3	8
	Length effects for T2, V2, N2	3.6	3.6	1	1	1	2	1
	Second residue effect	S2: 1 T2: 2 V2: 10.3 N2: 294						

C h a p t e r 3

RIBOSOME-NASCENT CHAIN INTERACTION REGULATES N-TERMINAL PROTEIN MODIFICATION

A version of this chapter was first published as: Yang, C.-I., Kim, J., Shan, S.-o. (2022). "Ribosome-nascent Chain Interaction Regulates N-terminal Protein Modification." In: *Journal of Molecular Biology* 434, pp. 167535. doi: 10.1016/j.jmb.2022.167535.

Numerous proteins initiate their folding, localization, and modifications early during translation, and emerging data show that the ribosome actively participates in diverse protein biogenesis pathways. Here we show that the ribosome imposes an additional layer of substrate selection during N-terminal methionine excision (NME), an essential protein modification in bacteria. Biochemical analyses show that cotranslational NME is exquisitely sensitive to a hydrophobic signal sequence or transmembrane domain near the N-terminus of the nascent polypeptide. The ability of the nascent chain to access the active site of NME enzymes dictates NME efficiency, which is inhibited by confinement of the nascent chain on the ribosome surface and exacerbated by signal recognition particle. *In vivo* measurements corroborate the inhibition of NME by an N-terminal hydrophobic sequence, suggesting the retention of formylmethionine on a substantial fraction of the secretory and membrane proteome. Our work demonstrates how molecular features of a protein regulate its

cotranslational modification and highlights the active participation of the ribosome in protein biogenesis pathways via interactions of the ribosome surface with the nascent protein.

3.1. Introduction

Proteins carry out the majority of biological functions in the cell. To acquire their functionality, newly synthesized proteins need to undergo adequate modifications, fold into the correct structures, and reach their proper cellular destinations. These processes, collectively termed protein biogenesis, often occur when the nascent polypeptide is being synthesized on the ribosome. The surface of the ribosome surrounding the nascent polypeptide tunnel exit serves as a hub to recruit various ribosome-associated protein biogenesis factors (RPBs) (Koubek et al., 2021; Kramer et al., 2009, 2019). In bacteria, these include targeting factors such as Signal Recognition Particle (SRP) and SecA, cotranslational chaperones such as Trigger Factor (TF), and protein modification enzymes. The nascent protein encodes molecular signals to initiate dedicated protein biogenesis pathways. For instance, SRP recognizes a transmembrane domain (TMD) on membrane proteins, or a strong signal sequence containing a continuous stretch of hydrophobic amino acids (Akopian et al., 2013) on a subset of secretory proteins. TF broadly engages hydrophobic sequences on cytosolic proteins as well as a subset of secretory proteins (De Geyter et al., 2020; Oh et al., 2011; Patzelt et al., 2001; Valent et al., 1995). During translation elongation, emergence of new molecular signals on the nascent protein could allow distinct RPBs to be recruited or

repositioned on the ribosome and potentially guide the sequence of cotranslational biogenesis events (Koubek et al., 2021; Kramer et al., 2019).

In addition to the recruitment of RPBs, the ribosomal surface also directly interacts with diverse nascent polypeptides. The surface of the 50S ribosome subunit is highly acidic due to the ribosomal RNA (Fedyukina et al., 2014) and able to constrain nascent chains via electrostatic interactions (Cassaignau et al., 2021; Kaiser et al., 2011). In addition, multiple nonpolar regions are decorated on the ribosome surface at uL23/uL29, uL24, and bL17/bL32 (Fedyukina et al., 2014; Guzman-Luna et al., 2021). Several nascent chains bearing hydrophobic signal sequences were reported to interact with uL23/uL29 adjacent to the tunnel exit (Eisner et al., 2006; Peterson et al., 2010; Ullers et al., 2003; Wang et al., 2019). Recently, it was reported that even an intrinsically disordered nascent protein crosslinks strongly to uL23 and the neighboring uL29 in a Mg^{2+}-dependent manner (Guzman-Luna et al., 2021). These ribosome-nascent chain interactions have been shown to stabilize the nascent protein in an unfolded state until downstream sequences emerge to recruit cotranslational chaperones or binding partners(Cabrita et al., 2016; Cassaignau et al., 2021; Kaiser et al., 2011; Waudby et al., 2019). This ‘holdase’ activity of the ribosome allows nascent proteins to avoid local kinetic traps and thus fold productively (Waudby et al., 2019). While the contribution of the ribosome in cotranslational protein folding has been actively studied, whether ribosome-nascent interactions participate in other biogenesis pathways remains unclear.

The covalent modification of nascent proteins constitutes an essential branch of cotranslational protein biogenesis. In bacteria, translation is initiated with formylmethionine (fMet), which is sequentially removed via the N-terminal methionine excision (NME) process catalyzed by two enzymes: peptide deformylase (PDF) and methionine aminopeptidase (MAP) (Giglione et al., 2004, 2015). Both enzymes are essential in bacteria and important targets for developing antibiotic drugs (Giglione et al., 2004). While PDF is promiscuous, MAP preferentially cleaves nascent polypeptides with small amino acids at the second residue after initiator methionine (iMet) (Frottin et al., 2006; Hu et al., 1999). Under physiological conditions, the NME reactions are further reshaped by the ribosome and other RPBs (Oh et al., 2011; Ranjan et al., 2017; Sandikci et al., 2013; Yang et al., 2019). Using substrates bearing structureless N-terminal sequences from a membrane protein FtsQ and a cytosolic protein luciferase, our previous work demonstrated that the association of MAP with the ribosome leads to rate enhancements of 10^2-10^4 fold compared to reactions on peptide substrates, allowing diffusion-limited nascent chain processing by MAP. On the other hand, SRP and TF selectively restrict the time window for the reaction of suboptimal substrates with large side chains at the second residue, and thus ensure the local sequence specificity of cotranslational NME (Yang et al., 2019). These observations underscore multiple mechanisms that can influence NME.

These previous studies were carried out on nascent polypeptides largely devoid of structural features near the N-termini, raising questions as to whether and how molecular

features on the nascent chain in addition to the size of the second residue following iMet contribute to NME. Indeed, SRP was found to inhibit the deformylation of ribosome-nascent chain complexes (RNCs) bearing TMD or signal sequences on the nascent chain (Ranjan et al., 2017). However, ~50% of the SRP-engaging proteins identified by selective ribosome profiling experiments underwent NME *in vivo* (Bienvenut et al., 2015; Schibich et al., 2016). Moreover, FtsQ, a *bona-fide* SRP substrate, was efficiently processed by both PDF and MAP on the ribosome, suggesting that the SRP-induced inhibition of deformylation is conditional on other molecular determinants (Yang et al., 2019). Whether and how molecular features on the nascent protein are sensed by the ribosome and other RPBs to determine the N-termini status of nascent proteins remain to be understood.

In this work, a combination of enzymatic kinetics, fluorescence measurements, and crosslinking analyses show that a contiguous stretch of hydrophobic residues, from either a TMD or a strong signal sequence, located near the N-terminus of the nascent chain inhibits both PDF and MAP reactions. This inhibition is due to confinement of the nascent chain on the ribosomal surface and is further exacerbated by SRP. Consistent with the biochemical measurements, this inhibitory effect remains dominant over the intrinsic sequence preference of the enzymes *in vivo*, leading to the retention of fMet on ~10% of the bacterial proteome. Our work reveals a previously unrecognized mechanism by which NME is regulated under physiological conditions, and provides a novel example of the active participation of the ribosome in protein biogenesis via its interaction with the nascent protein.

3.2. Results

An early TMD or signal sequence inhibits cotranslational NME.

Previous work based on peptide substrates showed that MAP strongly prefers substrates with a small residue following iMet (Frottin et al., 2006). To uncover additional features on the nascent protein that regulate NME efficiency and to test whether NME differs for proteins destined for different biogenesis pathways, we *in vitro* translated a series of model substrates in the *E. coli* S30 extract in the presence of ^{35}S-methionine (Yang et al., 2019)(Fig. 3.1A). The model substrates consist of N-terminal sequences derived from proteins of interest fused to a cytosolic protein, thioredoxin (TrxA), and are free of methionine residues other than the iMet. To control for the specificity of MAP for small second-site residues, we replaced the second residue of all substrates with alanine (Figs. 3.1B and S3.1A). These substrates are subject to NME by endogenous PDF and MAP and to regulation by additional factors in the lysate during translation, and their NME efficiency is determined by the reduction of the iMet signal (Fig. 3.1A).

Despite bearing the same second site residue, different NME levels were observed for the model substrates tested (Figs. S3.1B, C). Substrates bearing the N-terminus of cytosolic proteins, luciferase (Luc) and chloramphenicol acetyltransferase (CAT), were completely processed by PDF and MAP. Complete NME was also observed for integral membrane proteins FtsQ and RodZ, which can cotranslationally engage SRP and SecA

(Valent et al., 1995; Rawat et al., 2015; Wang et al., 2017; Schibich et al., 2016). NME was modestly inhibited on the secretory proteins OmpA and PhoA, which harbor weakly hydrophobic signal sequences (Hartl et al., 1990; Oh et al., 2011; Valent et al., 1995), and strongly inhibited on DsbA, a secretory protein with a more hydrophobic signal sequence. EspP, an autotransporter bearing a 38-residue N-terminal element (NTE) preceding a hydrophobic signal sequence (Peterson et al., 2006), was efficiently processed, whereas removal of its NTE (EspP dNTE) abolished NME. These results demonstrate additional layers of regulation of NME efficiency contributed by the N-terminal signals beyond the size of the second residue.

A common feature of the strongly inhibited substrates, DsbA and EspP dNTE, is a hydrophobic signal sequence that closely follows iMet. To test the effect of signal sequence hydrophobicity on NME, we replaced the hydrophobic core of the PhoA signal sequence with leucine and alanine and systematically varied the Leu/Ala ratio (Doud et al., 1993) (Fig. 3.1C). NME was strongly inhibited on the more hydrophobic variants, 3A7L and 2A8L (Figs. 3.1D and E). Despite having a hydrophobic TMD, FtsQ and RodZ underwent complete NME (Figs. S3.1B and C). We reasoned that the long NTE preceding their TMD might allow efficient processing by PDF and MAP before the TMD emerges from the ribosome tunnel exit. To test how the position of the TMD affects NME, we systematically truncated the NTE of FtsQ (Fig. 3.1F). Substrates with NTE longer than 12 residues were efficiently processed, but NME efficiency decreased drastically upon further truncation, indicating that a threshold

distance of the hydrophobic signal sequence or TMD to the N-terminus is required for efficient NME (Figs. 3.1G and H).

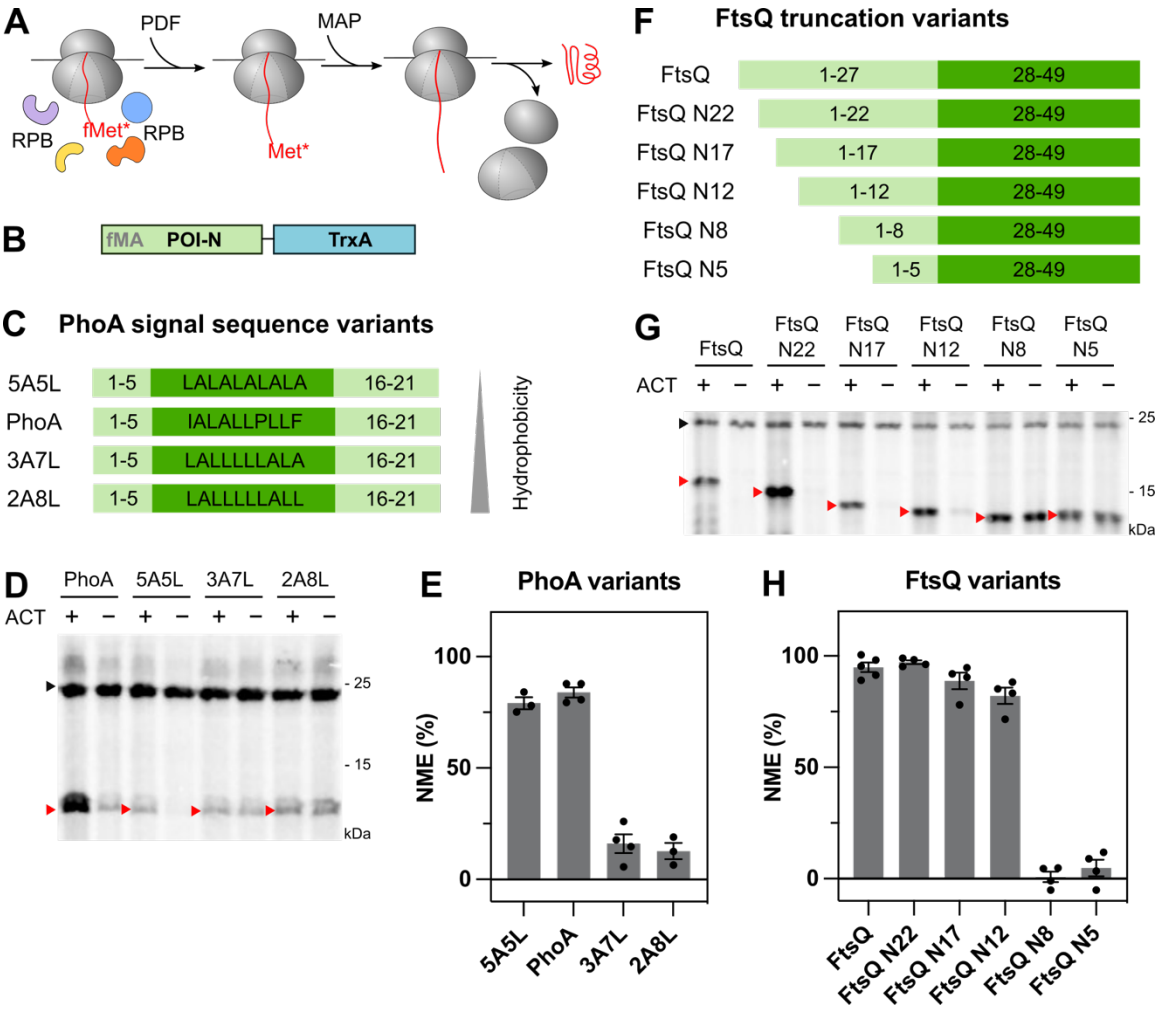

Figure 3.1. An early TMD or hydrophobic signal sequence inhibits cotranslational NME of nascent proteins.

(A, B) Scheme of the cotranslational NME assay. Model substrates (depicted in (B)) were translated in *E. coli* cell extracts containing ^{35}S-Met and processed by endogenous PDF and MAP. POI-N: N-terminal sequence of protein of interest. **(C)** Scheme of the PhoA

variants. The hydrophobic core of the signal sequence was replaced with the indicated sequences and colored in dark green. The number of the residues N- and C-terminal to the signal sequence in POI-N are indicated. **(D)** Representative SDS-PAGE autoradiography of the cotranslational NME of the PhoA variants. Red arrows indicate the substrates translated in the extracts. Black arrows indicate the loading control. Reactions in the presence of actinonin (ACT, 5 μM) provided controls for the iMet signal on substrates without NME. **(E)** Efficiency of cotranslational NME of the PhoA variants, determined from the data in (D) and their replicates by the reduction of the iMet signal in the reactions without ACT relative to that in the presence of ACT. **(F)** Scheme of the FtsQ variants. The NTE of FtsQ (first 27 residues) preceding the TMD (residues 28-49) was systematically truncated from the C-terminus, as indicated. **(G)** Representative SDS-PAGE autoradiography for cotranslational NME of the FtsQ variants. **(H)** Efficiency of cotranslational NME of the FtsQ variants, determined from the data in (G) and their replicates. All values are reported as mean ± SEM, with $n \geq 3$.

To decipher whether the inhibition is exerted on the PDF or MAP reaction, we analyzed the N-terminus of the NME-inhibited substrates after their coupled translation and processing in the S30 extract (Figs. S3.1D–F) using thin layer chromatography (TLC). Substantial remaining fMet was detected, indicating partial inhibition of the deformylation reaction (Figs. S3.1E and F). However, deformylation was reduced by only 50% on 2A8L, EspP dNTE, and DsbA and cannot fully account for the inhibition of NME, suggesting that both the PDF and MAP reactions were compromised on these substrates (Fig. S3.1F).

The results above show that a hydrophobic signal sequence or TMD near the N-terminus of a nascent protein prevents its processing by PDF and MAP. This inhibition could arise from the intrinsic properties of these sequences, or from the action of additional RPBs in the cell lysate such as SRP. To distinguish between these possibilities, we prepared ribosome-nascent chain complexes (RNCs) with a defined nascent chain sequence and a

chain length previously determined to be optimal for processing by PDF and MAP (Yang et al., 2019). The RNCs were generated via *in vitro* translation in S30 extract, and purified via a stringent sucrose-gradient centrifugation to remove ribosome-associated factors (Yang et al., 2019). We carried out pre-steady-state kinetic measurements of the PDF and MAP reactions on the purified RNCs under single-turnover conditions at sub-saturating enzyme concentrations (Fig. 3.2A) (Yang et al., 2019).

Both the PDF and MAP reactions are sensitive to the location and hydrophobicity of the membrane targeting signals. For FtsQ variants in which the NTE preceding the TMD is systematically truncated (Fig. 3.2B), the PDF and MAP reactions were inhibited by 30- and 10-fold, respectively, when the NTE was shortened to 8 residues, indicating that a flexible NTE of at least 9-12 residues is required for efficient NME (Figs. 3.2D and E). For PhoA variants in which the hydrophobicity of the N-terminal signal sequence was varied (Fig. 3.2C), the PDF reaction was slowed ~10 fold by a signal sequence with moderate hydrophobicity (5A5L vs. Luc, Fig. 3.2F) and 100-200 fold by more hydrophobic signal sequences (3A7L and 2A8L, Fig. 3.2F). The MAP reaction was also susceptible to this inhibition, with 4 fold and 40-80 fold slower rates on substrates with moderate and high hydrophobicity, respectively (Fig. 3.2G).

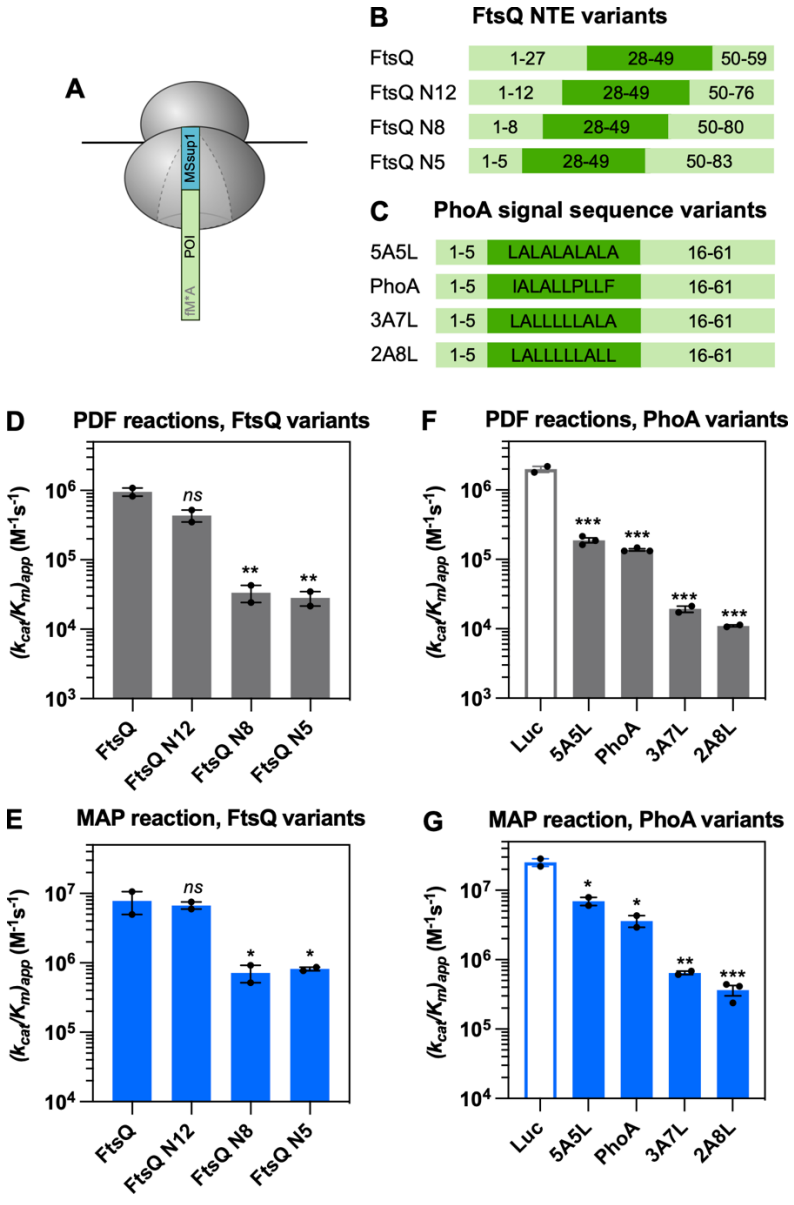

Figure 3.2. NME reactions are directly inhibited by sequence features on the nascent chain.

(A–C) Scheme of the RNC substrates used in the NME reaction measurements. An 8 amino acid stall sequence at the C-terminus, derived from Ms-sup1, allows the generation of translationally stalled nascent chains with defined lengths. The total length of the nascent

chains is 67 residues for FtsQ variants (B) and 69 residues for PhoA variants (C). The release of ^{35}S-labeled (asterisk) iMet provides readout for the extent of the reactions. **(D) and (E)** Summary of the observed rate constants of the PDF (D) and MAP (E) reactions on purified RNCs with the FtsQ variants. The PDF reactions (D) were measured with 10 nM RNC and 100 nM PDF for RNC_{FtsQ} and $RNC_{FtsQ\ N12}$ or 500 nM PDF for $RNC_{FtsQ\ N8}$ and $RNC_{FtsQ\ N5}$. The MAP reactions (E) contained 10 nM RNC and 100 nM MAP. Apparent k_{cat}/K_m is the observed pseudo-first-order rate constant divided by enzyme concentration**. (F) and (G)** Summary of the observed rate constants of the PDF (F) and MAP (G) reactions on purified RNCs with the PhoA variants. The reaction rates of RNC_{Luc} (open bars) were included for comparison with a substrate without a signal sequence. The PDF reactions (F) were measured with 10 nM RNC and 100 nM PDF for RNC_{Luc}, RNC_{PhoA} and RNC_{5A5L} or 500 nM PDF for RNC_{3A7L} and RNC_{2A8L}. The MAP reactions (G) contained 10 nM RNC and 100 nM MAP. All values are reported as mean ± SEM, with $n \geq 2$. '*', '**' and '***' represent $p \leq 0.05$, 0.01, and 0.001, respectively, based on unpaired t-tests. '*ns'*, $p > 0.05$.

In addition to hydrophobicity, a signal sequence or TMD could adopt helical structures that prevent the N-terminus from entering the enzyme active site. However, helical contents of the signal sequences, calculated from the prediction algorithm AGADIR, did not correlate with the observed NME reaction rates (Muñoz and Serrano, 1995) (Figs. S3.2). For instance, the 5A5L signal sequence has a significantly higher helical propensity than PhoA, but the reaction rate of 5A5L is comparable to or even slightly faster than that of PhoA (Figs. 3.2F and G). Therefore, secondary structure propensity is not sufficient to explain the inhibitory effect of an N-terminal signal sequence or TMD.

Collectively, the results in this section show that a hydrophobic signal sequence or TMD that emerges within 12 amino acids of the N-terminus inhibits the cotranslational modification of nascent proteins by both PDF and MAP. The observation of enzymatic

inhibition in the purified system further indicates that the molecular properties of the nascent chain are sufficient to regulate the PDF and MAP reactions.

Nascent chain-ribosome interactions regulate NME.

To understand the mechanisms by which the nascent chain sequence regulates its cotranslational NME, we considered a model in which binding of the enzymes to the RNC is followed by docking of the nascent chain N-termini at the enzyme active site, which mediates hydrolysis of the peptide bond (Fig. 3.3A). Any effect of the N-termini at the hydrolysis step can be excluded, as residues 2-4 following iMet that directly interact with the enzyme active site are identical within each set of the variants tested (Fig. 3.3A, Step 3; Figs. 3.2B and C) (Frottin et al., 2006; Hu et al., 1999). We therefore examined whether the N-terminal hydrophobic signal sequence exerts regulation by altering the ability of NME enzymes to bind the RNC (Fig. 3.3A, Step 1) or the access of the nascent chain N-termini to the enzyme active site (Step 2).

To test the first model, we established a fluorescence-based assay to measure the binding of the ribosome with PDF and MAP (Fig. 3.3B and Fig. S3.3). We incorporated a ybbR tag at the C-terminus of ribosomal protein bL17, which allows labeling of a donor dye (BODIPY-FL) via Sfp-mediated reactions (Yin et al., 2005). An acceptor dye (tetramethylrhodamine, TMR) was labeled at the N-terminus of PDF or the C-terminus of MAP. Based on structural information, the dye pairs are ~40 Å apart in the ribosome•PDF

or ribosome•MAP complex (Bhakta et al., 2019). An affinity tag (3X Strep) followed by ubiquitin (Ub) was fused N-terminally to the nascent peptide of interest, allowing affinity purification of the RNCs followed by Usp2-catalyzed removal of the N-terminal Ub fusion to generate nascent chains with the native iMet (Catanzariti et al., 2004). To bypass potential complications from enzymatic processing of the nascent chain, we used catalytically inactive mutants, PDF(E133A) or MAP(H79A), for ribosome binding measurements (Copik et al., 2003; Lowther et al., 1999; Rajagopalan et al., 2000).

The equilibrium dissociation constants (K_d) of PDF(E133A) and MAP(H79A) for the non-translating 70S ribosome are 7.3 ± 0.7 μM and 5.4 ± 0.8 μM, respectively, comparable to albeit slightly higher than the reported values of 2.7 μM and 2.4 μM using the wild-type enzymes (Bingel-Erlenmeyer et al., 2008; Sandikci et al., 2013) (Figs. 3.3C and D). The presence of the nascent chain does not affect the ribosome binding affinity of PDF (Fig. 3.3C). The FtsQ, PhoA and Luc nascent chains modestly stabilized the ribosome-MAP interaction by 2–3 fold (Fig. 3.3D). Nevertheless, substrates with 10-100 fold difference in reaction rates differ in K_d by < 3 fold (*cf*. FtsQ and FtsQN8; Luc and 2A8L; Fig. 3.3D). Thus, differences in enzyme-ribosome binding are insufficient to account for the strong inhibition of the PDF and MAP reactions (Figs. 3.2D–G).

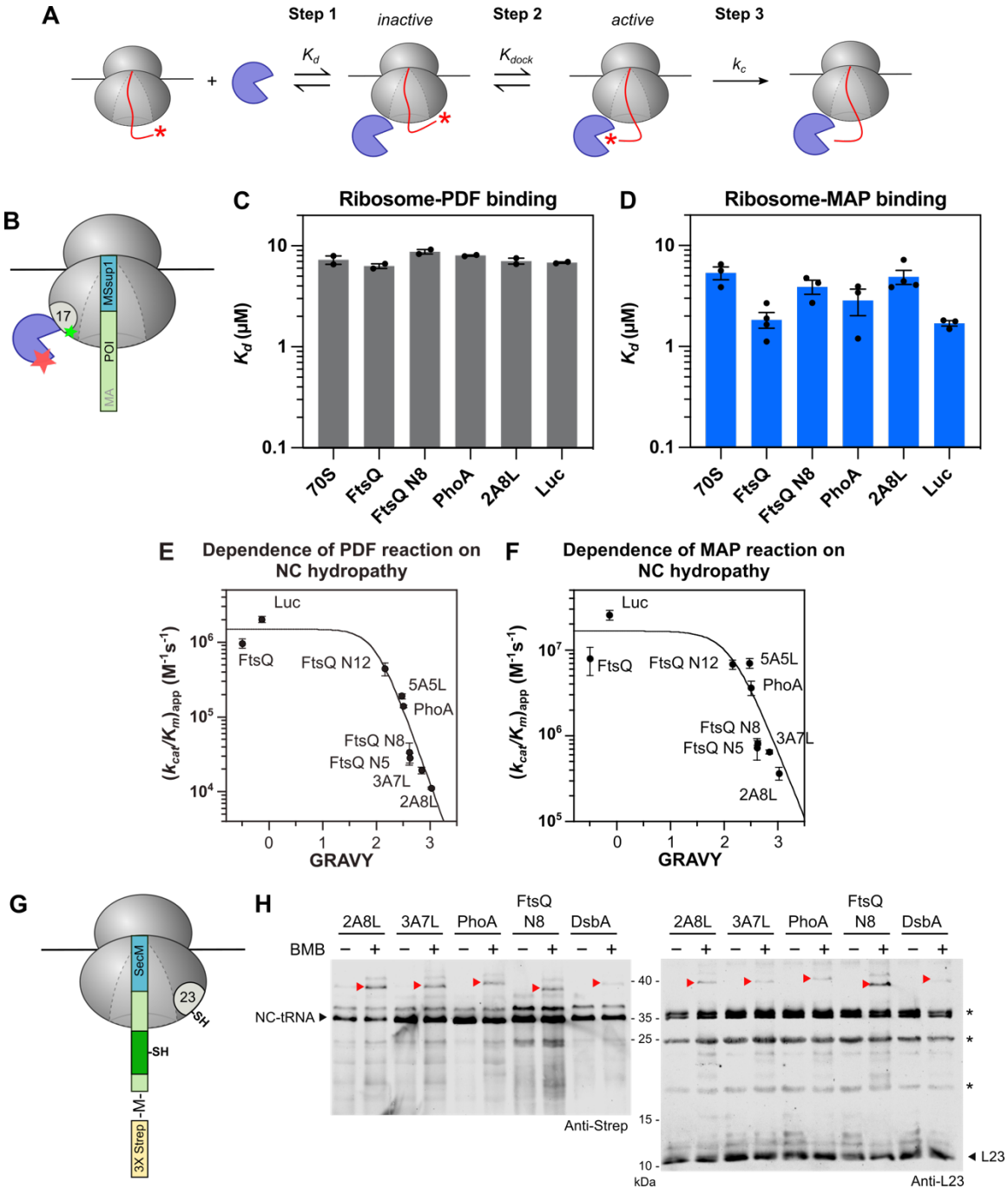
A
Step 1
inactive
Step 2
active
Step 3
K_d
K_{dock}
k_c
B
MSsup1
17
POI
MA
C
Ribosome-PDF binding
K_d (μM)
10
1
0.1
70S
FtsQ
FtsQ N8
PhoA
2A8L
Luc
D
Ribosome-MAP binding
K_d (μM)
10
1
0.1
70S
FtsQ
FtsQ N8
PhoA
2A8L
Luc
E
Dependence of PDF reaction on NC hydropathy
$(k_{cat}/K_m)_{app}$ ($M^{-1}s^{-1}$)
10^6
10^5
10^4
Luc
FtsQ
FtsQ N12
5A5L
PhoA
FtsQ N8
FtsQ N5
3A7L
2A8L
0
1
2
3
GRAVY
F
Dependence of MAP reaction on NC hydropathy
$(k_{cat}/K_m)_{app}$ ($M^{-1}s^{-1}$)
10^7
10^6
10^5
Luc
FtsQ
FtsQ N12
5A5L
PhoA
FtsQ N8
FtsQ N5
3A7L
2A8L
0
1
2
3
GRAVY
G
SecM
23
SH
SH
-M-
3X Strep
H
2A8L
3A7L
PhoA
FtsQ N8
DsbA
BMB
NC-tRNA
Anti-Strep
40
35
25
15
10
kDa
L23
Anti-L23

Figure 3.3. Interaction between the ribosome and the nascent chain regulates NME efficiency.

(A) Proposed model of PDF or MAP reactions on the RNC. **(B)** Scheme of the FRET-based binding assay. The ribosomal protein bL17 was genetically modified with a ybbR tag at the C-terminus and labeled with BODIPY-FL (green star). The nascent chain length is 67 residues for Luc and the FtsQ variants, and 69 residues for the PhoA variants. TMR (red star) was labeled at the N-terminus of PDF(E133A) or the C-terminus of MAP(H79A). **(C) and (D)** Summary of the K_d values between the indicated RNCs and PDF(E133A) (C) or MAP(H79A) (D), determined from equilibrium titrations of TMR-labeled PDF(E133A) or MAP(H79A) to 10 nM BODIPY-FL-labeled RNCs. Values are reported as mean ± SEM, with n ≥ 2. **(E, F)** Observed rate constants of the PDF (E) and MAP (F) reactions as a function of the hydropathy score of the nascent chains, defined as the GRAVY score (Kyte and Doolittle, 1982)of the most hydrophobic stretch of 11 residues that begins within the first 11 amino acids. Apparent k_{cat}/K_m values are from Figs. 3.2D–G. Lines are fits of the data to Eq. 6 in *Methods*, which describes the two-state model in (A). **(G)** Scheme of the RNCs used in the crosslinking experiments. The ribosomal protein uL23 carries a mutation S21C. A cysteine is placed near or in the TMD/signal sequence (dark green) of the model substrates, as detailed in *Methods*. The nascent chain length from the methionine to the PTC is 67 residues for FtsQN8 and DsbA, and 69 residues for the PhoA variants. **(H)** Representative western blots of the crosslinking experiment. The RNCs (500 nM) were incubated with or without 0.8 mM 1,4-bismaleimidobutane (BMB). Crosslinked products between the nascent chain and uL23 (red arrows) were detected with anti-Strep (for nascent chain) and anti-uL23 antibodies. Asterisks denote non-specific bands detected by the anti-uL23 antibody.

These results strongly suggest that the inhibitory effect of the hydrophobic N-terminal sequences on NME arises primarily from differential access of the nascent chain N-termini to the enzymes on the ribosome. To test this model, we used an established fluorescence assay in which an environmentally-sensitive probe, coumarin, at the fifth residue of RNC_{FtsQ} undergoes an increase in fluorescence upon docking at the MAP active site ((Yang et al., 2019) and Fig. S3.4A). In contrast to RNC_{FtsQ}, the coumarin fluorescence

signal of RNC_{FtsQN8} remained unchanged, suggesting a failure of proper positioning of the FtsQN8 nascent chain at the MAP active site (Fig. S3.4B).

Based on these results, we hypothesized that hydrophobic interactions with the ribosome surface confine the nascent chain N-terminus at a position inaccessible to the enzyme active sites. The interaction biases the equilibrium toward the "inactive" state, whereas weaker interaction allows the nascent chain to sample the "active" state more frequently and complete the hydrolysis step (Fig. 3.3A). To test if this model can quantitatively explain the differential reaction kinetics of the model substrates, we derived an analytical equation according to the two-state model, which describes the hydrophobic interaction as an additional activation barrier for the enzymatic reactions by disfavoring the docking equilibrium (see *Methods*). Considering the threshold length of NTE required for efficient processing (≥ 12 residues, Figs. 3.2D and E), we calculated the grand average of hydropathy (GRAVY) score of the most hydrophobic stretch of amino acids that begins within 11 residues from the N-terminus (Gasteiger et al., 2005; Kyte and Doolittle, 1982). The experimentally measured reaction rates fit well to the two-state model (Figs. 3.3E and F, *Methods*): the observed rate constants of both the PDF and MAP reactions correlate negatively with the calculated GRAVY scores for substrates with an N-terminal hydrophobic TMD/signal sequence, for which the docking equilibrium is unfavorable, but plateau at a maximum velocity for nascent chains below a threshold GRAVY score, for which the maximal occupancy of the docked state is achieved. The good agreement with data

demonstrates hydrophobic contacts of the nascent chain, presumably with the ribosome surface, as a key determinant that drive the activation of NME reactions.

The ribosomal protein uL23, together with the neighboring uL29, has been shown to constitute an interaction site for multiple nascent protein sequences and contains a hydrophobic cleft on which an emerging TMD can dock (Eisner et al., 2006; Peterson et al., 2010; Ullers et al., 2003; Wang et al., 2019). The 50 Å distance between the uL23 cleft and PDF/MAP on the ribosome is also consistent with the threshold length of the NTE (~12–13 residues in an extended conformation) required for efficient enzymatic processing of the nascent chain N-termini (Figs. S3.4C and D). These observations suggest that uL23 could constitute one of the sites on the ribosome that confine the movement of the nascent polypeptide. To test this possibility, we carried out site-specific crosslinking to test the docking of the TMD/signal sequence on uL23, taking advantage of the fact that the vicinity of the ribosome exit site is free of native cysteines (Wang et al., 2019) (Fig. 3.3G). We engineered a single cysteine on uL23 (S21C) and a second cysteine at or near the TMD/signal sequence of the nascent chain. We observed specific and prominent crosslinks between the nascent chain and uL23 on RNCs bearing a TMD/signal sequence (Fig. S3.4E, F and Fig. 3.3H), indicating that nascent chains can dock on uL23 and sample a conformation that disfavors their enzymatic processing by PDF and MAP. Nevertheless, the efficiency of crosslink with L23 does not correlate with the NME reaction kinetics, strongly suggesting

that additional sites surrounding the ribosome exit tunnel contribute to the sequestration of the nascent chain.

RPBs modulate the accessibility of nascent chains to regulate NME.

At the ribosome tunnel exit, multiple RPBs coordinate for access to the nascent protein and can potentially regulate NME (Kramer et al., 2019). This includes SRP, which recognizes N-terminal TMDs and strongly hydrophobic signal sequences to mediate membrane targeting, and TF, which engages cytosolic proteins and a subset of the secretory proteome (Ariosa et al., 2015; Kramer et al., 2019). To test this possibility, we measured the NME reactions on the model RNC_{FtsQ} and RNC_{PhoA} variants in the presence of SRP and TF (Figs. 3.4A–D).

Although RNC_{FtsQ} is a *bona fide* SRP substrate, the presence of SRP affected the PDF and MAP reactions by less than two fold (Figs. 3.4A and C, blue bars), consistent with previous results and the efficient cotranslational NME of FtsQ in the cell extract (Yang et al., 2019) (Fig. 3.1G). With substrates in which the NTE is ≤12 residues, SRP induced 50 to >100-fold inhibition of the PDF and MAP reactions, respectively (Figs. 3.4A and C, blue bars), in agreement with the observations by Ranjan *et al.* (Ranjan et al., 2017). SRP did not significantly affect the NME of substrates with weak signal sequences (RNC_{5A5L} and RNC_{PhoA}). However, reactions on the more strongly hydrophobic RNC_{3A7L} and RNC_{2A8L} substrates were slowed ~10- and > 50-fold by SRP, respectively (Figs. 3.4B and D, blue

bars). The SRP-induced inhibition was not due to weakened binding of the enzymes to the RNC, as direct binding assays detected a <3-fold effect of SRP on the RNC binding affinity of PDF or MAP (Figs. 3.4E and F), consistent with previous observations (Bornemann et al., 2014). These results show that SRP regulates the NME reactions on substrates with an N-terminal TMD/signal sequence, likely by confining the membrane targeting sequences to its signal sequence-binding M-domain at the ribosome tunnel exit and thus excluding the access of the N-termini to PDF and MAP (Jomaa et al., 2016; Schaffitzel et al., 2006).

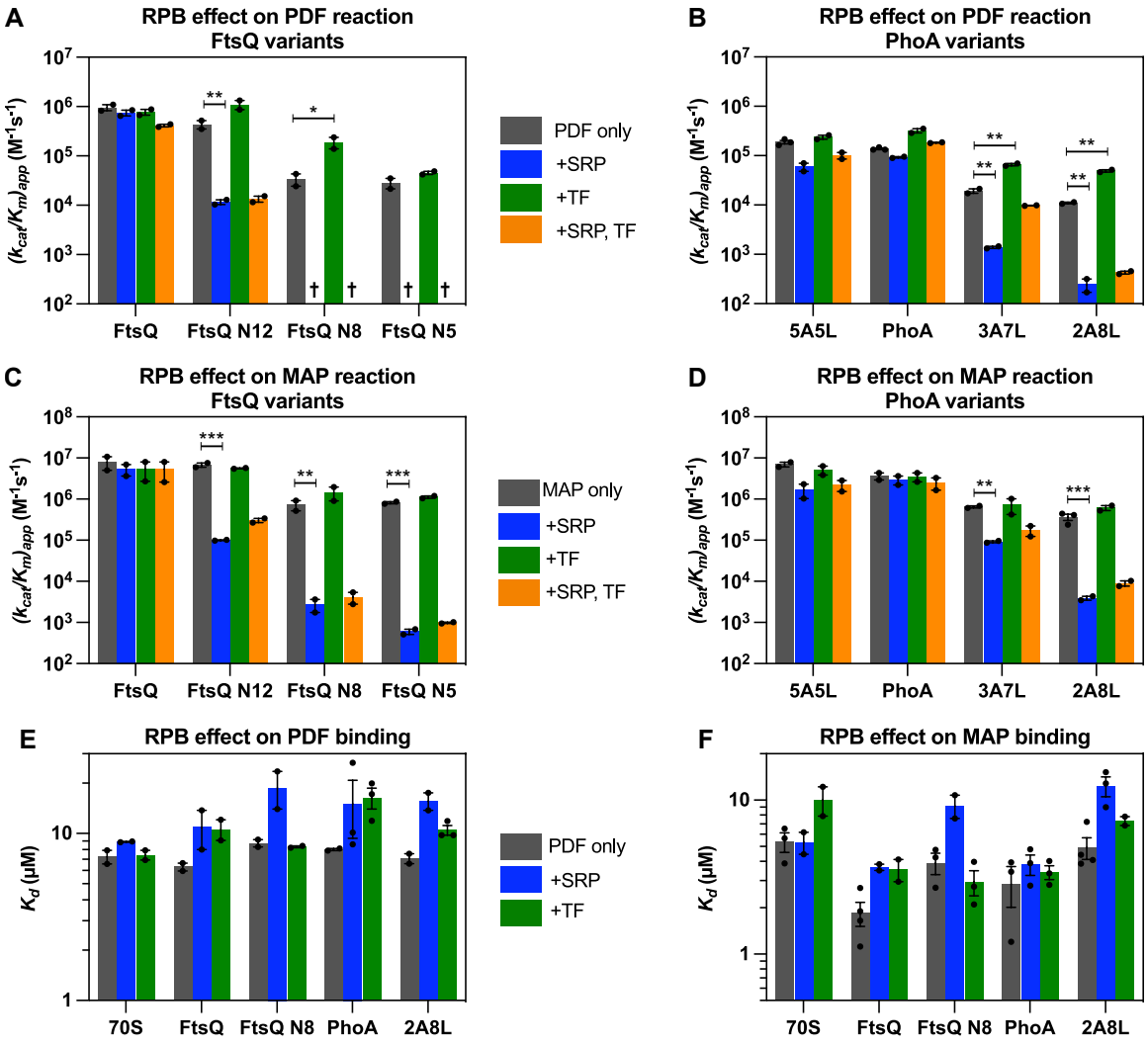

Figure 3.4. RPBs regulate the NME reactions primarily by reorienting the nascent chain.

(A-D) The effect of RPBs (400 nM SRP, 5 μM TF, or both) on the PDF (A, B) and MAP (C, D) reactions with the FtsQ (A, C) and PhoA nascent chain variants (B, D). Reactions were carried out as described in Figure 3.2. Daggers indicate that $(k_{cat}/K_m)_{app}$ is < 200 $M^{-1}s^{-1}$. Statistical tests were carried out on $\log(k_{cat}/K_m)_{app}$ values using unpaired t-tests, where '*', '**' and '***' represent $p < 0.05$, 0.01, and 0.001, respectively. **(E) and (F)** The effect of RPBs (400 nM SRP or 5 μM TF) on the binding affinity of PDF(E133A) (E) and

MAP(H79A) (F) for the indicated RNCs. The K_d measurements were carried out as described in Figs. 3.3B–D. All values are reported as mean ± SEM with n ≥ 2.

Unexpectedly, TF accelerated the PDF reactions on substrates with a hydrophobic N-terminal sequence/TMD by 3-5 fold (Fig. 3.4A–B, FtsQ N8, 3A7L, and 2A8L, green bars). The RNC binding affinity of PDF and MAP was unaffected or slightly weakened (< 2-fold) by TF, arguing against facilitated recruitment of the enzymes as the source of the TF-induced rate enhancement (Fig. 3.4E). Importantly, TF induced cysteine-specific crosslinks between the signal sequence and an engineered cysteine on uL22 (S30C) (Fig. S3.5), suggesting that TF brings the nascent chain close to uL22 near the PDF and MAP binding sites (Merz et al., 2008; Saio et al., 2014). The effects of SRP and TF on the PDF reaction counteract each other for a substrate with modest hydrophobicity (Figs. 3.4B, 3A7L), whereas the inhibitory effect of SRP dominates for substrates with strongly hydrophobic N-terminal targeting signals (Figs. 3.4A, B, FtsQ N8, FtsQ N5, and 2A8L). Thus, the interplay between SRP and TF on the RNCs enables intricate regulation of NME on a broad spectrum of substrates.

To further dissect the roles of the ribosome surface and RPBs in regulating the NME efficiency of the model substrates, we leveraged a previously established computational model (Yang et al., 2019), which uses parametrized PDF and MAP reaction rates on RNC based on experimental data to numerically calculate the extent of NME of model substrates during ongoing protein synthesis in cell lysate. This analysis showed that, in the absence of RPBs, the 2A8L and 3A7L nascent chains underwent ~10% and 20% cotranslational NME,

respectively, when 300 residues are synthesized (Fig. S3.6A). NME was abolished in the presence of SRP, while the additional presence of TF allowed ~10% NME on 3A7L (Figs. S3.6B and C). These results indicate that during continuous protein synthesis, the N-terminal hydrophobic sequences on nascent proteins is sufficient to suppress their cotranslational NME, but the presence of SRP and TF leads to more complete inhibition.

Proteins with hydrophobic N-terminal targeting signals are resistant to NME in vivo

To quantitatively measure NME efficiency *in vivo*, we designed a reporter-based assay. We constructed an arabinose-inducible bicistronic plasmid, in which the model substrate and the control protein TrxA are encoded after two separate Shine-Dalgarno sequences (Fig. 3.5A). The proteins were expressed in *E. coli* cells, pulse-labeled with ^{35}S-Met/Cys, and immunoprecipitated via the C-terminal FLAG tag. All the internal methionine and cysteine residues on the model substrates were removed such that the radioactive signal reports on the retention of iMet (Figs. 3.5B, D and F, "*iMet*" lanes). Wild-type substrates containing native methionines and cysteines were measured simultaneously ("*6M*" and "*8M4C*" lanes) to control for different expression levels of the model substrates. We first measured the *in vivo* NME of full-length FtsQ with varying residues at the second position (Figs. 3.5B and C). Consistent with the sequence specificity of MAP (Frottin et al., 2006), the retention of iMet on these substrates strongly correlated with the size of the second

residue, suggesting that the assay faithfully reports on the NME efficiency of model substrates *in vivo*.

To understand the effect of a hydrophobic N-terminal targeting signal on NME *in vivo*, we tested the FtsQ variants in which the NTE is systematically truncated. All FtsQ variants were successfully integrated into the membrane and, except for FtsQ-N5, adopted the correct Type-II topology, excluding artifacts such as protein misfolding (Figs. S3.7, A-C). Consistent with the analysis in the reconstituted system and in cell extract, we observed significant accumulation of iMet on substrates with an early TMD, comparable to the strongly disfavored NME substrate with lysine at the second residue (Figs. 3.5D and E). Significant iMet retention was also observed with FtsQ-N8 and FtsQ-N5 in cells lacking methionyl-tRNA formyltransferase (Δ*fmt*), in which deformylation is bypassed for NME, providing direct evidence for inhibition of the MAP reaction *in vivo* (Figs. S3.7D and E). Similarly, we carried out *in vivo* NME assays on the PhoA signal sequence variants. The mutation A21L prevents cleavage of the signal sequence by leader peptidase, allowing us to monitor the N-terminal modification of the substrate (Karamyshev et al., 1998). We observed increased retention of iMet on 3A7L and 2A8L compared to 5A5L and PhoA (Figs. 3.5F and G), in good agreement with our *in vitro* experiments. Collectively, these results show that a hydrophobic membrane targeting sequence near the N-terminus of a protein is a strong inhibitory signal for NME *in vivo*.

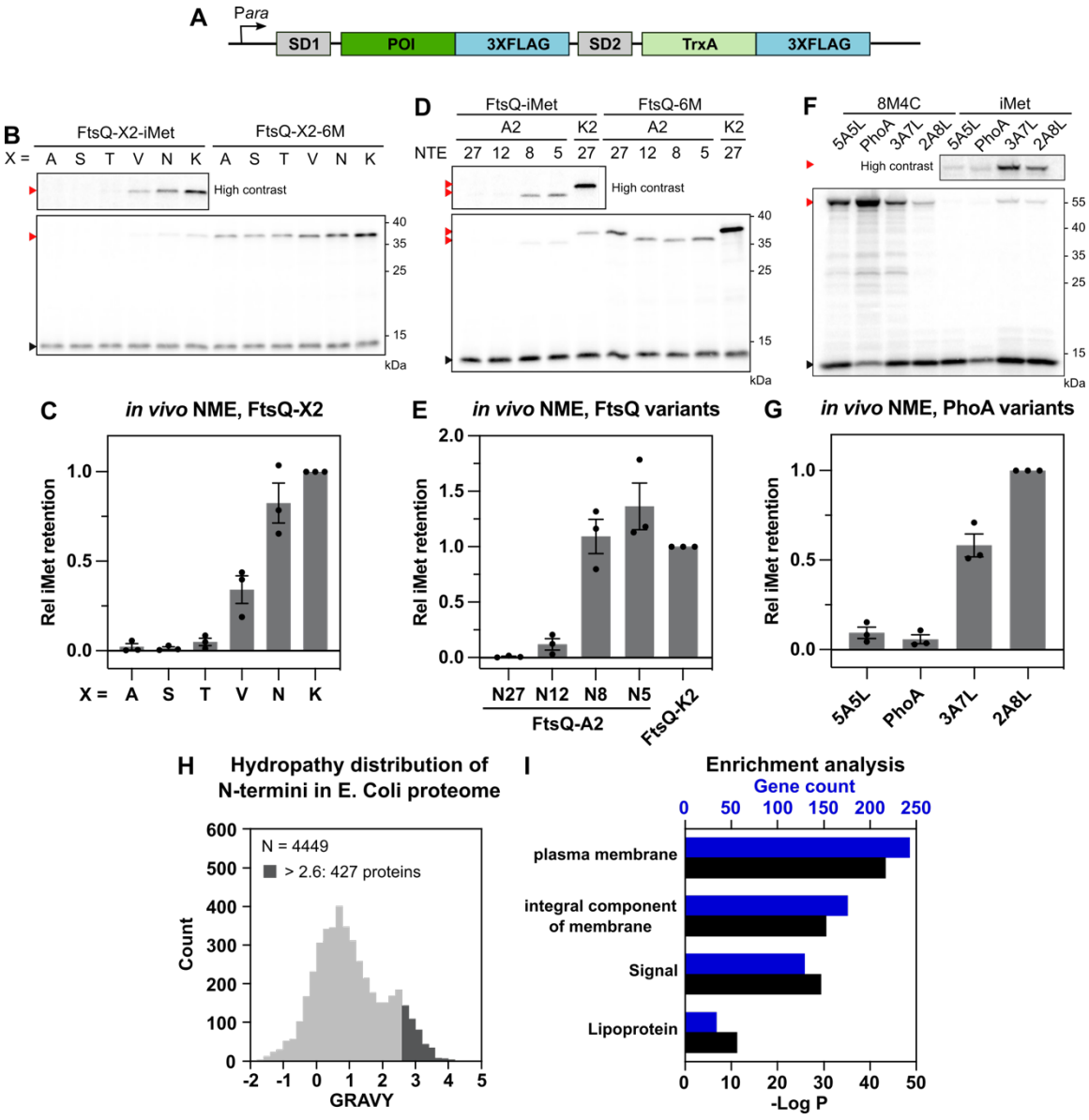

Figure 3.5. Proteins with an early TMD or hydrophobic signal sequence are resistant to NME *in vivo*.

(A) Scheme of the model substrates used in the *in vivo* NME assay. The protein of interest (POI) and the control protein TrxA was tagged with a C-terminal 3X FLAG tag and expressed from a bicistronic plasmid under the control of an arabinose promoter (P_{ara}) and their respective Shine-Dalgarno sequences (SD1 and SD2). **(B)** *In vivo* NME of model

FtsQ-X2 variants (red arrows), in which the second residue (X2) was mutated to the indicated amino acids. The substrates were induced in the *E. coil* strain CAG12184 and pulse-labeled with ^{35}S-Met/Cys for 10 min, immunoprecipitated, and analyzed by autoradiography. The signal of the *iMet* constructs, in which all six internal methionines were replaced with leucine, indicates the retention of iMet. The signal of the *6M* constructs, which retain the six native methionines, serves as the control for protein expression level. TrxA (black arrows) serves as the loading control. **(C)** Quantification of the data in (B) and their replicates. The *iMet* signal was divided by the *6M* signal to account for variations in expression level and normalized to that of FtsQ-K2, which completely retains the iMet. Values are reported as mean ± SEM, with n = 3 biological replicates. **(D)** *In vivo* NME of FtsQ truncation variants, measured as in (B). **(E)** Quantification of the data in (D) and their replicates. Values are normalized to FtsQ-K2 and reported as mean ± SEM, with n = 3 biological replicates. **(F)** *In vivo* NME of PhoA-A21L variants (red arrows), measured as described in (B). The *8M4C* constructs contain the 8 native methionines and 4 native cysteines in PhoA and serves as controls for variations in expression levels. The second residue is alanine in all PhoA variants. **(G)** Quantification of the data in (F) and their replicates. Values are normalized to that of 2A8L and reported as mean ± SEM, with n = 3 biological replicates. **(H)** Distribution of the hydropathy of the N-terminal sequences in the *E. coli* proteome, calculated as in Figs. 3.3G and H. Proteins bearing N-terminal sequences with GRAVY scores > 2.6 (comparable to or more hydrophobic than FtsQ N8) are colored in dark gray. **(I)** Enriched functional annotation terms (Gene Ontology and Uniprot Keywords) associated with the 426 proteins highlighted in (F).

Based on these *in vivo* NME measurements and the two-state model derived from *in vitro* kinetic analysis, proteins with N-terminal signal sequences comparable to or more hydrophobic than FtsQ-N8 and 3A7L are anticipated to retain fMet *in vivo*. We therefore calculated the GRAVY score of the most hydrophobic segment close to the N-terminus across the *E. coli* proteome (Fig. 3.5H), as described for the model substrates in Figs. 3.3E and F. This analysis predicted that 427 proteins, predominantly composed of inner membrane, periplasmic, and outer membrane proteins, are subject to this regulation (Fig. 3.5I). Consistent with our prediction, several studies reported the retention of the formyl group on

multiple membrane proteins with an early TMD (Bienvenut et al., 2015; Milligan and Koshland Jr, 1990; Sebald and Wachter, 1980; vonHeijne, 1989). These results strongly suggest that, despite the promiscuity of PDF, a non-trivial fraction of the proteome retains fMet, which may provide an embedded regulatory signal on the nascent protein.

3.3. Discussion

NME is a ubiquitous protein modification essential for cell viability and occurs in an obligatorily cotranslational mechanism. While the structure and enzymology of NME enzymes have been extensively studied based on peptide substrates and proteomics data, whether and how this modification is regulated at the ribosome tunnel exit in coordination with other protein biogenesis pathways remain unclear. Our work here demonstrates that hydrophobic membrane targeting signals on the nascent protein impose an overriding layer of regulation on NME *in vitro* and *in vivo*. Kinetic analyses combined with crosslinking experiments suggest the role of hydrophobic interactions between the nascent chain and the ribosomal surface in driving the activation of the enzymatic reactions. The NME regulation is further enforced by the targeting factor SRP, exemplifying the active role of the ribosome in modulating nascent protein biogenesis pathways.

Emerging data show that the ribosome is not only a protein synthesis machine, but also actively participates in diverse protein biogenesis pathways (Koubek et al., 2021; Kramer et al., 2019). In addition to providing a platform for the recruitment of multiple RPBs,

the ribosome interacts with diverse nascent polypeptides both within the exit tunnel and on the ribosome surface (Cassaignau et al., 2021; Cruz-Vera et al., 2005; Eisner et al., 2006; Guzman-Luna et al., 2021; Peterson et al., 2010; Ullers et al., 2003; Valent et al., 1995; Waudby et al., 2019). These interactions can regulate the rate of translation elongation as well as cotranslational protein folding (Cassaignau et al., 2021; Kaiser et al., 2011; Lu and Deutsch, 2008; Thommen et al., 2017; Waudby et al., 2019). Here, our results suggest that hydrophobic interaction of the nascent protein with the ribosome surface could also regulate their N-terminal modification. While the ribosome surface is mostly acidic, multiple proteins including uL23, uL29, uL24, and bL17/bL32 (Fedyukina et al., 2014; Guzman-Luna et al., 2021) present contiguous hydrophobic surfaces that could provide docking sites for signal sequence or TMDs ((Guzman-Luna et al., 2021) and this work), which sequester the nascent chain N-terminus from access by the NME enzymes. Moreover, the ribosome can interact with nascent chains via electrostatic and metal ion-mediated interactions (Cassaignau et al., 2021; Guzman-Luna et al., 2021; Kaiser et al., 2011). Recent studies showed that interaction of the ribosome surface with the nascent chain of phosphorylated insulin receptor (PIR) and α-synuclein clusters to a specific region near the tunnel exit, where uL23 and uL29 are located (Cassaignau et al., 2021; Deckert et al., 2021). Whether these interactions confine the conformation of other classes of nascent chains and whether such confinement influences their NME remain to be explored.

Together with previous studies, our work here explains how PDF and MAP coordinate with other RPBs at the crowded ribosome exit site. First, interaction with the ribosome dominates the binding affinity of PDF and MAP. The binding of either enzyme to the RNC is not significantly stabilized by the nascent polypeptide (this work), nor affected more than 3-fold by SRP or TF (Figs. 3.4E and F). Reciprocally, TF or SRP binding to the ribosome is weakened <2-fold by physiological amount of PDF and unaffected by MAP (Bornemann et al., 2014; Sandikci et al., 2013). These results are consistent with structural studies showing that the NME enzymes can flexibly adopt alternative binding modes on the ribosome in response to SRP and TF binding (Akbar et al., 2021; Bhakta et al., 2019; Bornemann et al., 2014; Sandikci et al., 2013). Coupled with their high ribosome association and dissociation rates, both enzymes can rapidly scan a variety of translating ribosomes for substrates (Sandikci et al., 2013; Yang et al., 2019). Secondly, efficient NME initiates for nascent chains as short as 45 amino acids (Sandikci et al., 2013; Yang et al., 2019), and the irreversible chemical steps of the PDF and MAP reactions are rapid for an optimal N-terminus (k_{cat} > 200 s^{-1} for PDF and >30 s^{-1} for MAP (Ragusa et al., 1998; Yang et al., 2019)). Thus, the action of the NME enzymes on optimal substrates are kinetically privileged compared to the other RPBs. Notably, although physiological concentrations of SRP reduced the rates of the PDF and MAP reactions on $RNC_{FtsQ\text{-}N12}$ by ~20 fold, FtsQ-N12 underwent efficient NME in the extract and *in vivo*, likely reflecting this kinetic privilege. Finally, NME of suboptimal substrates is further restricted to a limited time window during translation.

Nascent chains with large side chains at the second residue are inhibited by SRP and TF at nascent chain lengths below 67 residues and above 82 residues (Yang et al., 2019). Proteins with an early TMD or signal sequence are targeted to the plasma membrane as soon as their membrane targeting motifs emerge from the ribosome, and are thus quickly removed from access by the NME enzymes (this work).

Our results indicate that other RPBs could regulate NME by tuning the accessibility of the nascent chain N-termini to the enzyme. SRP, with an M-domain that engages hydrophobic signal sequences/TMDs at the ribosome tunnel exit, restricts the sampling of the nascent chain, such that only membrane proteins with a long extension preceding the TMD efficiently undergo NME. TF, which forms a cradle to protect patches of hydrophobic amino acids on an elongating nascent protein, brings the nascent chain near the PDF/MAP docking site on the ribosome and could modestly stimulate NME. The two RPBs counteract one another, but SRP dominates on substrates with strongly hydrophobic membrane targeting signals, reflecting the specificity of this targeting factor (Ariosa et al., 2015). Moreover, regulation of NME by RPBs is substrate- and nascent chain length-dependent. While TF enhances the PDF reaction on substrates with N-terminal targeting signals, it inhibits NME on cytosolic proteins and unstructured nascent chains beyond the optimal length, suggesting its versatile role in modulating nascent protein modification (Oh et al., 2011; Sandikci et al., 2013; Yang et al., 2019). In addition to SRP and TF, SecA and DnaK also interact with hydrophobic nascent polypeptides (Deuerling et al., 1999; Huber et al.,

2017). However, stable binding of SecA to RNCs requires the synthesis of >100 residues (Huber et al., 2017), including the periplasmic domain of RodZ, a membrane protein that depends on SecA for its cotranslational targeting (Wang et al., 2017). DnaK does not bind to the ribosome and is generally considered to act downstream of TF during protein synthesis (Deuerling et al., 2003). Considering their late engagement during protein maturation, SecA and DnaK are unlikely to significantly affect the NME reactions and their regulation by SRP and TF under physiological conditions.

Our results here, together with previous work, provide a more complete model for how the NME enzymes mediate efficient and selective cotranslational processing of a large fraction of the bacterial proteome (Fig. 3.6). Although both PDF and MAP are sub-stoichiometric to translating ribosomes in cells (Meinnel et al., 1993), their rapid ribosome binding and dissociation rates enable these enzymes to scan translating ribosomes for the emerging nascent polypeptide (Step 1) ((Bornemann et al., 2014; Sandikci et al., 2013; Yang et al., 2019) and this work). Ribosome binding greatly increases the effective enzyme concentration with respect to the nascent protein, enabling rapid processing of optimal substrates. On the other hand, the interaction of nascent proteins with the ribosome surface regulates the flexibility of the nascent chain and its ability to search for and access the enzyme active site. Cytosolic proteins and secretory proteins with weakly hydrophobic signal sequences can readily dock at the enzyme active site, where the nascent protein is deformylated by PDF (Step 2) followed by excision of iMet if the second residue is small

(Step 3). In contrast, an early TMD or hydrophobic signal sequence confines the nascent chain on the ribosome surface at a site away from the enzymes, such as on uL23, and inhibits their access to and processing by both enzymes (Step 4). Recruitment of SRP, which engages the signal sequence/TMD in the M-domain at the ribosome tunnel exit, further precludes the N-termini from reaching the enzyme active sites (Step 5). Together, these effects lead to the retention of fMet on a significant fraction of the membrane and secretory proteome (Step 6).

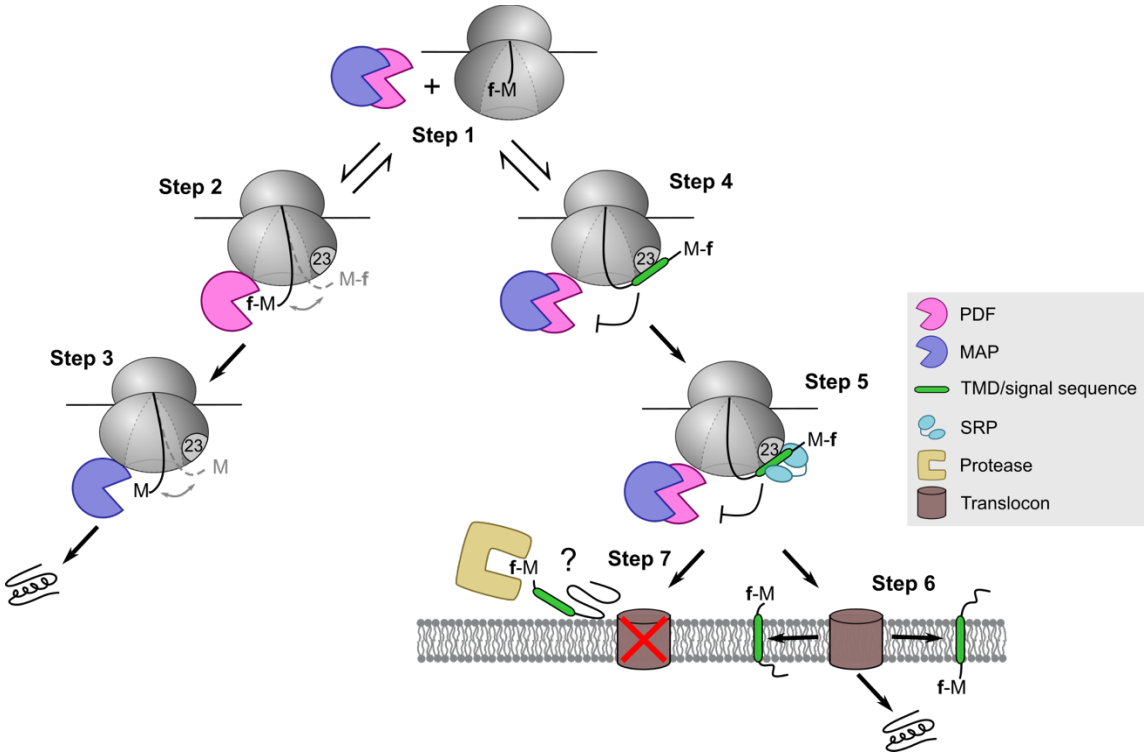

Figure 3.6. Model for the regulation of NME by interaction of the nascent chain with the ribosome surface and with SRP.

PDF and MAP rapidly scan translating ribosomes for emerging nascent proteins (Step 1). Proteins without strongly hydrophobic sequences freely access the enzyme active site,

allowing efficient processing by PDF (Step 2) and MAP (Step 3) given a small penultimate residue. On the other hand, an N-terminal TMD or hydrophobic signal sequence interacts with the ribosome surface and is precluded from reaching the NME enzymes (Step 4), which is exacerbated by SRP (Step 5). The NME inhibition leads to fMet retention on a significant fraction of the membrane and secretory proteome (Step 6), and may potentially enable their quality control in case of failed translocation (Step 7).

The function of fMet retention remains an outstanding question. The significant enrichment of membrane and secretory proteins in the NME-inhibited proteome suggests potential roles of fMet in the biogenesis and/or quality control of these proteins. Diverse roles in the folding, assembly, and quality control of proteins have been described for N-terminal acetylation, a modification that is chemically similar to the formyl group (Aksnes et al., 2019; Fauvet et al., 2012; Hwang et al., 2010; Scott et al., 2011). Previous studies also suggested that fMet can serve as a degradation signal for bacterial and yeast proteins (Kim et al., 2018; Piatkov et al., 2015). Although not yet identified, the protease responsible for the fMet/N-degron pathway in bacteria resides in the cytoplasm or on the inner membrane and was proposed to be FtsH, a membrane-embedded AAA+ protease facing toward the cytoplasm (Piatkov et al., 2015). It is plausible that fMet enables the degradation of membrane/secretory proteins that fail in targeting and/or translocation (Fig. 3.6, Step 7). While membrane proteins with long and flexible terminus can be recognized and degraded readily (Chiba et al., 2000, 2002), the retention of fMet on proteins with an early signal sequence or TMD may provide an alternative recognition signal for quality control pathways and facilitate the clearance of mislocalized proteins.

3.4. Materials and Methods

Cotranslational NME assay

The POI-N sequences and TrxA were cloned into the pK7-derived plasmids using Gibson cloning and Fastcloning techniques to generate the pK7-POI-TrxA plasmids (Gibson et al., 2009; Jewett and Swartz, 2004; Li et al., 2011; Yang et al., 2019). All internal methionine residues and the second residue of each POI-N were replaced with alanine. DNA fragments encoding the T7 promoter, T7 terminator and the model substrates were PCR-amplified from pK7-POI-TrxA, transcribed, and translated *in vitro* in E. coli S30 extracts containing ^{35}S-methionine as described (Yang et al., 2019), and analyzed by SDS-PAGE and autoradiography. Where indicated, the control reactions contained 5 μM actinonin (ACT). Cotranslational NME efficiency is quantified as $\left(1 - \frac{I_{-ACT}}{I_{+ACT}}\right) \times 100\%$, where I indicates the ^{35}S signal from the substrate.

Cotranslational deformylation assay

A Strep tag was introduced to the C-terminus of thioredoxin in the pK7-POI-TrxA constructs for the indicated model substrates to generate the pK7-POI-TrxA-Strep plasmids. The substrates were translated as described for the cotranslational NME assay and immunoprecipitated using Strep-tactin Sepharose resin. Purified substrates were digested with proteinase K (1 mg/mL, 37 °C, overnight), and radioactive Met and fMet were analyzed

by thin-layer chromatography (Millipore Silica gel 60, n-butanol: acetic acid: water = 5: 3: 2) and autoradiography (Ranjan et al., 2017). Cotranslational deformylation efficiency is quantified as $\left(1 - \frac{I_{-ACT}}{I_{+ACT}}\right) \times 100\%$, where I indicates the ^{35}S signal from the fMet species.

Protein expression and purification

Wild-type PDF, MAP, MAP-H79A, SRP, and TF were expressed and purified as described (Agashe et al., 2004; Peluso et al., 2001; Yang et al., 2019).

To construct the expression plasmid for PDF-E133A, an 11-residue ybbR tag was fused to the protein coding sequence, and subcloned into pET28a vector containing a cleavable N-terminal His_6-SUMO tag (Yin et al., 2005). To express PDF-E133A, BL21 star (DE3) cells were induced at OD = 0.6 with 0.5 mM IPTG at 30 °C for 3 h, and lysed by sonication in buffer A (20 mM Hepes-KOH, 300 mM NaCl, 0.2 mM $CoCl_2$, 10% glycerol, 1 mM TCEP, pH 7.5) containing protease inhibitor cocktail (GoldBio). Clarified lysates were purified with Ni-NTA resin, and the His_6-SUMO tag was removed by overnight dialysis in the presence of His_6-Ulp1 protease against buffer B (20 mM Hepes-KOH, 20 mM NaCl, 10% glycerol, pH 7.5). Tag-less proteins were further purified over a Ni-NTA column, supplemented with 100 mM NaCl, 0.2 mM $CoCl_2$, 1 mM TCEP, and 50% glycerol, and stored in –30 °C.

Fluorescence labeling

MAP-H79A containing a C-terminal GLPATGG tag was labeled with TMR (Invitrogen) via sortase-mediated reactions as described (Guimaraes et al., 2013; Yang et al., 2019).

PDF-E133A was labeled with TMR at the N-terminus using Sfp-mediated reaction (Yin et al., 2005). The labeling reaction was carried out in Sfp buffer (50 mM Hepes-KOH, 10 mM $MgCl_2$, pH 7.5) containing 50 μM PDF-E133A, 10 μM His_6-tagged Sfp and 50 μM CoA-TMR conjugates, and incubated at room temperature for 1 h. The reaction mixture was passed through TALON resin to remove Sfp. Excess dye conjugates were removed using a PD-10 column (GE). Labeling efficiency was ~ 80%.

RNC purification

RNCs for enzymatic reactions. Radiolabeled RNCs were generated and purified as described previously (Yang et al., 2019). Briefly, the DNA templates were *in vitro* translated in E. coli S30 extracts containing ^{35}S-methionine and 5 μM actinonin. The reaction mix was purified through 10–50% sucrose gradient fractionation centrifugation in a SW32 rotor (Beckmann Coulter, 23,000 rpm, 15 h, 4 °C) and the 70S fractions were collected.

RNCs for Nascent chain-MAP docking. Coumarin-labeled RNCs were generated via the amber suppression technique by *in vitro* translating the DNA templates in S30 extracts of an E. coli strain KC6 expressing $tRNA_{CUA}$ in the presence of 220 μM L-(7-

hydroxycoumarin-4-yl)ethylglycine (Cm), 12 μM purified Cm tRNA synthetase and 5 μM actinonin, as described (Saraogi et al., 2011). 70S ribosomes were isolated via sucrose gradient fractionation as described above.

RNCs for the fluorescence binding assay. The coding sequence for human ubiquitin, UBA52, was subcloned from pHUE (Catanzariti et al., 2004) and inserted between a 3X Strep tag and the nascent chain sequence on pK7-derived plasmids via Gibson cloning. An 8-residue Ms-sup1 stalling sequence was placed at the C-terminus of the nascent chain sequence (Yap and Bernstein, 2009). DNA templates were *in vitro* translated in S30 extracts from the E. coli strain containing a ybbR tag at the C-terminus of bL17 (KC6 ΔrplQ::kan $pL17_{ybbR}$), and the reactions were loaded on a Strep-tactin column. Purified RNCs were labeled with BODIPY-FL (Invitrogen) in reactions containing 1 μM RNC, 4 μM Sfp, and 4 μM BODIPY-FL-CoA at room temperature for 2 h. The reactions also contained 1 μM deubiquitinylating enzyme (Usp2-cc) (Catanzariti et al., 2004) to remove the 3X Strep-ubiquitin moiety and expose the methionine on the nascent chain. Labeled RNCs were further purified through a sucrose cushion centrifugation.

RNCs for the crosslinking assay. The plasmids for RNCs used in the crosslinking assay were constructed by placing the nascent chain sequences between an N-terminal 3X Strep tag and a C-terminal SecM stall sequence in pK7-derived plasmids. Cysteine mutations were placed at the end of the signal sequences for the PhoA variants (T16C), in the middle

of the TMD for FtsQ N8 (T14C), and in the middle of the signal sequence of DsbA (G15C) via site-directed mutagenesis. The DNA templates were *in vitro* translated in S30 extracts from the E. coli strains carrying a cysteine mutation at uL22 (KC6 ΔrplV::kan $pL22_{S30C}$) or uL23 (KC6 ΔrplW::kan $pL23_{S21C}$), and the RNCs were purified via Strep-tactin resin.

To generate E. coli strains KC6 ΔrplQ::kan $pL17_{ybbR}$, KC6 ΔrplV::kan $pL22_{S30C}$ and KC6 ΔrplW::kan $pL23_{S21C}$, the strain KC6 (Calhoun and Swartz, 2006) was transformed with the plasmid pEK20 encoding C-terminal ybbR-tagged bL17, uL22-S30C, or uL23-S21C. The respective genomic ribosomal protein genes were subsequently knocked out via lambda-red recombination (Datsenko and Wanner, 2000; Wang et al., 2019).

Enzymatic assays on purified RNC.

Deformylation assay. The measurements were carried out manually or using an RQF-3 Quench-flow instrument (KinTek) as described previously (Yang et al., 2019). The reaction was initiated by mixing 20 nM ^{35}S-labeled RNC with an equal volume of PDF at sub-saturating concentrations in assay buffer (50 mM Hepes-KOH, 150 mM KOAc, 10 mM $Mg(OAc)_2$, 0.1 mM $CoCl_2$, and 1 mM TCEP, pH 7.5), and quenched with an excess amount of ACT at specific time points. Excess MAP was added subsequently to release deformylated methionine, which remains soluble after treatment with 15% trichloroacetic acid (TCA). The mixture was centrifuged, and the TCA-soluble ^{35}S-Met signal in the supernatant was quantified by scintillation counting.

Methionine cleavage assay. Measurements were carried out as described previously (Yang et al., 2019). Briefly, 20 nM of ^{35}S-labeled RNC was first deformylated by incubation with 100 nM PDF. The reaction was initiated by adding equal volume of MAP at sub-saturating concentrations and quenched with 15% TCA at specific time points. The released ^{35}S-Met was quantified as described above and previously (Yang et al., 2019).

The amount of released methionine in the deformylation and methionine cleavage assays was normalized to the total amount of nascent chains and fit to Eq. 1,

$$\frac{[Met]}{[RNC]_0} = C(1 - e^{-k_{obs}t}) \qquad \text{Eq. 1}$$

where k_{obs} is the observed rate constant, and C is the maximum fraction of RNC that can be processed. The k_{obs} was then divided by the enzyme concentration used during the reaction to obtain an apparent k_{cat}/K_m value.

Fluorescence measurements

All fluorescence measurements were performed on Fluorolog-3 (HORIBA).

Equilibrium titrations to measure ribosome-PDF and ribosome-MAP binding. The measurement was carried out with 10 nM BODIPY-labeled RNC in assay buffer with 1 mg/mL BSA to prevent nonspecific binding. Increasing amount of TMR-labeled PDF-

E133A or MAP-H79A was added into the reaction, and the fluorescence emission at 515 nm was recorded at the excitation wavelength of 485 nm. The FRET efficiency was calculated according to Eq. 2,

$$FRET = 1 - \frac{F_{DA}}{F_D} \quad \text{Eq. 2}$$

where F_{DA} and F_D are the fluorescence signals with and without the acceptor, respectively, after corrections for dilution and environmental sensitivity using parallel titrations with unlabeled PDF-E133A or MAP-H79A.

The FRET efficiency was fit to the Michaelis-Menten equation (Eq. 3),

$$FRET = A \times \frac{[E]}{K_d + [E]} \quad \text{Eq. 3}$$

where A denotes the FRET efficiency at saturated condition, [E] is the concentration of PDF-E133A or MAP-H79A, and K_d is the dissociation constant between the RNC and PDF or MAP.

Nascent chain-MAP docking. The experiment was carried out using Cm-labeled RNC_{FtsQ} and $RNC_{FtsQ\ N8}$ as described previously (Yang et al., 2019). Briefly, 10 nM of RNC

and indicated amount of MAP-H79A were mixed, and the emission spectrum was recorded at the excitation wavelength of 360 nm.

Crosslinking assays

500 nM RNCs carrying Cys mutations were reduced in crosslinking buffer (50 mM Hepes-KOH, 150 mM KOAc, 10 mM $Mg(OAc)_2$, pH 7.0) with 5 mM TCEP at room temperature for 30 min, followed by incubation with 0.8 mM 1,4-bis(maleimido)butane (BMB) or 1,4-bis(maleimido)hexane (BMH) for 1 h. The reaction was quenched with 50 mM DTT, and analyzed by Western blot using indicated antibodies. Anti-Strep and anti-HA were purchased from Genscript and anti-uL23 was customized from Genscript as previously described (Wang et al., 2019).

Two-state model

Considering a two-state model (depicted in Fig. 3.3A), in which the active and inactive states are rapidly exchanging before proceeding to the irreversible chemistry step,

$$inactive \overset{K_{dock}}{\rightleftharpoons} active \overset{k_c}{\rightarrow} product \qquad \text{Eq. 4}$$

The free energy change (ΔG) between the inactive and active states is driven by the hydrophobic interaction between the nascent chain N-terminus and uL23, and thus related to the hydropathy (Φ) of the N-terminus,

$$\Delta G = \Delta G_0 + a \cdot \Phi \qquad \text{Eq. 5}$$

where ΔG_0 describes the intrinsic free energy term independent of N-terminus hydropathy, and a is a constant of proportionality. The observed rate constant (k_{obs}) is proportional to the fraction of the active state and can be described by Eq. 6,

$$k_{obs} = k_{max} \times \frac{1}{1 + e^{-\frac{\Delta G}{kT}}} = \frac{k_{max}}{1 + e^{-\frac{\Delta G_0}{kT} - \frac{a \cdot \Phi}{kT}}} \qquad \text{Eq. 6}$$

where k_{max} denotes the maximal rate constant when the active fraction approaches unity, k is the Boltzmann constant, and T is the temperature in the kelvin scale.

To define Φ, we used the Kyte and Doolittle scale (Kyte and Doolittle, 1982) to calculate the grand average of hydropathy (GRAVY) and searched with an 11-residue rolling window from the N-terminus of the nascent chain, given that the hydrophobic cleft on uL23 can accommodate a helical peptide of 11-13 residues (Wang et al., 2019). Based on the distance between the cleft and the enzyme active sites (Figs. S3.4C and D), the GRAVY score of the most hydrophobic segment that begins at or before the 11th residue from iMet was plotted against the observed rate constant of the PDF or MAP reaction, and fit to Eq. 6 (Figs. 3.3E and F).

Simulation for cotranslational NME

Numerical simulations of cotranslational NME under single turnover conditions were carried out as described previously (Yang et al., 2019). This model considers sequential PDF and MAP reactions during protein translation in S30 lysates, in which the concentration of ribosome is in excess of actively translated nascent proteins. The irreversible pseudo-first order rate constants for PDF and MAP reactions are defined as $(k_{cat}/K_m)_{app} \times [enzyme]_{free}$, where $[PDF]_{free}$ = 130 nM and $[MAP]_{free}$ = 63 nM. $(k_{cat}/K_m)_{app}$ values for RNCs below 45 aa are set to zero, and those longer than 69 aa are set to the measured rate constants in Figs. 3.3 and 3.4. Values of $(k_{cat}/K_m)_{app}$ between 45 and 69 aa are linearly interpolated from experimental data. The translation elongation rate is set to 2 aa/s.

In vivo NME assay

DNA fragments encoding full-length FtsQ and PhoA were amplified from E. coli genomic DNA, appended with a C-terminal 3X FLAG tag, and integrated into pBAD/His C (Invitrogen) under control of the arabinose promoter (Guzman et al., 1995) via Gibson cloning. A second open reading frame (ORF) encoding thioredoxin with a C-terminal 3X FLAG tag was cloned downstream. Both the FtsQ/PhoA and thioredoxin ORFs are preceded by a Shine-Dalgarno sequence in the 5'UTR. The iMet constructs for the FtsQ variants contain the mutations M137L, M159L, M177L, M180L, M193L, and M217V. The iMet constructs for PhoA variants contain the mutations M26L, M75L, M157A, M286L, M324L, M420L, M422L, M464L, C190S, C200S, C308S, and C358S.

Plasmids were transformed into the E. coli strain CAG12184 (λ-rph-1 tolC210::Tn10 (tet)) or KPS73 (λ-rph-1 *tolC*210::Tn10 (tet) Δ*fmt* ::Km) (Piatkov et al., 2015; Singer et al., 1989). Cells were grown in Luria-Bertani medium containing 0.2% glucose and 100 μg/mL ampicillin at 37 °C until OD = 0.5-0.7, washed and resuspended to OD = 0.05 in pre-induction medium (M9 medium containing 0.5% glycerol, 0.2% glucose, 100 μg/mL ampicillin and 40 μg/mL of 20 amino acids except methionine), and grown to OD = 0.5. Cells were collected, washed three times with prewarmed induction medium (M9 medium containing 0.5% glycerol and 40 μg/mL of 20 amino acids except methionine and cysteine), and resuspended with induction medium corresponding to 1/20 volume of the cell culture. Cells were induced with 0.02% arabinose at 37 °C for 30 min, labeled with 200 μCi/mL ^{35}S-Met/Cys EasyTag mix (PerkinElmer) for 10 min, and flash-frozen in liquid nitrogen. The frozen cells were thawed, spun down, and lysed in 25 μL lysis buffer (50 mM Tris-HCl, 150 mM NaCl, 2 mM DTT, 5 mM EDTA, 4% SDS, pH 8.0) containing 1X protease inhibitor at 95 °C for 10 min. The lysates were diluted with 500 μL IP buffer (50 mM Tris-HCl, 150 mM NaCl, 5 mM EDTA, 1% Triton X-100, pH 8.0), incubated at room temperature for 10 min, and centrifuged at 12,000 × g for 5 min. Clarified lysates were further diluted with 500 μL TBS (50 mM Tris-HCl, 150 mM NaCl, pH 8.0) and incubated with 10 μL Anti-FLAG M2 magnetic beads (Sigma-Aldrich) at 4 °C for 1.5 h with rotation. The beads were washed twice with IP buffer and once with TBS, and the FLAG-tagged proteins were eluted by incubating the beads with 25 μL 2X SDS sample buffer at 95 °C for 10 min. The radioactive signals

were subsequently analyzed by SDS-PAGE and autoradiography. To calculate iMet retention, the substrate/TrxA signal ratio from the iMet construct was divided by that of the corresponding 6M or 8M4C construct, and normalized to the value of FtsQ K2 or 2A8L in each experiment.

Cell fractionation

CAG12184 cells expressing the FtsQ variants were harvested and fractionated as described previously (Wang et al., 2017). In brief, cells were subject to osmotic shock and lysozyme treatment to release the periplasm, and the spheroplasts were further lysed by freeze-thaw cycles in liquid nitrogen. The lysates were centrifuged in a TLA120.1 rotor (Beckmann Coulter) at 63,000 rpm for 1 h to separate the membrane and cytoplasm. The cellular localization of the FtsQ variants was determined by Western blot of the different fractions using anti-FLAG antibody (Genscript).

Proteinase K protection assay

Spheroplasts prepared as described above were resuspended in Buffer PK (100 mM Tris-HCl, 20% sucrose, 20 mM $MgSO_4$, pH 8.0). 0.5 mg/mL of proteinase K was added into the reaction and incubated on ice for 1h with or without 1% of Triton X-100 as control. The reaction was stopped by adding 5 mM PMSF, and analyzed by Western blot using anti-FLAG antibody.

3.5. Supplementary Figures

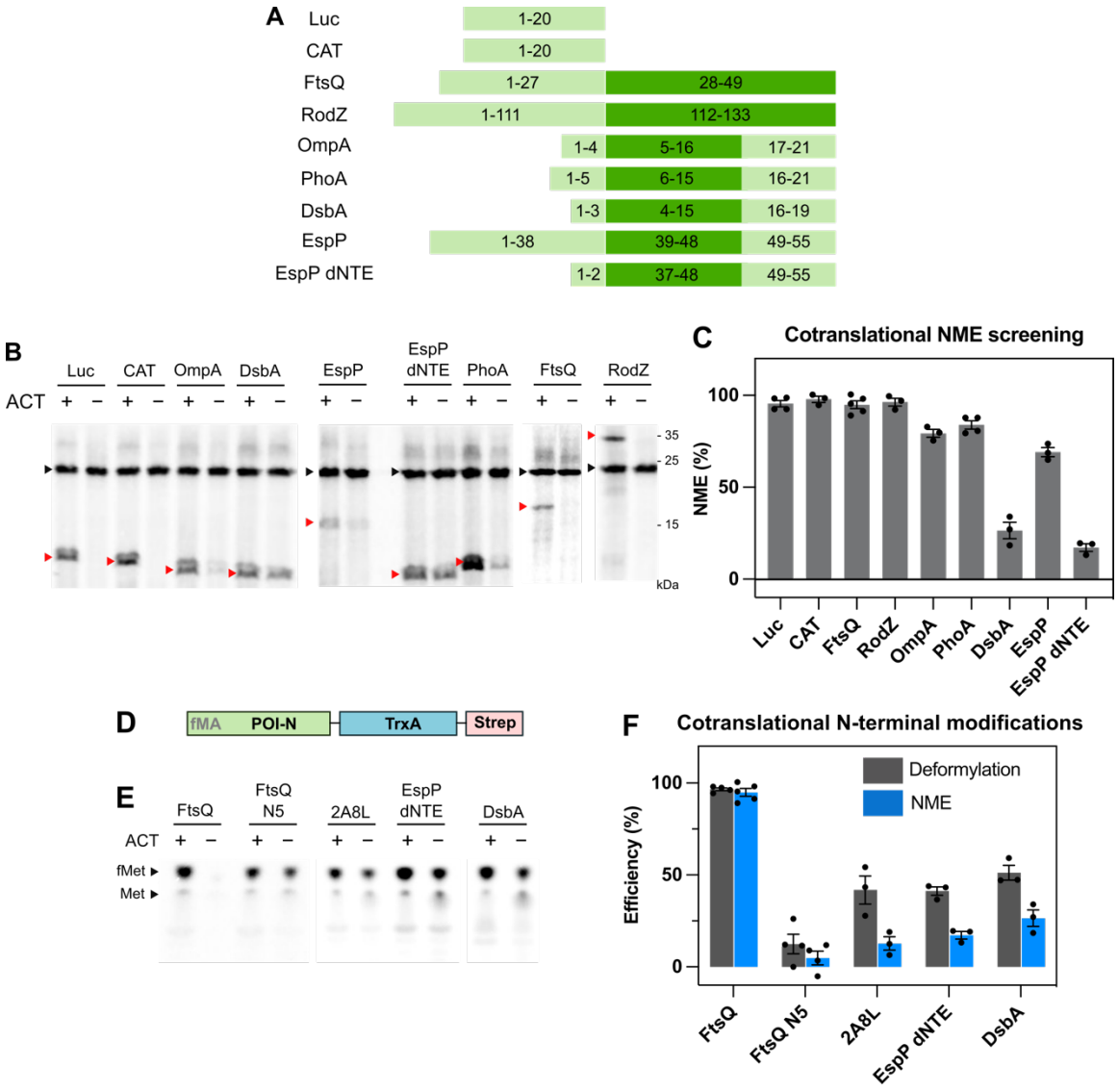

Figure S3.1. Cotranslational NME of model substrates in cell extracts.

(A) Scheme of the POI-N used to screen for molecular features that regulate NME. Hydrophobic cores of the signal sequence or TMDs are colored in dark green. **(B)** Representative SDS-PAGE autoradiography for the cotranslational NME of the model substrates in (A). Red arrows indicate the substrate of interest, and black arrows indicate

the loading control. Reactions with actinonin (ACT, 5µM) provided controls for the iMet signal from the substrates without NME. **(C)** Cotranslational NME efficiency of the indicated substrates, determined by the reduction of the iMet signal in the reactions without ACT relative to that in ACT-containing reactions. **(D)** Scheme of the model substrates used to analyze the formylation state. A Strep tag was appended C-terminally to the reporter proteins depicted in Fig. 3.1B for immunoprecipitation. **(E)** Representative TLC analysis to quantify the fMet and Met on the substrates. The substrate proteins were translated in *E. coli* S30 lysates containing ^{35}S-Met, immunoprecipitated via the Strep tag, and digested by Proteinase K. fMet and Met were separated by TLC and quantified by autoradiography. **(F)** Summary of cotranslational deformylation and NME of the indicated substrates. Deformylation was determined by the reduction of the fMet signal in the "–ACT" samples relative to the "+ACT" samples, and NME was determined as in Figs. 3.1E, H and S3.1C. Values are reported as mean ± SEM with n ≥ 3.

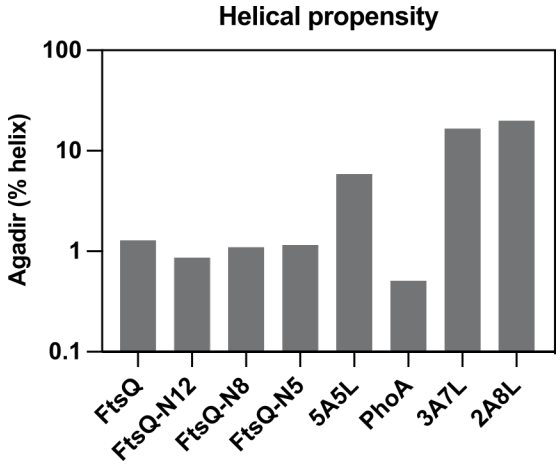

Figure S3.2. Secondary structure of the nascent chain is insufficient to explain the NME inhibition by an N-terminal membrane targeting signal.

Prediction of helical propensity using the AGADIR algorithm (Muñoz and Serrano, 1995) for the first 32 residues of FtsQ variants and first 34 residues of PhoA variants, corresponding to the exposed nascent chain sequence of the respective RNC in Fig. 3.2.

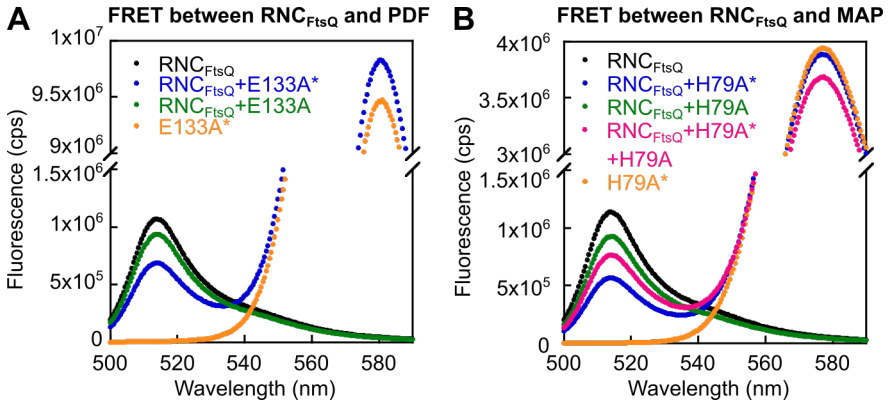

Figure S3.3. FRET assay to measure the binding between the ribosome and PDF or MAP.

(A) Fluorescence emission spectra of 10 nM BDP-labeled RNC_{FtsQ} in the absence (*black*) and presence of 4 μM TMR-labeled *(blue*, indicated by '*') or unlabeled (*green*) PDF(E133A). Incubation of BDP-RNC_{FtsQ} with TMR-PDF(E133A) induced FRET, whereas unlabeled PDF(E133A) modestly reduced the donor fluorescence intensity due to environmental sensitivity. The fluorescence emission spectrum of 4 μM TMR-PDF(E133A) is shown in *orange*. **(B)** Fluorescence emission spectra of 10 nM BDP-RNC_{FtsQ} in the absence (*black*) or presence of 1 μM TMR-labeled (*blue*) or unlabeled (*green*) MAP(H79A). The FRET signal between BDP-RNC_{FtsQ} and TMR-MAP(H79A) can be chased by unlabeled MAP(H79A) (2.5 μM, *magenta*). The fluorescence emission spectrum of 1 μM TMR-MAP(H79A) is shown in *orange*.

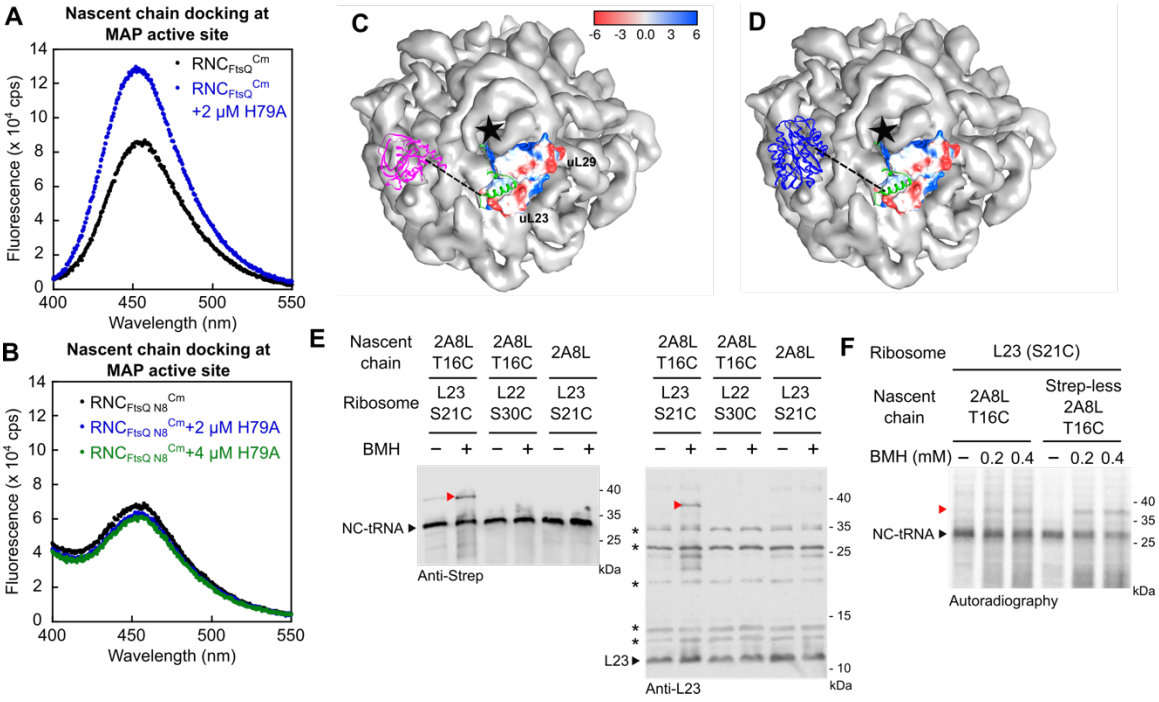

Figure S3.4. Interaction with the ribosomal surface prevents the nascent chain from accessing PDF and MAP.

(A) and (B) Fluorescence assay to report on the local environment of the nascent chain N-terminus. L-(7-hydroxycoumarin-4-yl)ethylglycine (Cm) was incorporated at the fifth position of the FtsQ (A) and FtsQ-N8 (B) nascent chains during translation. Purified RNC was incubated with the indicated amount of MAP(H79A). The enhancement in the fluorescence intensity of RNC_{FtsQ}^{Cm} upon the addition of MAP(H79A) (A) reports on docking of the nascent chain N-terminus at the MAP active site (Yang et al., 2019); this fluorescence change is not observed with $RNC_{FtsQ\ N8}^{Cm}$ in (B). **(C) and (D)** Models of PDF (C, *magenta*) or MAP (D, *blue*) bound to an RNC with an emerging TMD (*green*), viewed from the ribosome tunnel exit (star). The models were generated by overlaying the 70S structures of an RNC bearing the nascent chain of a membrane protein RodZ (PDB-6S0K) and the PDF-bound (EMD-9750) or MAP-bound (EMD-9752) ribosome using UCSF Chimera. The Coulombic surface potential of uL23 and uL29 were generated using Chimera, and colored as indicated in units of kcal·mol^{-1}·e^{-1}at 298K, where *e* denotes the charge of a proton. The distances from the N-terminus of the TMD to the active site of PDF and MAP (dashed lines) are 48 Å and 54 Å, respectively. **(E)** Representative western blot for the crosslink between RNC_{2A8L} and uL23. RNC_{2A8L} variants with or without the indicated cysteine mutations were incubated in the presence or absence of 0.4 mM

bismaleimidohexane (BMH). Crosslinked product (red arrows) was detected with anti-Strep (for nascent chain) and anti-L23 antibodies. Asterisks, non-specific bands detected by the anti-uL23 antibody. **(F)** Representative SDS-PAGE and autoradiograph of the crosslink between RNC_{2A8L} and uL23 for nascent chains with or without the N-terminal 3X Strep tag. RNC_{2A8L} was generated by *in vitro* translation in S30 extract in the presence of ^{35}S-Met, purified via sucrose gradient fractionation, incubated with indicated amount of BMH, and analyzed by autoradiography. The crosslinked product (red arrow) was independent of the presence of the Strep tag.

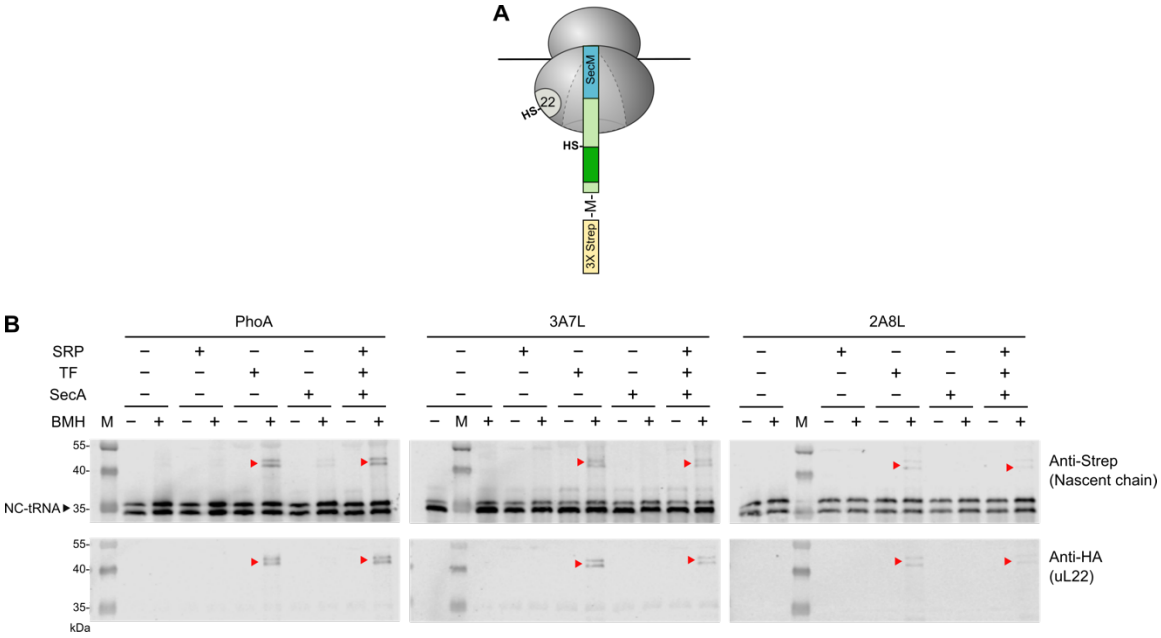

Figure S3.5. TF reorients the nascent chains.

(A) Scheme of the RNCs used to detect the proximity of the nascent chains to uL22. The mutation S30C and a C-terminal HA tag were genetically introduced into uL22, and a cysteine was placed near the signal sequence (dark green) of the model substrates, as detailed in *Methods*. **(B)** Crosslinking between the indicated nascent chains and uL22. The RNCs (500 nM) were incubated with or without 1.6 mM 1,4-bismaleimidohexane (BMH) in the absence or presence of 500 nM SRP, 10 µM TF or 1 µM SecA, and analyzed by Western blot analysis using anti-Strep (for nascent chain) and anti-HA (for uL22) antibodies. The crosslinked products between the nascent chain and uL22 (red arrows) were only detected in the presence of TF. M: molecular weight marker.

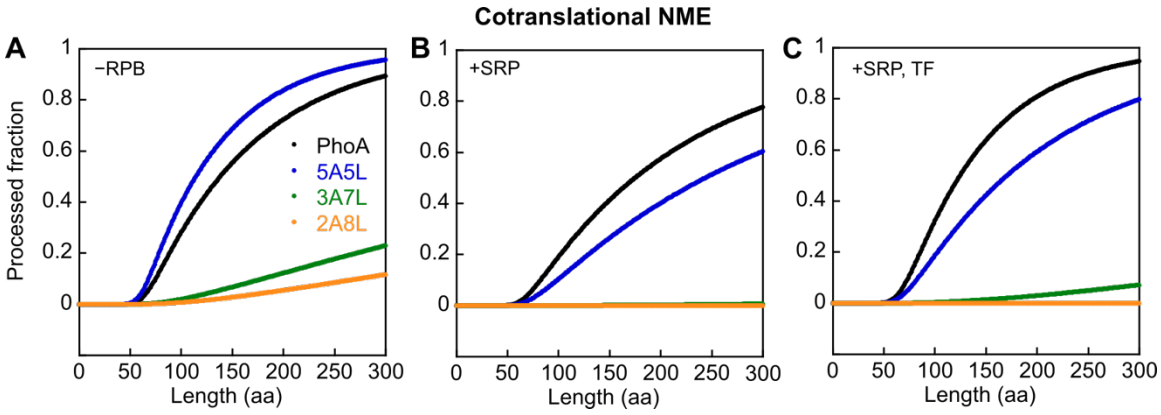

Figure S3.6. Kinetic simulation of the cotranslational NME of PhoA variants.

The cumulative fraction of the indicated model nascent chains successfully processed by both PDF and MAP during ongoing translation were calculated using the numerical integration method (Yang et al., 2019) in the absence of RPBs (A), in the presence of SRP (B), and with both SRP and TF present (C). The calculations were carried out under the following assumptions: (i) NME initiates after 45 aa of the nascent chain are translated. (ii) The k_{cat}/K_m values of the PDF and MAP reactions increase linearly to the experimentally measured values in Figs. 3.4B and D as the nascent chain elongates from 45 to 69 aa, and remain constant thereafter.

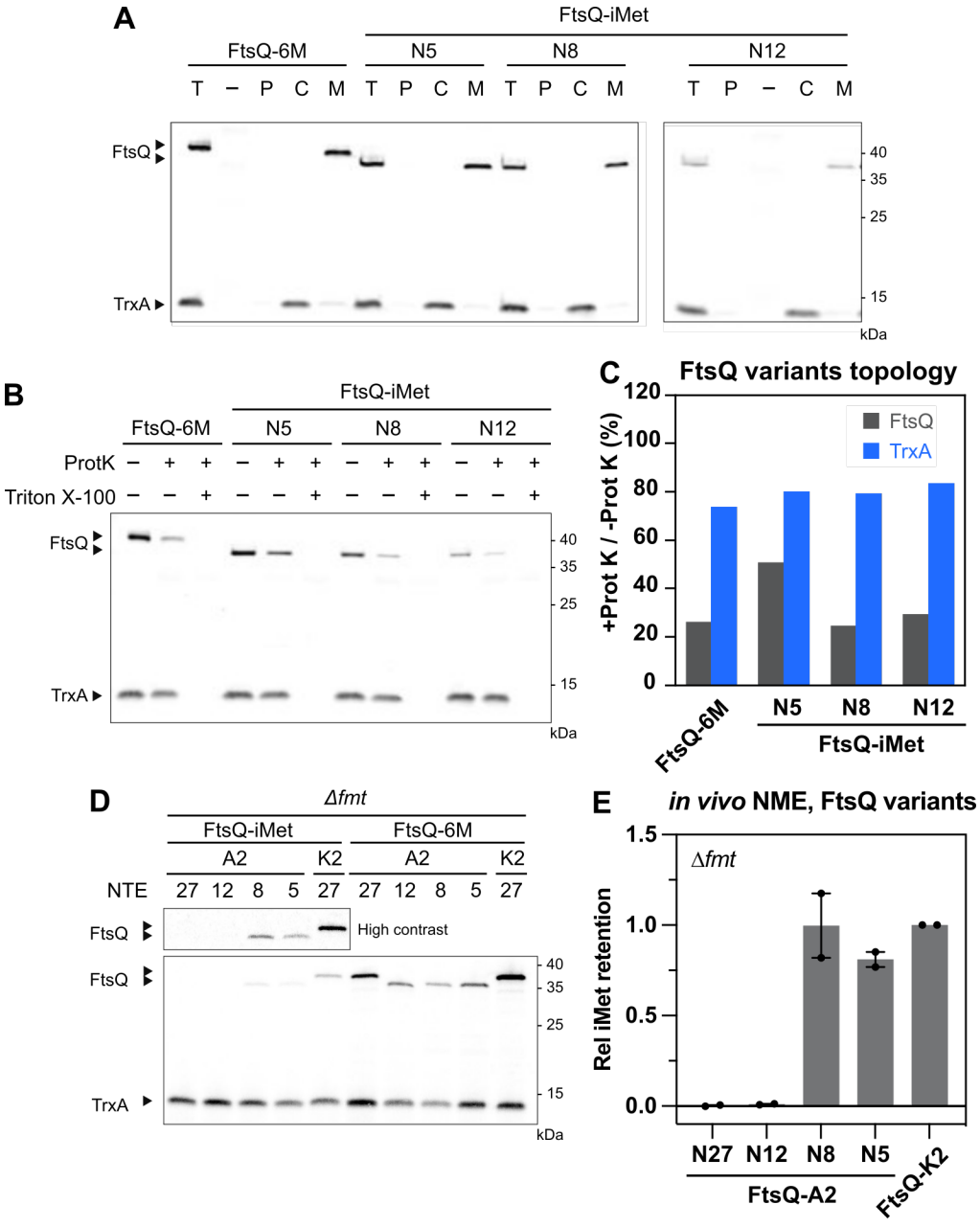

Figure S3.7. Additional data for *in vivo* NME of FtsQ variants.

(A) Cellular localization of the indicated FtsQ variants. Cells expressing the model substrates and the control protein TrxA from the constructs described in Fig. 3.5A were collected, lysed, and fractionated as described in *Methods*. The sub-cellular fractions were

analyzed by Western blotting with anti-FLAG antibody. T: total lysate; P: periplasm; C: cytoplasm; M: membrane. **(B)** Topology of the indicated FtsQ variants. Spheroplasts were prepared from cells expressing the model substrates, treated with proteinase K (ProtK) in the presence or absence of Triton X-100, and analyzed by Western blotting with anti-FLAG antibody. **(C)** Quantification of the remaining protein signals after the ProtK treatment in (B). The C-terminal FLAG tag on cytosolic TrxA was resistant to ProtK, whereas those on FtsQ-*6M*, FtsQ N12-*iMet* and FtsQ N8-*iMet* were susceptible to ProtK cleavage, consistent with the N-in-C-out topology. **(D)** *In vivo* NME of the FtsQ NTE truncation variants in the Δ*fmt* strain (KPS73), measured as described in Fig. 3.5B. **(E)** Quantification of the data in (D) and replicates. Values are normalized to FtsQ-K2 and reported as mean ± SEM, with n = 2 biological replicates.

Chapter 4

SYSTEM-WIDE ANALYSES REVEAL ESSENTIAL ROLES OF N-TERMINAL PROTEIN MODIFICATION IN BACTERIAL PHYSIOLOGY

A version of this chapter was first published as: Yang, C.-I., Zhu, Z., Jones, J., Lomenick, B., Chou, T.-F., Shan, S.-o. (2022). "System-wide analyses reveal essential roles of N-terminal protein modification in bacterial membrane integrity" In: *iScience, Accepted*.

Removal of the N-terminal formyl group on nascent proteins by peptide deformylase (PDF) is the most prevalent protein modification in bacteria that impacts over 90% of the proteome. PDF is essential and a critical target of antibiotic development; however, its role in bacterial physiology remains a long-standing question. In this work, we used time-resolved analyses of the *E. coli* translatome and proteome to investigate the consequences of PDF inhibition. Inactivation of PDF results in the rapid activation of cellular stress responses, especially those associated with protein misfolding and membrane defects, followed by a global downregulation of metabolic pathways. Functional assays reveal the rapid hyperpolarization of the plasma membrane and impaired membrane integrity upon PDF inhibition, suggesting that disruption of plasma membrane is the most immediate and

primary consequence of formyl group retention on nascent proteins. Our work resolves the physiological function of a ubiquitous N-terminal protein modification and uncovers its crucial role in maintaining the structure and function of the bacterial membrane.

4.1. Introduction

The synthesis of all bacterial proteins initiates with formylated methionine (fMet) (Adams and Capecchi, 1966; Gualerzi and Pon, 1990). After translation initiation, the formyl group on nascent polypeptides can be removed cotranslationally by peptide deformylase (Adams, 1968; Giglione et al., 2004) (PDF, encoded by *the def* gene in *E. coli*). PDF is a promiscuous enzyme with limited specificity and impacts up to 90% of the proteome, rendering deformylation the most prevalent N-terminal modification in bacteria (Adams, 1968; Bienvenut et al., 2015; Meinnel et al., 1993; Ragusa et al., 1999). Consistent with its ubiquitous activity, deformylation is an essential process in bacteria, evidenced by the lethality of *def* knockout (Mazel et al., 1994). As a result, PDF has been a prominent target for developing efficient and specific antibiotics (Giglione et al., 2000). Despite the early discovery and importance of PDF, why it is essential for bacterial survival is unknown. Methionyl-tRNA formyltransferase (MTF, encoded by the *fmt* gene), which delivers the formyl group to methionine, improves the efficiency and specificity of translation initiation but is dispensable (Antoun et al., 2006; Guillon et al., 1992; Sundari et al., 1976). Interestingly, the additional knockout of *fmt* rescues the growth of Δ*def* cells (Margolis et al.,

2000; Mazel et al., 1994). Analogously, mutations in genes involved in the generation of fMet-tRNA^{fMet} confer resistance to PDF inhibitors (Duroc et al., 2009). These observations indicate that the retention of fMet on proteins is detrimental to cells.

How PDF activity affects protein function and cellular processes remains largely unknown. Traditionally, the requirement for PDF is attributed to another essential enzyme, methionine aminopeptidase (MAP, encoded by *map* gene) (Ben-Bassat et al., 1987; Giglione et al., 2000), which catalyzes N-terminal methionine excision (NME) after the action of PDF on ~50% of bacterial proteins (Frottin et al., 2006; Hirel et al., 1989; Solbiati et al., 1999). MAP is universally conserved and plays crucial roles in multiple cellular processes in higher eukaryotic organisms, including angiogenesis, cell cycle, translation, and glutathione metabolism (Frottin et al., 2009; Fujii et al., 2018; Giglione et al., 2004; Griffith et al., 1998; Hu et al., 2006). In bacteria, MAP is required for cell viability (Chang et al., 1989), but its role in bacterial physiology is equally elusive. Multiple hypotheses have been proposed to explain the essentiality of MAP (Giglione et al., 2004, 2015; Meinnel et al., 1993). First, MAP may be involved in the metabolism of methionine, one of the most expensive amino acids for *de novo* synthesis by cells (Old et al., 1991). This model is supported by the induction of the Met biosynthesis pathway upon inhibition of *map1* gene in yeast (Dummitt et al., 2003), implicating a role of MAP in Met recycling. Whether such Met salvage pathway is essential in bacteria remains to be tested. Secondly, some essential proteins may require fMet removal to acquire activity (Meinnel et al., 1993), such as N-terminal hydrolases that

use an N-terminal Ser, Cys, or Thr as the nucleophile. However, there is limited knowledge of such NME-dependent proteins to date, few of which have been reported in *E. coli* (Brannigan et al., 1995; Kim et al., 1996; Larsen et al., 1999; Mouilleron et al., 2006; Oinonen and Rouvinen, 2000; Park et al., 2008; Yoo et al., 1997).

A different model for the role of fMet is suggested from comparison with a chemically similar modification in eukaryotes, N-terminal acetylation. Appendage of the formyl or acetyl group to the N-terminal amine reduces the net charge at the N-terminus and adds a potential interaction site to nascent proteins. N-terminal acetylation can contribute to the folding and function of multiple proteins by stabilizing secondary structures at the N-terminus (Greenfield et al., 1994; Jarvis et al., 1995; Kang et al., 2012), to protein-protein interactions by preventing the repulsion of the charged N-terminus or establishing additional contacts (Scott et al., 2011; Singer and Shaw, 2003), and to protein half-life by providing a 'degron' for the Ac/N-end rule pathway (Hwang et al., 2010; Varshavsky, 2019). Analogous roles could be envisioned for the N-terminal formyl group. Indeed, both the formyl group and the initiator Met have been proposed to control protein half-life via the bacterial fMet/N-degron pathway and Leu/N-degron pathway, respectively (Ninnis et al., 2009; Piatkov et al., 2015; Tobias et al., 1991; Varshavsky, 2019), as evidenced by fMet-dependent degradation of model substrates in *E. coli* (Piatkov et al., 2015) and by the initiator methionine-dependent recruitment of the ClpS-ClpAP protease machinery to putrescine aminotransferase (Ninnis et al., 2009). However, the native substrates of bacterial N-degron pathways are poorly

characterized (Schmidt et al., 2009). The extent to which fMet impacts the proteome via regulation of protein stability and/or other aspects of protein biogenesis and function is unclear.

In this work, we aim to fill the knowledge gap between the biochemical activity and physiological significance of PDF by studying the impact of its inhibition using system-wide analyses of the translatome and steady-state proteome. We found that acute disruption of PDF function induces protein folding defects and membrane stress responses, leading to the perturbation of cellular bioenergetics and a wide range of metabolic pathways. Importantly, time-resolved analyses of cellular responses to PDF inhibition revealed the early onset of membrane hyperpolarization and membrane-associated defects, suggesting the membrane as an immediate and primary target of fMet-retaining nascent proteins.

4.2. Results

Effect of PDF inhibition on the bacterial proteome.

We reasoned that cells can detect and respond to defects in physiologically important processes caused by the loss of PDF function. To investigate these cellular responses, we measured the changes in steady-state bacterial proteome upon PDF inhibition. To rapidly inactivate PDF, we used the antibiotic actinonin (ACT), which tightly and specifically binds the PDF active site (Chen et al., 2000; Fieulaine et al., 2011; Van Aller et al., 2005) and leads

to fMet retention on nascent proteins *in vivo* (Bienvenut et al., 2015). The *E. coli* strain CAG12184, in which the multidrug exporter *tolC* was inactivated (Bienvenut et al., 2015; Singer et al., 1989), was used to facilitate the ACT treatment. Unless otherwise specified, CAG12184 cells were grown in defined medium with a doubling time of 70-90 min and were continuously replenished with fresh medium upon entering the mid-log phase to minimize other sources of stress, such as saturation and nutrient depletion. Upon treatment with 4 μg/mL ACT (16-fold of minimal inhibition concentration (Chen et al., 2000)), cells continued to grow exponentially for ~2 generations before exhibiting a growth defect, and growth stopped after ~9 hours (Fig. 4.1A), consistent with the bacteriostatic effect of ACT and the essentiality of PDF (Chen et al., 2000; Mazel et al., 1994).

To enable quantitative assessment of the proteome, we used Stable isotope labeling by amino acids in cell culture (SILAC) coupled to Tandem mass tags (TMT), which allows sensitive and efficient analysis of multiplexed samples by LC-MS/MS (Welle et al., 2016). Cells grown in the presence of light and heavy amino acids in defined medium were treated with 4 μg/mL ACT and mock-treated, respectively. At 0, 1.5, 4.5, and 9 h after ACT treatment, an equal amount of protein from ACT-treated and control cells were mixed, protease-digested, and labeled with TMTpro16 reagents, which allowed simultaneous identification and quantification of samples from the 4 time points in 4 biological replicates using LC-MS/MS (Fig. 4.1B). In total, we quantified the time-dependent changes in the abundance ratio of 1932 proteins (Dataset1).

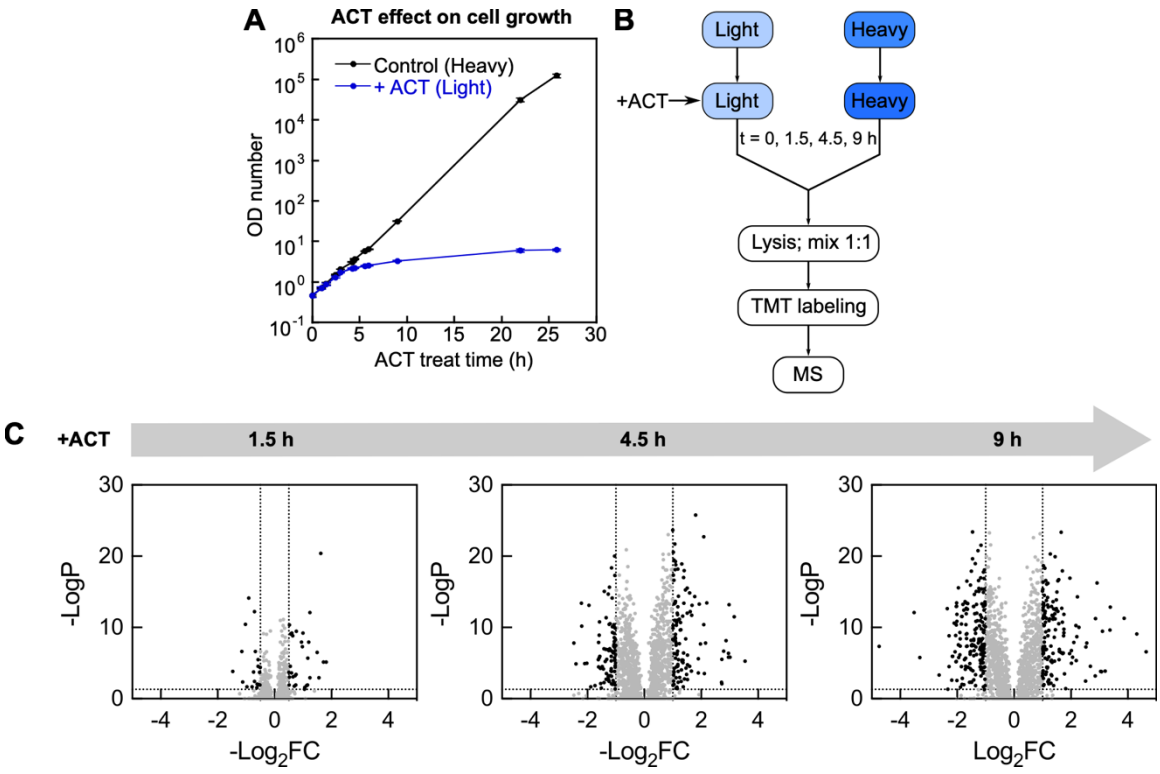

Figure 4.1. Inhibition of PDF activity leads to time-dependent changes in *E. coli* proteome.

(A) Growth curve of CAG12184 cells in SILAC medium in the absence and presence of 4 μg/mL actinonin (ACT). Cell cultures were diluted with fresh medium when they reached mid log phase (OD_{600} = 0.4-0.7). OD number is defined as the product of measured OD_{600} value and the dilution factor. Values are shown as mean ± S. D., with n = 3. Error bars are shown but may not be visible. **(B)** Overview of the SILAC-TMT procedures for proteomic analysis of PDF inhibition. Cell lysates from the light (ACT-treated) and heavy (untreated) culture collected at the indicated times were mixed at 1:1 protein ratio, digested, labeled with TMT reagents and analyzed by LC-MS/MS. **(C)** Volcano plots of the fold change (FC) in protein abundance upon ACT treatment. FC is defined as the light-to-heavy ratio of the protein level at the indicated time points relative to that at 0 h. Significantly up- and down-regulated proteins ($|\log_2 FC| \geq 0.5$ for 1.5 h and $|\log_2 FC| \geq 1$ for 4.5 h and 9 h, adjusted $p \leq 0.05$) are highlighted.

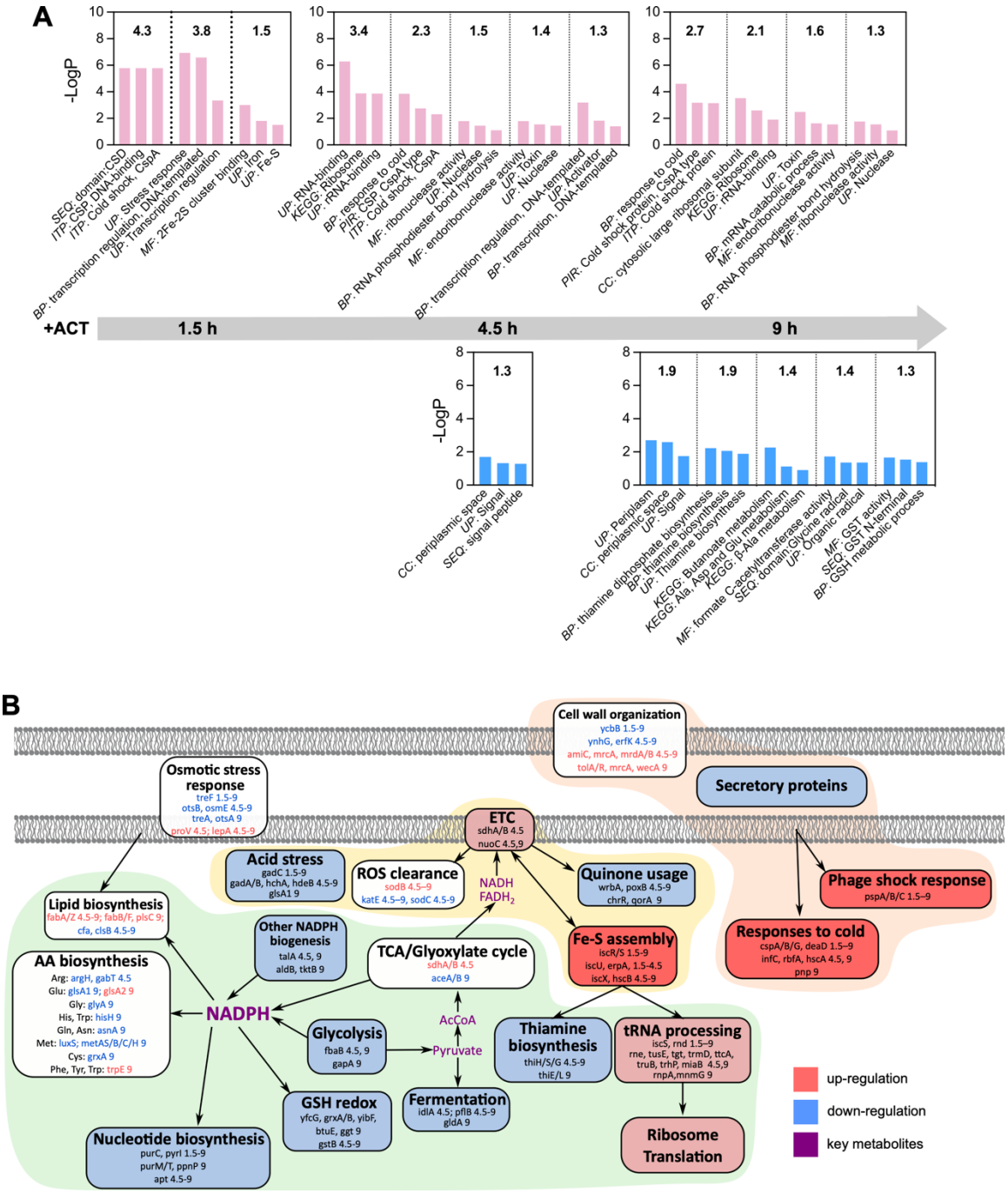

Figure 4.2. Overview of proteomic changes induced by PDF inhibition.

(A) Enrichment analysis of differentially expressed proteins upon PDF inhibition. Up- or down-regulated proteins, as defined in Fig. 4.1C, were subjected to DAVID functional annotation clustering using annotation terms from GO_BP (labeled as *BP*), GO_MF (*MF*), GO_CC (*CC*), Uniprot Keywords (*UP*), Uniprot Sequence Features (*SEQ*), Kegg Pathway (*KEGG*), InterPro (*ITP*), PIR SuperFamily (*PIR*) and SMART (*SM*). Significant clusters (Enrichment Score (indicated in bold) ≥ 1.3) are shown with the top 3 annotation terms and their P-values in each cluster. **(B)** The regulated proteins, as defined in Fig. 4.1C, are manually mapped to the cellular pathway network. Up- and down-regulated pathways are colored in red and blue, respectively, with darker and lighter colors indicating responses observed at 1.5 h and after 4.5 h, respectively. For pathways in which individual proteins are differently regulated, the individual proteins instead of the entire pathway are color indicated. The times after ACT treatment at which up- or down-regulation of the individual proteins were observed are also indicated. Pathways involved in membrane function (peach), bioenergetics (yellow), and metabolism (green) are color-shaded. See Fig. S4.3 for the list of regulated secretory proteins and Fig. S4.7 for translation-related proteins.

Differential expression analysis demonstrated increasing proteome changes over time (Fig. 4.1C and Dataset 1). Analysis of the significantly up- or down-regulated proteins using the DAVID annotation clustering algorithm (Huang et al., 2007, 2009; Jiao et al., 2012) revealed the enrichment of distinct cellular pathways at different stages after PDF inhibition (Fig. 4.2A; Dataset 2). At 1.5 h, the iron-sulfur (Fe-S) biogenesis pathway and stress responses, including the cold shock response and phage shock response pathways, were enriched in the up-regulated proteins. At 4.5 h, when growth defects begin to manifest in ACT-treated cells, translation and transcription-related proteins were up-regulated, along with the down-regulation of secretory proteins. Late responses to ACT treatment observed at 9 h included the down-regulation of metabolic pathways for thiamine, amino acids, and glutathione (Fig. 4.2A). In addition, proteins involved in multiple metabolic pathways, including respiration and nucleotide/lipid biosynthesis, were differentially expressed

(Dataset 2 and Fig. 4.2B). The regulated proteins were mapped to a manually curated pathway network, allowing us to assess the spatial, temporal, and biochemical connections between the different responses (Fig. 4.2B).

Effect of PDF inhibition on the bacterial translatome.

The observed steady-state proteome responses to PDF inhibition could be due to changes in protein synthesis and/or degradation. To distinguish between these possibilities and to complement the proteomic analysis, we used ribosome profiling (Ingolia et al., 2012) to investigate the system-wide perturbation of the translatome, which includes changes at the transcriptional and translational level. To this end, ribosome-protected mRNA footprints were isolated from mock-treated cells or cells after 0.25, 0.5, and 1.5 h of ACT treatment and subjected to deep sequencing. Gene-wise expression level was determined by the sum of normalized reads (RPM) at each codon across the transcript. From three consistent biological replicates, we quantified the time-dependent translational profile of 2405 genes (Fig. S4.1A and Dataset 3).

Differential expression analysis of the translatome data revealed significant changes in protein synthesis as early as 0.25 h after PDF inhibition, with 37 and 27 genes up- and down-regulated by more than 2-fold, respectively, and the changes became more pronounced after 1.5 h (Dataset 3 and Fig. 4.3A). The changes in the translatome correlated well with the steady-state proteome changes after 1.5 h of ACT treatment, suggesting that the observed

perturbation in the proteome arises largely from regulations of protein synthesis instead of degradation (Fig. S4.1B). DAVID clustering analysis on the genes differentially expressed by more than twofold ($p < 0.05$) revealed the enrichment in several pathways observed in the proteomic analysis, including the up-regulation of various membrane proteins and the translation machinery and the down-regulation of secretory proteins and glutathione metabolism at 1.5 h (Dataset 4 and Fig. 4.3B). Enrichment of multiple metabolic pathways was observed in the down-regulated translatome, including the TCA cycle, glycolysis, and the biosynthesis of nucleobases and amino acids (Dataset 4 and Fig. 4.3B). Notably, an up-regulation of the heat shock response was observed at 0.25 h of ACT treatment, indicating an immediate response to PDF inhibition (Dataset 4 and Fig. 4.3B). Compared to the proteomic data, the ribosome profiling results detected earlier and more prominent changes in gene expression in diverse cellular pathways (Fig. 4.3C). This may reflect the higher sensitivity of the ribosome profiling technique and suggests the presence of rapid cellular adaptive responses to PDF inhibition before changes in steady-state protein abundance are detected (Figs. 4.5–4.6, S4.3, and S4.6-S4.8 below).

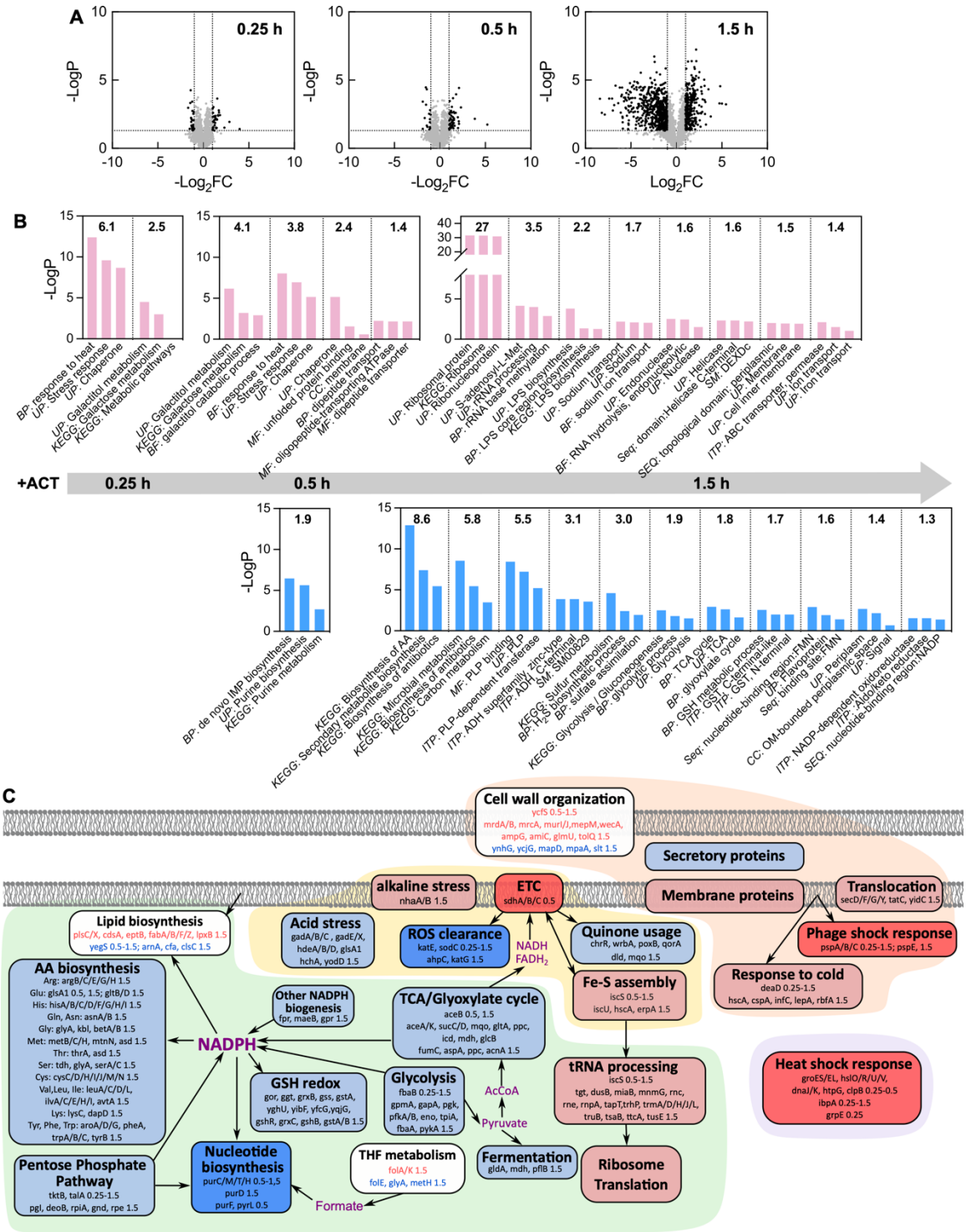
A
0.25 h
0.5 h
1.5 h
-LogP
-Log2FC
Log2FC
B
-LogP
+ACT
0.25 h
0.5 h
1.5 h
C
Cell wall organization
ycfS 0.5-1.5
mrdA/B, mrcA, murI/J,mepM,wecA,
ampG, amiC, glmU, tolQ 1.5
ynhG, ycjG, mapD, mpaA, slt 1.5
Secretory proteins
alkaline stress
nhaA/B 1.5
ETC
sdhA/B/C 0.5
Membrane proteins
Translocation
secD/F/G/Y, tatC, yidC 1.5
Lipid biosynthesis
plsC/X, cdsA, eptB, fabA/B/F/Z, lpxB 1.5
yegS 0.5-1.5; arnA, cfa, clsC 1.5
Acid stress
gadA/B/C , gadE/X,
hdeA/B/D, glsA1
hchA, yodD 1.5
ROS clearance
katE, sodC 0.25-1.5
ahpC, katG 1.5
NADH
FADH2
Quinone usage
chrR, wrbA, poxB, qorA
dld, mqo 1.5
Phage shock response
pspA/B/C 0.25-1.5; pspE, 1.5
AA biosynthesis
Arg: argB/C/E/G/H 1.5
Glu: glsA1 0.5, 1.5; gltB/D 1.5
His: hisA/B/C/D/F/G/H/I 1.5
Gln, Asn: asnA/B 1.5
Gly: glyA, kbl, betA/B 1.5
Met: metB/C/H, mtnN, asd 1.5
Thr: thrA, asd 1.5
Ser: tdh, glyA, serA/C 1.5
Cys: cysC/D/H/I/J/M/N 1.5
Val,Leu, Ile: leuA/C/D/L,
ilvA/C/E/H/I, avtA 1.5
Lys: lysC, dapD 1.5
Tyr, Phe, Trp: aroA/D/G, pheA,
trpA/B/C, tyrB 1.5
Other NADPH biogenesis
fpr, maeB, gpr 1.5
TCA/Glyoxylate cycle
aceB 0.5, 1.5
aceA/K, sucC/D, mqo, gltA, ppc,
icd, mdh, glcB
fumC, aspA, ppc, acnA 1.5
Fe-S assembly
iscS 0.5-1.5
iscU, hscA, erpA 1.5
Response to cold
deaD 0.25-1.5
hscA, cspA, infC, lepA, rbfA 1.5
NADPH
GSH redox
gor, ggt, grxB, gss, gstA,
yghU, yibF, yfcG,yqjG,
gshR, grxC, gshB, gstA/B 1.5
Glycolysis
fbaB 0.25-1.5
gpmA, gapA, pgk,
pfkA/B, eno, tpiA,
fbaA, pykA 1.5
AcCoA
Pyruvate
tRNA processing
iscS 0.5-1.5
tgt, dusB, miaB, mnmG, rnc,
rne, rnpA, tapT,trhP, trmA/D/H/J/L,
truB, tsaB, ttcA, tusE 1.5
Heat shock response
groES/EL, hslO/R/U/V,
dnaJ/K, htpG, clpB 0.25-0.5
ibpA 0.25-1.5
grpE 0.25
Pentose Phosphate Pathway
tktB, talA 0.25-1.5
pgl, deoB, rpiA, gnd, rpe 1.5
Nucleotide biosynthesis
purC/M/T/H 0.5-1,5
purD 1.5
purF, pyrI 0.5
THF metabolism
folA/K 1.5
folE, glyA, metH 1.5
Formate
Fermentation
gldA, mdh, pflB 1.5
Ribosome Translation

Figure 4.3. Effect of PDF inhibition on bacterial gene translation.

(A) Volcano plots of the fold change (FC) in translation level upon ACT treatment, determined by ribosome profiling. The thresholds for up- or down-regulated genes ($log_2FC \geq 1$ or ≤ -1, $p < 0.05$) are indicated. **(B)** Enrichment analysis of differentially translated proteins upon PDF inhibition. Up- or down-regulated genes were subjected to DAVID functional annotation clustering. Annotation categories are abbreviated as described in Fig. 4.2B. Significant clusters (Enrichment Score ≥ 1.3) are shown with the top 3 annotation terms and their P-values in each cluster. **(C)** The regulated genes, as defined in (A), are manually mapped to the cellular pathway network. Up- and down-regulated pathways are colored in red and blue, respectively, with darker or lighter colors indicating responses observed at 0.25-0.5 h or 1.5 h. For pathways in which individual genes are differently regulated, the individual genes instead of the entire pathway are color indicated. The times after ACT treatment at which up- or down-regulation were observed are indicated for each gene. Pathways involved in protein folding (purple), membrane function (peach), bioenergetics (yellow), and metabolism (green) are color-shaded. See Fig. S4.3 for the list of regulated membrane and secretory proteins and Fig. S4.7 for translation-related proteins.

Collectively, both the proteome and translatome analyses reveal extensive ACT-induced perturbations in diverse cellular pathways, consistent with the ubiquitous action of PDF across the proteome. Mapping the proteome and translatome perturbations to the network of biochemical pathways suggest that PDF inhibition led to changes in the expression of genes involved in several related cellular processes: protein folding, structure and function of the cellular membrane, bioenergetics at the membrane, and redox-dependent metabolic pathways (Figs. 4.2B and 4.3C). These changes are described and biochemically tested in the following sections.

Retention of fMet induces protein misfolding.

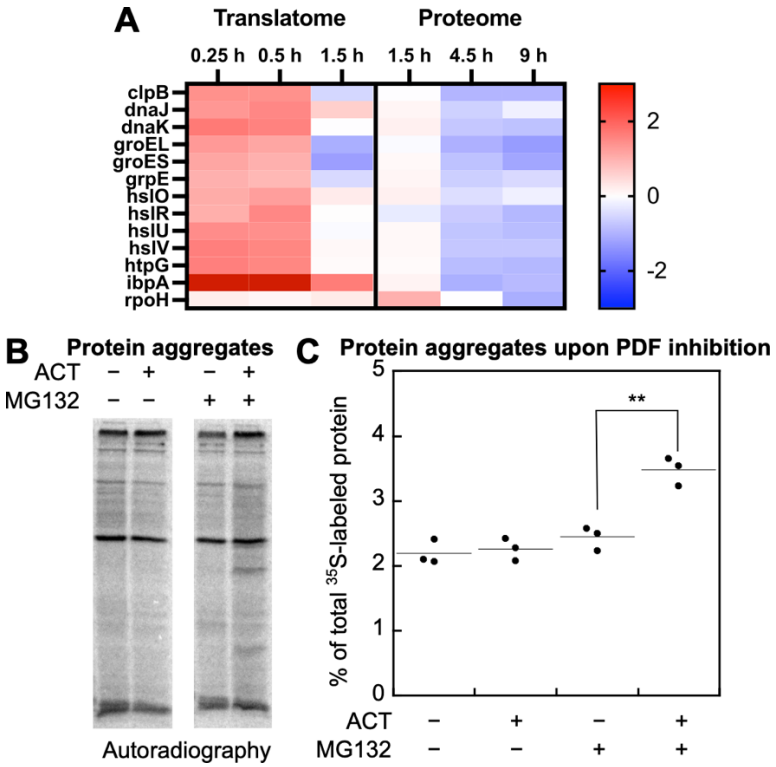

Figure 4.4. PDF inhibition induced protein folding stress.

(A) Time-dependent changes (log_2FC) in the translation (left) and steady-state protein level (right) of heat shock response genes upon PDF inhibition. **(B)** Representative autoradiographs of the analysis of nascent protein aggregates. Where indicated, cells were treated with ACT (4 μg/mL) and/or MG132 (20 μM) in the presence of ^{35}S-methionine/cysteine for 30 min. Detergent-insoluble protein aggregates were isolated and analyzed by autoradiography. The original gel image including the total and different fractions of the nascent proteins are shown in Fig. S4.2. **(C)** Quantification of ^{35}S-labeled protein aggregates isolated from cells treated with the indicated compounds. Data were analyzed by autoradiography and are shown as mean with the values from 3 biological replicates displayed. **: $p < 0.01$.

One of the earliest stress responses to PDF inhibition is the increased translation of multiple heat shock response proteins, including the Hsp70 chaperone system

DNAK/J/GrpE, the Hsp90 chaperone HtpG, the small heat shock protein IbpA, the chaperonin GroEL-GroES, the disaggregase ClpB, and the proteases HslU/V and Lon (Figs. 4.3B, 4.3C and 4.4A). The synthesis of these chaperones and quality control machineries increased more than 2-fold after 15 min of ACT treatment, followed by a decline in their translation and in steady-state protein level over time, strongly suggesting an immediate and transient protein folding stress upon PDF inhibition. To test this model, we pulse labeled the proteins synthesized after ACT treatment for 0.5 h using ^{35}S-methionine and cysteine and isolated protein aggregates using adaptations of an established protocol (Friedrich et al., 2021; Tomoyasu et al., 2001). We observed an ~40% increase in detergent-insoluble protein aggregates in cells treated with both ACT and MG132, a proteasome and HslU/V inhibitor (Park et al., 2008; Rohrwild et al., 1996) (Figs. 4.4B, C, and S4.2). Thus, failure to remove the N-terminal formyl group could disrupt the folding of newly synthesized proteins, which are subjected to quality control by the HslU/V protease complex.

PDF inhibition causes defects at the bacterial membrane

Genes involved in stress responses associated with the bacterial membrane comprise a major cluster of ACT-induced changes (Figs. 4.2B and 4.3C, shaded in peach). Up-regulation of major components in the phage shock (Psp) and cold shock (Csp) response pathways, including PspA/B/C and CspA/B/G, are among the most pronounced proteome responses to PDF inhibition (Dataset 1). In addition, the translation of PspA/B/C increased

by more than 2-fold as early as 0.25 h (Figs. 4.3C and 4.5A). The Psp system is usually induced upon exposure to membrane stress to protect the integrity of the bacterial inner membrane, and the induction of cold shock proteins often accompanies a change in membrane fluidity (Barria et al., 2013; Flores-Kim and Darwin, 2016; Jovanovic et al.). The upregulation of these stress pathways strongly suggests immediate membrane defects upon PDF inhibition.

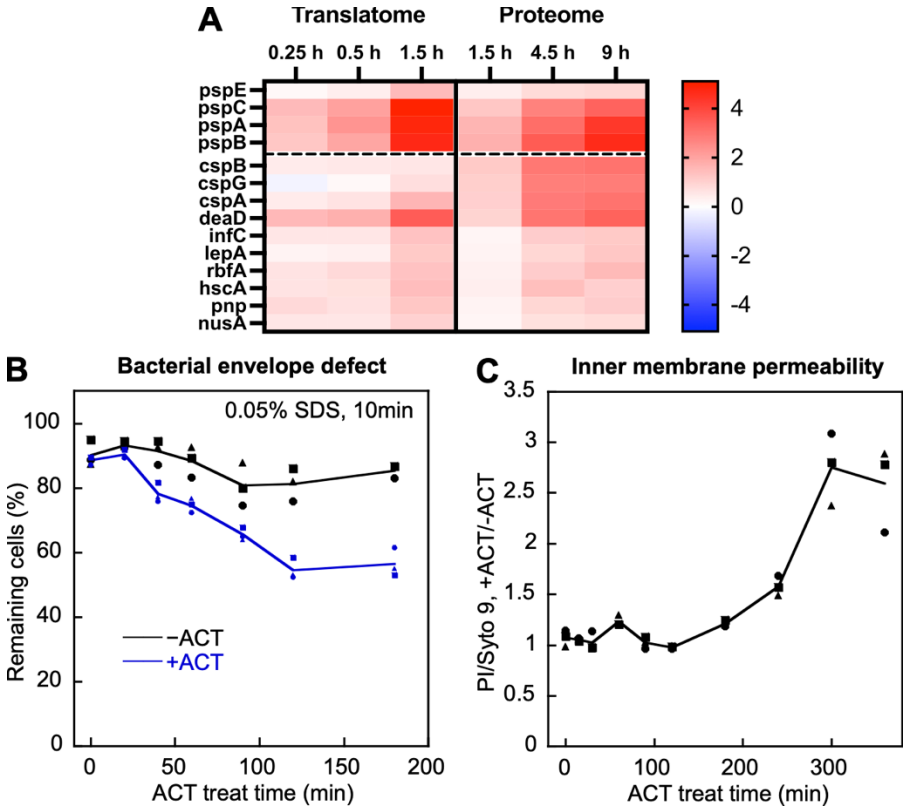

Figure 4.5. PDF inhibition leads to bacterial membrane defect.

(A) Time-dependent changes (log_2FC) in the expression (left) and steady-state protein (right) level of indicated phage shock genes (top) and genes related to cold response

(bottom) upon PDF inhibition. **(B)** SDS susceptibility of cells upon PDF inhibition. After ACT addition, CAG12184 cells collected at the indicated times were mixed with 0.05% SDS. The cell density was determined by OD_{600} after 10 min and normalized to that before SDS addition. The data for 3 biological replicates are shown, and the line represents the mean. **(C)** The effect of PDF inhibition on the inner membrane integrity of CAG12184 cells. The membrane permeability was measured by the ratio of fluorescence intensity of propidium iodide (PI) to the membrane permeable dye Syto 9 and normalized to that of the cells without ACT treatment. The values for 3 biological replicates are shown, and the line represents the mean.

After the onset of membrane stress responses, at 1.5 h in the translatome and 4.5–9 h in the steady-state proteome, we observed a decrease in the translation and abundance of multiple secretory proteins and an increase in the translation of membrane proteins, including components of all the major protein translocation machineries such as SecYEG/DF, YidC, and Tat (Fig. S4.3), suggesting compromised protein translocation at the bacterial inner membrane. Multiple proteins involved in cell wall generation and maintenance were also dysregulated (Figs. 4.2B and 4.3C). Similar to cells deficient in the membrane protein targeting factor, signal recognition particle (Zhang et al., 2012), cells subjected to prolonged PDF inhibition exhibited elongated and heterogeneous morphology (Figs. S4.4A-C).

To directly test the effect of PDF inhibition on the bacterial membrane envelope, we measured the susceptibility of cells to sodium dodecyl sulfate (SDS), which induces lysis more readily when the cell envelope is compromised (Singh et al., 2021; Zhang et al., 2012). Cells exhibited increased sensitivity to SDS after 40 min of ACT treatment. This effect was exacerbated after 120 min of treatment, at which 50% of ACT-treated cells were lysed by

0.05% SDS within 10 min (Figs. 4.5B and S4.4D-G). In addition, we measured the integrity of the inner membrane using a fluorescent probe, propidium iodide (PI), which penetrates permeabilized membrane to bind the DNA (Stocks, 2004; Sträuber and Müller, 2010). We observed a significant increase in PI fluorescence after 5 h of ACT treatment, indicative of significant membrane rupture (Fig. 4.5C). Cells grown in rich medium exhibited similar albeit earlier membrane defects, potentially due to more active protein translation. Under the same growth condition, the membrane of cells lacking formyltransferase (Δ*fmt* (Piatkov et al., 2015)), which bypasses deformylation, remained intact even after 6 h of ACT treatment (Fig. S4.4H). These observations rule out off-target effects of ACT and suggest a direct role of formylated nascent proteins in disrupting bacterial membrane integrity.

PDF inhibition disturbs bioenergetics at the membrane.

In addition to the membrane-associated stress responses, iron-sulfur cluster (Isc) biosynthesis factors and chaperones (IscU/R/S/X and HscA/B), and the Fe-S cluster carrier ErpA are enriched in the earliest up-regulated proteome at 1.5 h (Figs. 4.2 and 4.6A). Increased translation of components of these pathways was observed beginning at 0.5 h (Figs. 4.3C and 4.6A). In addition, we observed an increase in the translation and steady-state level of multiple Fe-S cluster-binding enzymes, including several enzymes involved in tRNA processing (TtcA and MiaB) and the subunit of electron transport chain (ETC)

complex II (SdhB) (Figs. 4.2B, 4.3C, and 4.6A), consistent with the essential role of the Isc pathway in the maturation of Fe-S enzymes (Ezraty et al., 2013).

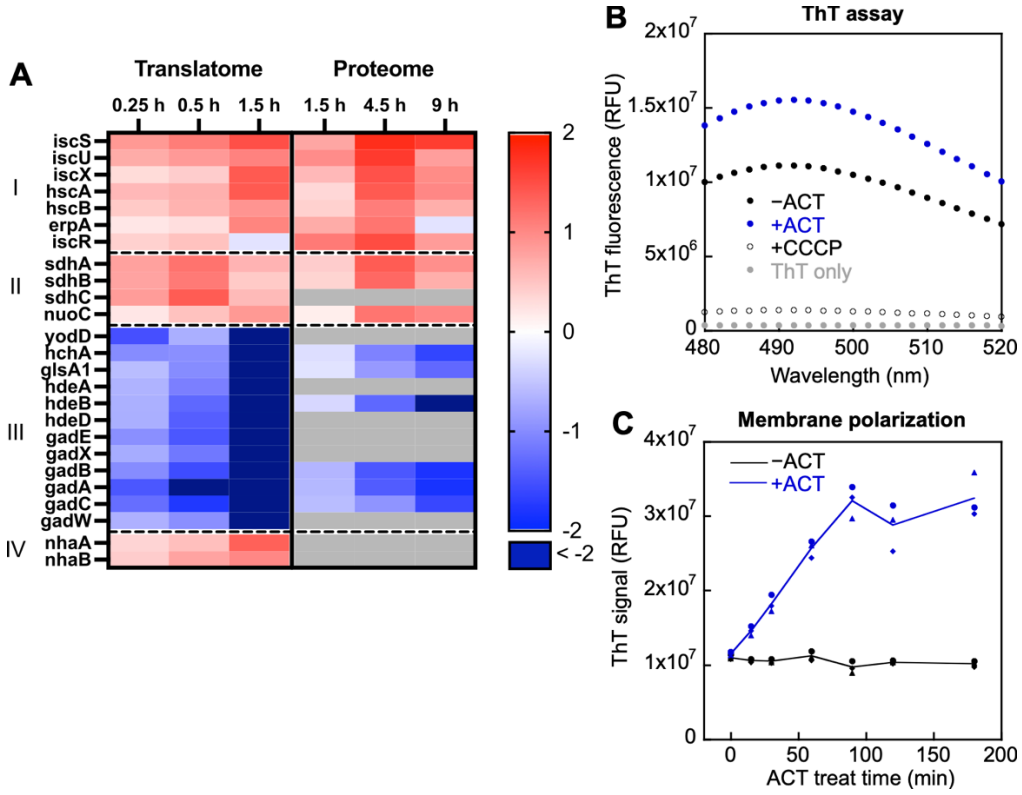

Figure 4.6. Inhibition of PDF induces membrane hyperpolarization.

(A) Time-dependent changes (log_2FC) in the translation (left) and steady-state protein level (right) of the regulated genes in the Fe-S cluster biogenesis pathway (I), the electron transfer complexes (II), the acid response pathway (III), and the alkaline response pathway (IV) upon PDF inhibition. **(B)** Thioflavin T (ThT) fluorescence spectra measured with CAG12184 cells before (solid black) and after 15 min of treatment with 4 µg/mL ACT (solid blue), and after an additional 5 min of 5 µM CCCP treatment (open black). The ThT spectrum without cells is shown in gray. **(C)** Membrane potential of CAG12184 cells mock-treated (black) and treated with ACT (blue), measured by the fluorescence intensity of ThT. The values for 3 replicates are shown, and the line represents the mean.

The translation of other subunits of ETC complex II (SdhA, SdhC) and the steady state level of the ETC complex I subunit NuoC were also up-regulated (Figs. 4.2B, 4.3C, and 4.6A), suggesting disturbance in oxidative phosphorylation that couples redox energy to the generation of proton motive force (PMF). Related to these observations, a significant down-regulation of acid stress response was detected at 1.5 h of ACT treatment, including components of the glutamate-dependent acid resistance (AR2) system (GadA/B/C/E/X), which consumes intracellular protons via decarboxylation of glutamate (Foster, 2004; Krulwich et al., 2011) (Figs. 4.2B , 4.3C, and 4.6A, cluster III). In contrast, the translation of NhaA and NhaB, which export Na^+ in exchange for protons during alkaline stress (Padan et al., 2005), was up-regulated at 1.5 h (Figs. 4.3C and 4.6A). These observations suggest that cells respond to PDF inhibition by increasing the proton concentration at the cytosolic side of the plasma membrane. Several genes involved in the response to reactive oxygen species (ROS) and the consumption of quinone were also differentially regulated in the translatome and proteome data (Figs. 4.2B and 4.3C). Together, these observations suggest that PDF inhibition leads to abnormal bioenergetics at the plasma membrane.

To directly test this hypothesis, we used a Nernstian voltage indicator, thioflavin T (ThT), to measure the membrane potential ($\Delta\psi$) component of PMF upon PDF inhibition (Prindle et al., 2015). Cationic ThT molecules permeate the cell and accumulate on the cytoplasmic side of the membrane due to the negative membrane potential, giving rise to increased fluorescence signal (Fig. 4.6B) (Prindle et al., 2015). Treatment with carbonyl

cyanide *m*-chlorophenyl hydrazone (CCCP), a protonophore that depolarizes the cell, abolished the fluorescence (Fig. 4.6B). We observed a drastic increase in ThT fluorescence upon PDF inhibition, which was detected as early as 15 min after ACT treatment and continued to rise until 90 min when it reached the maximum detectable value (Fig. 4.6C), indicating extensive membrane hyperpolarization (Figs. 4.6B and C). In contrast, the membrane potential of Δ*fmt* cells remained invariant (Fig. S4.5A). Independent measurements with another established membrane potential indicator $DiOC_2(3)$, which exhibited a red shift in emission wavelength (Hudson et al., 2020; Novo et al., 1999), confirmed the ACT-induced hyperpolarization detected by ThT (Fig. S4.5B). Notably, the addition of CCCP abolished the ACT-induced ThT signal, excluding other factors that could enhance ThT fluorescence, such as protein aggregation (Fig. S4.5C). Finally, the additional presence of a translation inhibitor, chloramphenicol, rescued the ACT-induced membrane hyperpolarization, suggesting that the observed changes in membrane potential are directly caused by the retention of the formyl group in newly synthesized proteins (Fig. S4.5D). Collectively, these observations demonstrate that the accumulation of fMet-retaining nascent proteins induces rapid membrane hyperpolarization and disruptions of membrane bioenergetics.

PDF inhibition disrupts metabolism and redox homeostasis.

Multiple metabolic pathways were also dysregulated following PDF inhibition. At 0.5 h after ACT treatment, we observed reduced translation of genes involved in the *de novo* biosynthesis of pyrimidine and purine (Figs. 4.3C and S4.6A). This could be partially attributed to the inhibition of NME on amidophosphoribosyl transferase (purF), which requires unmasking of Cys2 to catalyze a committed step in *de novo* purine synthesis (Kim et al., 1996). Alternatively or in addition, this rapid response could originate from the depletion of formate following PDF inhibition, as formate and tetrahydrofolate (THF) derivatives are precursors of purines and pyrimidines (Baxter and Scott, 1984; Moffatt and Ashihara, 2002; Oizel et al., 2020). Consistent with the essential roles of formate in one-carbon metabolism (Leonhartsberger et al., 2002), we also observed changes in the translation of the genes involved in THF conversion, including glyA, metH, folA, folK, and folE (Figs. 4.3C and S4.6B).

The majority of ribosomal proteins were up-regulated in the translatome after 1.5 h of ACT treatment, and their steady-state abundances started to accumulate after 4.5 h (Fig. S4.7A). This response is likely related to the inability of several ribosomal proteins to undergo N-terminal acetylation (Cumberlidge and Isono, 1979; Jones and O'Connor, 2011; Tanka et al., 1989; Yoshikawa et al., 1987), which confer interactions to stabilize ribosome structure and modulate ribosome assembly (Clatterbuck Soper et al., 2013; Gordiyenko et al., 2008). Accordingly, multiple genes related to translation, ribosome biogenesis, and

rRNA modification were also up-regulated, potentially as cellular responses to rescue ribosome assembly and translation activity (Fig. S4.7B).

After 1.5 h of ACT treatment, we began to observe reduced synthesis of genes involved in energy generation pathways, such as glycolysis and the TCA cycle, and in the biosynthesis pathways for NADPH, the cellular currency for reducing power (Fig. S4.8A). Translation of several amino acid biosynthetic pathways, which heavily depend on NADPH (Ju et al., 2020; Spaans et al., 2015), and the glutathione metabolism pathway, which plays key roles in maintaining the proper redox state of the cell (Masip et al., 2006), were down-regulated after 1.5 hr of ACT treatment (Fig. S4.8B). Accordingly, the steady-state level of multiple proteins in these pathways decreased after 4.5 – 9 h (Fig. S4.8B).

To test the role of PDF in cellular redox homeostasis, we used an established enzymatic assay to measure the level of the different forms of nicotinamide adenine dinucleotides, which are critical electron carriers in metabolic reactions (Kern et al., 2014). We observed an increase in the NAD^+ level and a depletion of NADH and NADPH after 9 h of ACT treatment, indicating an imbalance in redox homeostasis upon PDF inhibition (Fig. S4.8C).

4.3. Discussion

As the earliest covalent modifications encountered by nascent proteins, the pivotal roles of deformylation and NME are reflected by the loss of cell viability upon the depletion or inhibition of PDF and MAP. However, why these modifications are essential for bacterial survival (Mazel et al., 1994) has been a long-standing question. In this work, we combined unbiased proteome and translatome analyses to investigate the roles of N-terminal protein modifications in bacterial physiology. Our results revealed different stages of cellular responses to PDF inhibition (Fig. 4.7A). Within 15-30 min of PDF inactivation (Phase I), cells exhibited rapid responses to protein misfolding and membrane stresses. Membrane hyperpolarization was detected at this early stage, along with the differential translation of proteins in the ETC, which are reflected in changes in their protein levels after 1.5 h. In Phase II (1.5 h), the defect in membrane potential intensified and was accompanied by significant remodeling of the membrane proteome, including the increased synthesis of membrane proteins and reduced expression of secretory proteins. Up-regulation of the Fe-S cluster biogenesis pathway and the translation machinery also occurs at this stage, along with reduced translation of proteins involved in multiple metabolic pathways. In Phase III (after 3 h of ACT treatment), cell growth defects are observed. The changes in the translatome during Phase II manifest in steady-state proteome changes after 4.5 h, followed by considerable membrane rupture and NAD(P)H depletion. These time-resolved analyses

provide insights into the direct and indirect roles of PDF in regulating various biological pathways.

Multiple models could link the biochemical activity of PDF to the physiological impact of its inhibition. It has been proposed that proper NME is required to unmask the second residue on N-terminal nucleophile hydrolases and other enzymes (Meinnel et al., 1993). In addition, the retention of fMet may perturb the folding trajectory of nascent proteins, as the chemically similar N-terminal acetylation plays pivotal roles in controlling protein folding, targeting, and complex assembly (Aksnes et al., 2019; Forte et al., 2011; Friedrich et al., 2021; Kang et al., 2012). Our data here support the role of proper N-terminal modification in protein biogenesis. PDF inhibition leads to the formation of nascent protein aggregates and the rapid induction of heat shock responses (Fig. 4.4). The increased translation of the membrane protein chaperone YidC and other translocation machineries also suggests defects in membrane protein folding and translocation. Notably, the different biochemical mechanisms predict distinct kinetics by which PDF inhibition impacts cell function. If fMet retention inhibits protein function, then defects in function will manifest only after the turnover of pre-existing proteins that underwent the correct NME. Alternatively, if defective protein biogenesis due to fMet retention generates toxic species that disrupt cellular functions, the defects would occur immediately after PDF inhibition. Both classes of models contribute to the cellular responses observed in our study, as discussed below.

Although an estimated 90% of the bacterial proteome is modified by PDF, our time-resolved analyses suggest that the membrane is the earliest and primary target of PDF inhibition. This is most strongly evidenced by the pronounced activation of membrane stress responses and membrane hyperpolarization observed in Phase I, the compromised membrane integrity, and the differential expression of multiple membrane and secretory proteins. The ACT-induced membrane defects require protein synthesis and are likely a direct consequence of fMet-retaining nascent proteins (Figs. S4.4H, 4.6C, S4.5A, and S4.5D). As discussed above, the rapid onset of membrane-associated defects (<15 min) suggest that they originate from the toxicity of fMet-retaining nascent proteins that impair the mechanisms involved in the maintenance of membrane structure and/or function. Misfolded and aggregated proteins could disrupt membrane structure via aberrant protein-lipid interactions, as documented for amyloidogenic protein aggregates and aminoglycosides that generate mistranslated proteins (BUSSE et al., 1992; Davis et al., 1986; Lal et al., 2007; Sciacca et al., 2012, 2021). Alternatively or in addition, fMet-retaining nascent proteins could interfere with the proper functioning of membrane proteins. For example, the rapid membrane hyperpolarization is most easily explained by the 'poisoning' of PMF-dissipating machineries such as ATP synthase, ion transporters, and protein translocation machineries, many of which are up-regulated after 1.5 h of PDF inhibition. In particular, nascent membrane proteins that retain fMet may fail to translocate and thus jam or overload the translocation machinery, in analogy to the effect of N-terminal acetylation in yeast (Forte et al., 2011), leading to extensive

membrane stress. The down-regulation of secretory proteins and up-regulation of various protein translocation machineries likely reflect cellular responses to reduce the load on protein translocation pathways while increasing the capacity of these pathways. Finally, the down-regulation of potassium channels (Kch, MscL, and MscS) and up-regulation of sodium transporters (ChaA, NhaA, and NhaB) (Dataset 3) suggest that the maintenance of selective ion gradients across the membrane is also disrupted. Regardless of the precise mechanism, the rapid onset of the membrane defects upon PDF inhibition is most consistent with models in which fMet retention generates toxic species that directly impact the structure and function of the bacterial plasma membrane.

PDF inhibition also perturbs multiple metabolic pathways in the cytoplasm. Our observations here are consistent with the results of NME inhibition in archaea and higher eukaryotes, which was also reported to dysregulate glutathione metabolism and deplete NADPH (Frottin et al., 2009, 2016). With the exception of the downregulation of the genes involved in THF, purine and pyrimidine biosynthesis, which is likely due to the role of formate as a precursor in the biosynthesis of these molecules (Baxter and Scott, 1984; Duthie et al., 2002; Moffatt and Ashihara, 2002), the dysregulation of translation, redox metabolism, and NADPH-dependent biosynthesis pathways occurred late and is likely caused by mechanisms distinct from the early-onset membrane defects. As discussed earlier, fMet retention could affect ribosome biogenesis by inhibiting the proper post-translational modifications on ribosomal proteins and impair the activity of metabolic enzymes that rely

on both PDF and MAP activity to generate key catalytic residues at the N-terminus. These effects on newly synthesized proteins manifest over time as the existing pool of proteins are replaced. However, a limited number of N-terminal nucleophilic hydrolases are known so far in *E. coli*, (Fox et al., 2014) including PurF, asparagine synthetase B (AsnB), glutamine--fructose-6-phosphate aminotransferase (GlmS), and HslV; the small number and the redundancy of many of these proteins (Humbert and Simoni, 1980) are not sufficient to explain the extensive re-programming of metabolic pathways we observed. Alternatively or in addition, as glycolysis and redox metabolism are intimately linked to oxidative phosphorylation at the membrane, the changes in these metabolic pathways may be a downstream effect of the dysfunctions of bioenergetics at the membrane.

Our data also help evaluate several previous models for the essentiality of NME. One model involves the recycling of methionine from a fraction of nascent proteins (Dummitt et al., 2003; Meinnel et al., 1993). As methionine is supplied in the growth medium and the genes involved in the methionine biosynthesis pathway are down-regulated upon PDF inhibition, increased demand for the supply of methionine is unlikely under our experimental conditions. Another potential role of fMet is to serve as a degradation signal, providing a quality control pathway for nascent proteins (Kim et al., 2018; Piatkov et al., 2015). Under our experimental conditions, however, the change in protein abundance upon PDF inhibition is largely determined by altered protein synthesis instead of degradation. The fMet-mediated

degradation is thus likely to be conditional and substrate-specific, akin to the Ac/N-degron pathway in eukaryotes (Hwang et al., 2010; Varshavsky, 2019).

We suggest the following model to explain the physiological impact of incorrect N-terminal modification in bacteria (Fig. 4.7B). The immediate molecular consequences of PDF inhibition are the depletion of formate (Step 1a) and accumulation of fMet-retaining nascent proteins (Step 1b). A temporary decrease in formate level could affect the synthesis of nucleobases and one-carbon metabolism mediated by THF derivatives. However, we speculate that this effect is local, as deformylation of nascent proteins only constitutes a fraction of the formate supply. On the other hand, nascent proteins that escape deformylation and NME immediately and profoundly impact the integrity and proper functioning of the membrane. This could occur via rapid replacement of functional proteins (Step 2a) or, more plausibly, the accumulation of misfolded protein aggregates (Step 2b), which induces protein folding stress both in the cytosol and at the membrane. Aberrant fMet-retaining proteins disrupt the structure and function of the membrane (Step 3a), including the dysregulation of PMF (Step 3b), leading to the activation of membrane stress responses as well as transcriptional/translational re-programming that adjust the demand for membrane functions, such as protein translocation and ion transport. Over time, the disruption of bioenergetics at the membrane and potential accumulation of enzymes inactivated by fMet retention leads to the down-regulation of proteins involved in redox metabolism/homeostasis and to the reduction of NADPH-dependent biosynthetic pathways (Step 4). Our work uncovers the

significance of a ubiquitous N-terminal modification in bacterial protein biogenesis and emphasizes the role of the inner membrane in translating the NME-linked protein biogenesis defects to cellular metabolism. Identification of the critical protein players and the mechanistic link between NME and membrane structure/function remain outstanding goals for future investigations.

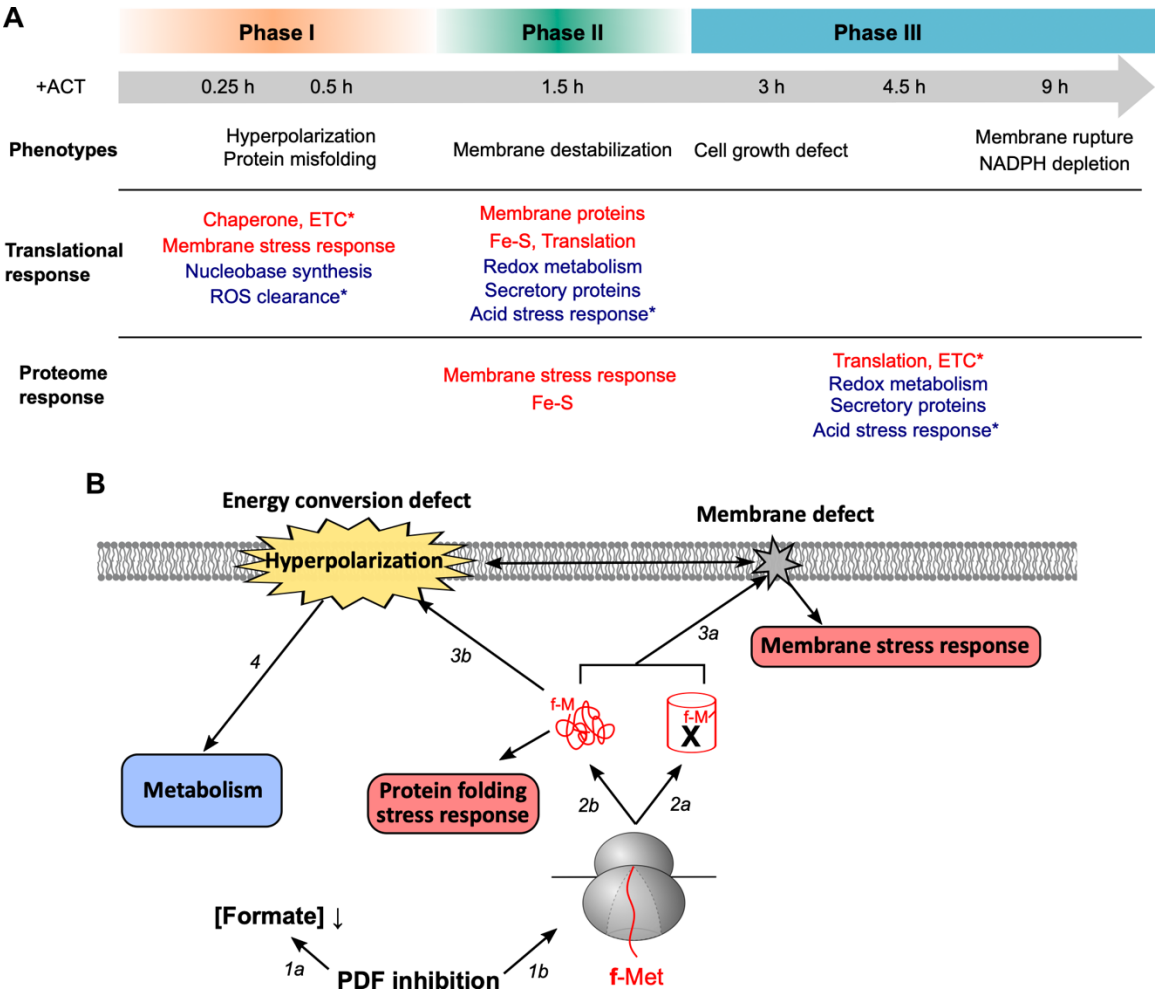

Figure 4.7. Impact of PDF inhibition on bacterial physiology.

(A) Summary of the time-dependent changes in cell physiology, gene expression and steady state proteome level induced by PDF inhibition. Up- or down-regulated pathways in translatome or proteome are colored in red or blue, respectively. With the exception of chaperone upregulation, which turns 'off' after Phase I, all the other responses persist for the remainder of the ACT treatment. Asterisk, pathways related to oxidative phosphorylation. **(B)** Model for the cellular impact of PDF inhibition, as described in the text.

4.4. Materials and Methods

SILAC-TMT

E. coli cell growth and PDF inhibition. E. coli cells from strain CAG12184 (Singer et al., 1989) were grown at 37 ˚C in SILAC medium (48 mM Na_2HPO_4, 22 mM KH_2PO_4, 8 mM NaCl, 19 mM NH_4Cl, 2 mM $MgSO_4$, 0.1 mM $CaCl_2$, 0.4% glucose, 40 μg/mL each of Ser, Thr, Val, Phe, Ile, Leu, Tyr, His, Met, Trp, Lys, and Arg) for optimal metabolic labeling of Lys and Arg isotopes (Ping et al., 2013). For SILAC experiments, two parallel cultures were grown in the presence of light or heavy Lys ($^{13}C_6$, $^{15}N_2$-*L*-lysine, Sigma) and Arg ($^{13}C_6$, $^{15}N_4$-*L*-arginine, Cambridge Isotope Lab) for >30 generations to allow ≥95% incorporation of the isotope labels. At OD_{600} = 0.4, 4 μg/mL ACT (Enzo) was added to the light culture. Cells were continuously diluted with fresh medium with or without ACT whenever the OD_{600} reached 0.6-0.8. At indicated time points, cells were harvested by centrifugation and flash-frozen in liquid nitrogen.

MS sample preparation. All of the buffers were made using LC/MS Grade water (Fisher). Cells were resuspended with MS buffer (50 mM Hepes-NaOH, pH 8.5) containing 10 M urea and 1X Halt protease inhibitor (Thermo Scientific), sonicated briefly, and centrifuged (16,600 × *g*, 5 min) at room temperature to remove cell debris. The lysate was diluted to reduce the urea concentration to 8 M, and the protein concentration was determined by Bradford assay (Bio-rad). An equal amount of total proteins from heavy and light isotope-labeled cells were mixed, reduced by 10 mM TCEP (20 min incubation at room temperature), and alkylated by 27 mM 2-chloroacetamide (15 min incubation in dark at room temperature). Lys-C (Wako Chemicals) was added to the sample at an enzyme-to-protein ratio of 1:200, and incubated at 37 ˚C for 4 h. The sample was further diluted with MS buffer to reduce the urea concentration to 2 M, and incubated overnight with trypsin (Thermo Fisher Scientific) at an enzyme-to-protein ratio of 1:100. The digested peptides were then acidified with 0.5% trifluoroacetic acid (TFA), and desalted with C18 Spin Columns (Thermo Fisher Scientific). For SILAC-TMT experiment, desalted peptides were further labeled with TMTpro 16plex reagents (Thermo Fisher Scientific). An equal amount of peptides with different TMT labels were pooled, desalted, and separated into 8 fractions using High pH Reversed-Phase Peptide Fractionation Kit (Thermo Fisher Scientific).

LC-MS analysis of TMT-SILAC samples. LC-MS analysis was carried out on an EASY-nLC 1200 (Thermo Fisher Scientific) coupled to an Orbitrap Eclipse mass spectrometer (Thermo Fisher Scientific) equipped with a Nanospray Flex ion source.

Peptides (500ng per fraction) were directly loaded onto an Aurora 25cm x 75µm ID, 1.6µm C18 column (Ion Opticks, Victoria, Australia) heated to 50°C. The peptides were separated with a 120 min gradient at a flow rate of 350 nL/min as follows: 2–6% Solvent B (7.5 min), 6-25% B (82.5 min), 25-40% B (30 min), 40-98% B (1 min), and held at 98% B (15 min). Solvent A consisted of 97.8 % H_2O, 2% ACN, and 0.2% formic acid and solvent B consisted of 19.8% H_2O, 80 % ACN, and 0.2% formic acid. MS1 spectra were acquired in the Orbitrap at 120K resolution with a scan range from 350-1800 m/z, an AGC target of $1e^6$, and a maximum injection time of 50 ms in Profile mode. Features were filtered for monoisotopic peaks with a charge state of 2-7 and minimum intensity of $2.5e^4$, with dynamic exclusion set to exclude features after 1 time for 30 seconds with a 5-ppm mass tolerance. A targeted mass difference selection node was also used to monitor for SILAC pairs with a delta mass of 8.0142 Da (Lysine-8) or 10.008 Da (Arginine-10) and trigger both precursors of the SILAC pair for MS2 analysis. HCD fragmentation was performed with fixed collision energy of 32% after quadrupole isolation of features using an isolation window of 0.5 m/z, an AGC target of $5e^4$, and a maximum injection time of 86 ms. MS2 scans were then acquired in the Orbitrap at 50K resolution in Centroid mode with the first mass fixed at 110. Cycle time was set at 3 seconds.

LCMS Data Reduction for TMT-SILAC. Analysis of LCMS proteomic data was performed in Proteome Discoverer 2.5 (Thermo Scientific) (Orsburn, 2021) utilizing a dynamic modification strategy to account for the TMT/SILAC mixed labeling, with the

peptide results ported to R (R Core Team, 2018) for final analysis. All searches were conducted using the Sequest HT (Tabb, 2015) search algorithm with the Escherichia coli proteome (UniProt UP000000625; strain K12 / MG1655 / ATCC 47076; 4,438 proteins covering 440 genes with a BUSCO assessment of 100% genetic coverage). Search parameters were as follows: fully tryptic protease rules with 2 allowed missed cleavages, precursor mass tolerance set to 20 ppm, fragment mass tolerance set to 0.5 Da with only b and y ions accounted for. Percolator (Käll et al., 2007) was used as the validation method, based on q-value, with a maximum FDR set to 0.01. The SequestHT search considered modifications dynamic for Loss of Protein N-term Methionine, Formylation (N-term), Oxidation (M), Carbamidomethyl (C), TMTpro (K, N-term, +304.207 Da), TMTpro-SILAC-K8 (K, +312.221 Da) and SILAC-R10 (R, +10.008 Da). Quantitative analysis is based on TMT MS2 reporter ions generated from HCD fragmentation, with an average reporter S/N threshold of 10.

Peptide data was divided into *light-only* (not containing a SILAC modification) and *heavy-only* (containing a SILAC modification) with normalization accomplished using the R::limma package (Ritchie et al., 2015). Peptides from the two datasets where then merged such that all peptides from the *light-only* dataset had a corresponding *heavy-only* peptide, for a total of 32 TMT (16 *light-only*, 16 *heavy-only*) quantitative measurements per peptide. Protein values were calculated as the sum of each TMT channel for all corresponding peptides, with foldchange (FC) values computed as all pairwise combinations between time

points (*t*1.5h/*t*0h, *t*4.5h/*t*0h, *t*9h/*t*0h), within the light and heavy data sets independently, for a total of 16 FC values per comparison. FC values were additionally log2 transformed.

Statistical analysis and enrichment analysis. Statistical analyses were performed in R, comparing the *light-only* (treated) FC values to the *heavy-only* (untreated) FC values using a two-sample t-test. Significance was determined at an adjusted p-value of 0.05 (Benjamini and Hochberg, 1995), and a threshold of $|\log_2 FC| \geq 0.5$ for 1.5 h, $|\log_2 FC| \geq 1$ for 4.5 and 9 h samples.

Enrichment analysis was performed on differentially expressed genes at each time point using the Functional annotation clustering algorithm from DAVID Bioinformatics Resources 6.8 (Jiao et al., 2012). The analysis was performed with medium classification stringency and included the following annotation categories: Gene Ontology (GO) terms (biological process, molecular function, cellular compartment), Uniprot Keywords and Sequence features, KEGG pathway, and protein domains (InterPro, SMART, and PIR SuperFamily).

Ribosome profiling

Cell culture and ribosome footprint preparation. For ribosome profiling, two parallel experiments (Replicate 1 and 2) and a third independent measurement (Replicate 3) were carried out for a total of 3 biological replicates. E. coli CAG12184 cells were grown in

SILAC medium at 37 ˚C and treated with 4 μg/mL ACT when OD_{600} reached 0.4. At indicated time points, 200 mL of cell culture were harvested by rapid filtration through nitrocellulose membrane with 0.2 mm pores and flash-frozen in liquid nitrogen. Frozen cells were mixed with 0.5 mL of Lysis buffer (50 mM Hepes-KOH, 100 mM NaCl, 10 mM $MgCl_2$, 5 mM $CaCl_2$, 0.4% Triton X-100, 0.1% NP-40, 1 mM chloramphenicol, 1 mM PMSF, 50 U/mL DNaseI (recombinant DNaseI, Roche), pH 7.0) and lysed via mixer milling (1 min, 25 Hz, Retsch). Frozen lysate powder was thawed and centrifuged (3,000 × *g*, 6 min, 4 ˚C) to remove unbroken cells. Lysate containing 0.5 mg total RNA was supplemented with 100 U/mL SUPERase · In (Ambion), and treated with 1875 U of MNase for 15 min in a thermomixer (1,400 rpm, 25 ˚C) before quenching with 6 mM EGTA. Monosomes were then loaded on a 30% sucrose cushion in Wash buffer (50 mM Tris/HCl, 150 mM NaCl, 10 mM $MgCl_2$, 1 mM chloramphenicol, 0.4% Triton X-100, 0.1% NP-40, pH 7.4) containing 1X protease inhibitor cocktail (Complete EDTA-free, Roche), and centrifuged in TLA100.3 rotor at 80,000 rpm for 1.5 h at 4 ˚C. Pellets were then washed and resuspended in Wash buffer. RNA from the purified monosomes were extracted using Direct-zol RNA miniprep kit (Zymo) and loaded onto a 15% polyacrylamide TBE-Urea gel. The 15-45 nt region on the gel was excised, and ribosome protected mRNA footprints were recovered from the gel pieces.

Library preparation. Libraries are prepared as described (Mohammad and Buskirk, 2019) with modifications. Briefly, mRNA footprints were dephosphorylated by T4 polynucleotide kinase (NEB), and ligated to pre-adenylated linkers (Linker-1, Linker-2, and Linker-3 for replicate 1, replicate 2, and replicate 3, respectively) using T4 RNA ligase 2. Ligated products were purified with Oligo and Concentration Kit (Zymo), and samples from replicate 1 and 2 were pooled. Products were separated from excess linkers on a 15% polyacrylamide TBE-Urea gel, and recovered from the gel pieces. Reverse transcription was subsequently carried out using Superscript III RT (Invitrogen) and RT primer, followed by alkaline hydrolysis of the RNA fragments. Reverse-transcribed DNA products were further purified on a 10% polyacrylamide TBE-Urea gel to remove excess RT primers, and circularized using CircLigase (Epicentre). Circularized DNA was amplified via 5-8 cycles of PCR reaction using Phusion polymerase (NEB), PCR Forward primer, and barcoded PCR Reverse primer, and purified on a 8% polyacrylamide native TBE gel. The DNA products were then quantified by Qubit and sequenced on Nextseq 2000.

Sequencing data analysis. Pair-end reads were merged using PEAR (Zhang et al., 2014). Adaptor sequences were trimmed from sequencing reads using Cutadapt. Reads were mapped to bacterial genome using Bowtie after discarding the reads mapping to ribosomal RNAs. The *E.coli* MG1655 reference genome assembly (ASM584v2) was downloaded from EnsemblBacteria (https://bacteria.ensembl.org). Ribosome density was assigned to 14-nt upstream of the 3'-end of reads using reads with size range 15–45 nt. Nucleotide reads at

each codon were then summed based on the gene annotations taken from Uniprot (The UniProt Consortium, 2017). For each gene, the sum of raw reads and RPM-normalized reads at each codon, excluding the first five and last five codons, were calculated. In each replicate, genes with ≥ 64 raw reads in the control sample and ≥ 64 raw reads in at least one of the 3 time points were considered. The fold change (FC) was calculated as the ratio of the RPM value of ACT-treated samples to that of the control (–ACT) sample. Genes with at least 2 valid $\log_2$ FC values from 3 replicates were included in subsequent analyses. Statistical analyses were performed using the two-sample t-test embedded in the Perseus software (version 1.6.14.0)(Tyanova et al., 2016). Significance was determined with thresholds of $|\log_2 FC| \geq 1$ and $p < 0.05$. Enrichment analysis was performed on differentially expressed genes at each time point using the Functional annotation clustering algorithm from DAVID Bioinformatics Resources 6.8(Jiao et al., 2012), as described for the proteomic analysis.

Isolation of nascent protein aggregates. E. coli

CAG12184 cells grown in SILAC medium at 37 ˚C until OD_{600} reached 0.4. Subsequently, the cells were labeled with 10 µCi/mL ^{35}S-Met/Cys EasyTag mix (PerkinElmer) and, where indicated, treated with 4 µg/mL ACT and 20 µM MG132 (Thermo Scientific) for 30 min. Before harvesting, 0.5 mg/mL Met and Cys was added to the culture. Cells from 5 mL of culture were pelleted, resuspended in 250 µL Lysis buffer B (100 mM Hepes-KOH, 0.25 M sucrose, 0.5 mM EDTA, 50 µg/mL lysozyme, 1 mM PMSF, 1X

protease inhibitor cocktail, 20 μM MG132, pH 7.0), and lysed by tip sonication (Branson, 20x at level 5 and 50% duty cycle). Lysates were centrifuged at 2,000 × *g* and 4 ˚C for 5 min to remove unbroken cells. Clarified lysates were centrifuged at 15,000 × *g* and 4 ˚C for 30 min to separate the membrane fraction and aggregates from cytoplasm. The pellets were further resuspended in 200 μL Wash buffer B (100 mM Hepes-KOH, 1 mM PMSF, 1X protease inhibitor cocktail, pH 7.0) with brief sonication. To isolate large protein aggregates, 2% NP-40 was added, and the resuspended pellets were centrifuged again at 15,000 × *g*, 4 ˚C for 30 min. NP-40 insoluble protein aggregates were then resuspended in 50 μL Wash buffer B with 1% SDS. All fractions were then analyzed by SDS-PAGE and quantified by autoradiography.

Bright field microscopy.

CAG12184 cells grown in SILAC medium were treated with 4 μg/mL ACT, collected at indicated time points, washed, and resuspended with PBS to an OD of 1. 2 μL of the cell suspension was spotted onto an agarose (1%)-coated glass slide, and covered with a glass coverslip. Bright field microscopy images were obtained with Revolve Microscope (Echo) with a 100x oil immersion objective.

SDS sensitivity assay

CAG12184 cells grown in SILAC medium to an OD_{600} of 0.4 were mock-treated treated with 4 μg/mL ACT. At indicated time points, an aliquot of cells was pelleted, resuspended with SILAC medium to an OD_{600} of 1, and mixed with equal volume of 0.1% SDS. Cell lysis was monitored on a plate reader continuously for 20 min by the change in OD_{600} value relative to that of the cells without SDS incubation. For Fig. 4.5B, the fraction of remaining cells at 10 min of SDS incubation was recorded.

PI permeability assay

Where indicated, CAG12184 or Δ*fmt*(Piatkov et al., 2015) cells grown in SILAC medium or Luria-Bertani Broth (LB) were treated with 4 μg/mL ACT at an OD_{600} of 0.4. At indicated time points, an aliquot of cells were withdrawn, washed, and resuspended in PI buffer (50 mM Hepes-KOH, 5 mM glucose, pH 7.0) to an OD of 0.5. Resuspended cells were incubated with 5 μM PI for 30 min, and the fluorescence signals were recorded using a plate reader with the excitation wavelength at 535 nm. Independent cell resuspensions were incubated with 2.5 μM Syto9, and the fluorescence signals were measured with the excitation wavelength at 440 nm. The fluorescence intensity of PI at 620 nm was then normalized to that of Syto9 at 505 nm.

Membrane polarization assays

CAG12184 grown in SILAC medium or Δ*fmt* cells grown in LB were treated with 4 μg/mL ACT at an OD_{600} of 0.4. Where indicated, cells were treated with 5 μM CCCP for 5 min before collection. At indicated time points after ACT treatment, cells were withdrawn, washed with PBS, and normalized to an OD_{600} of 0.5. Resuspended cells were incubated with 10 μM ThT at room temperature for 5 min, and the fluorescence signals were recorded using a plate reader at the excitation wavelength of 450 nm.

For measurements using $DiOC_2(3)$, cells were collected, resuspended to an OD_{600} of 1 with PBS, and treated with 10 mM EDTA for 5 min. The cell suspension was then washed and resuspended in MP buffer (130 mM NaCl, 60 mM Na_2HPO_4, 60 mM NaH_2PO_4, 10 mM glucose, 5 mM KCl, 0.5 mM $MgCl_2$, pH 7.0). The cell suspension was loaded with 30 μM $DiOC_2(3)$ and incubated at room temperature for 15 min, followed by fluorescence measurement with an excitation wavelength of 450 nm.

Measurement of NAD(P)$^+$ and NAD(P)H

The cellular concentrations of $NAD(P)^+$ and NAD(P)H were measured as described(Kern et al., 2014). Briefly, CAG12184 cells grown in SILAC medium were treated with 4 μg/mL ACT for 9 h. Cell aliquots were withdrawn, pelleted, and incubated at 50 ˚C for 10 min in 0.2 M NaOH for $NAD(P)^+$ or 0.2 M HCl for NAD(P)H extraction. The lysate was then neutralized and clarified by centrifugation at 16,000 × *g*, 4 ˚C for 5 min. For NAD^+ and NADH measurements, 5 μL of the lysate was incubated at 30 ˚C for 10 min with 90 μL

of the reagent mix containing 110 mM bicine buffer (pH 8.0), 11% (v/v) ethanol, 4.4 mM EDTA, 0.47 mM MTT (methylthiazolyldiphenyl-tetrazolium bromide), and 3.7 mM PES (phenazine ethosulfate). 5 µL of 1 mg/mL Alcohol dehydrogenase II (ADH II, Sigma) was added to initiate the reaction, and the absorbance at 570 nm was monitored for 20 min at 30 ˚C in a plate reader. $NADP^+$ and NADPH measurements were carried out similarly, except that ethanol in the reagent mix was replaced with 2.8 mM glucose-6-phosphate, and 5 µL of 0.1 mg/mL Glucose-6-phosphate dehydrogenase (Sigma) was used to initiate the reaction. The velocities of the reactions were normalized by cell density, and the relative amount of NAD(P)(H) was reported as the ratio of the normalized values between ACT-treated and untreated samples.

4.5. Supplementary Figures

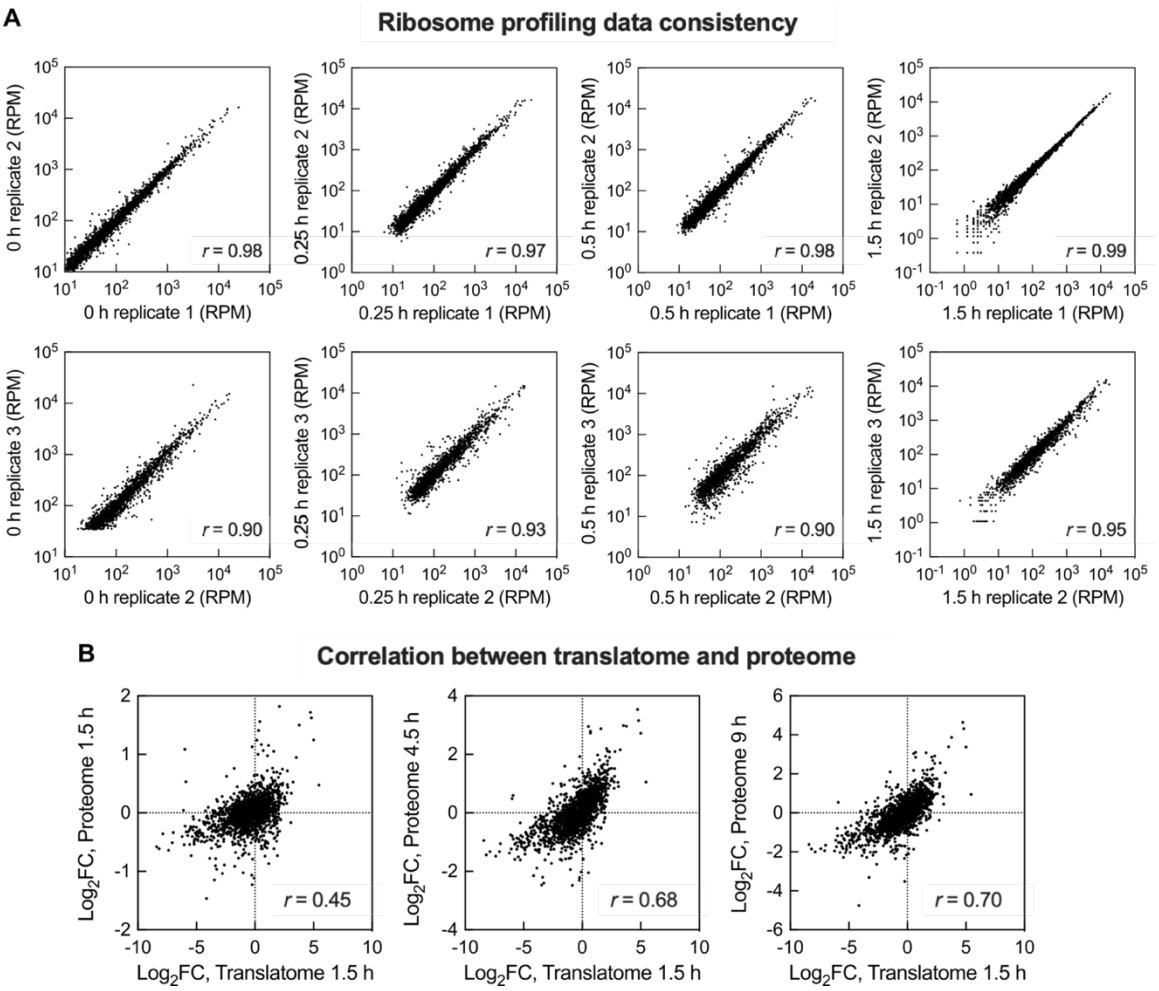

Figure S4.1. Ribosome profiling of cells under PDF inhibition.

(A) Scatter plots depicting the correlation of the ribosome profiling data between three biological replicates. Pearson correlation coefficients (r) computed from the normalized read values (reads per million, RPM) of genes present in both datasets being compared were shown. **(B)** Scatter plots depicting the correlation between the changes in translation at 1.5 h and steady-state protein levels at the indicated time of ACT treatment.

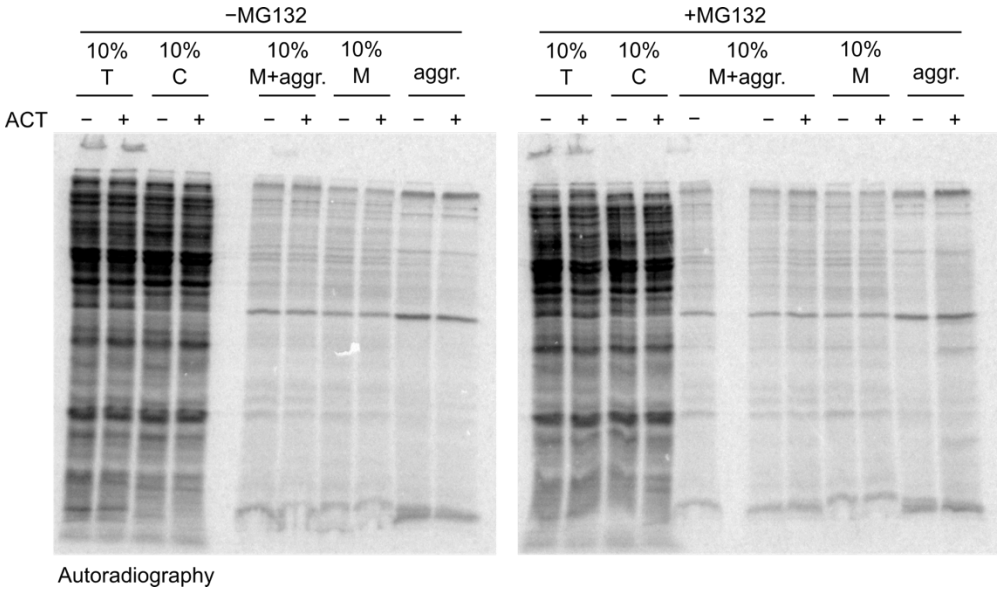

Figure S4.2. Nascent protein aggregates upon PDF inhibition.

Representative autoradiographs of cellular fractions from CAG12184 cells treated with ACT and/or MG132, related to Figs. 4.4B and C. T: total cell lysate; C: cytoplasm; M: membrane; aggr.: NP40-insoluble protein aggregates.

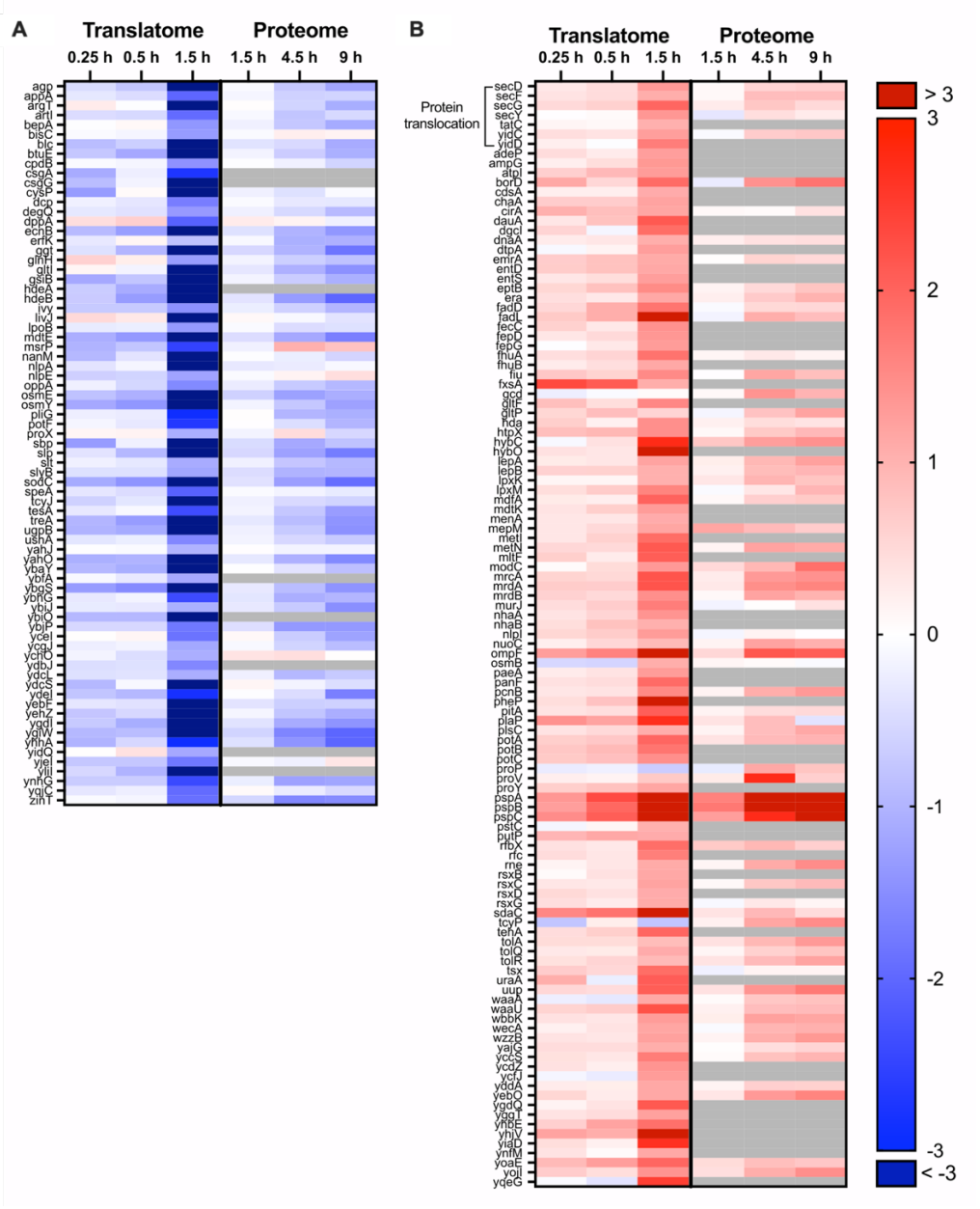

Figure S4.3. Differential expression of membrane and secretory proteins.

Time-dependent changes of secretory proteins ($\log_2$ FC ≤ -1) **(A)** and membrane proteins ($\log_2$ FC ≥ 1) **(B)** after ACT treatment in the ribosome profiling (left) or proteomic (right) data.

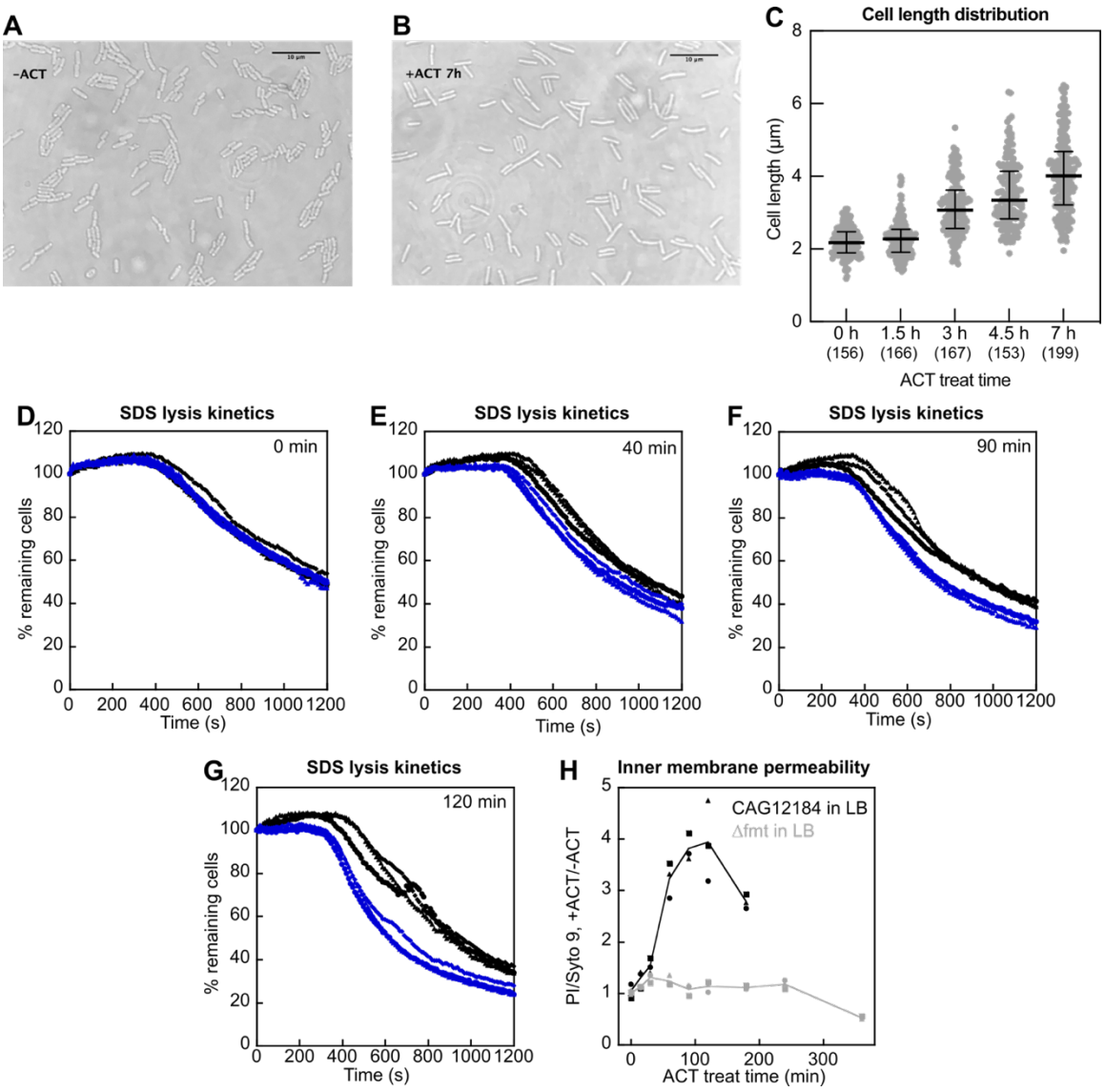

Figure S4.4. Membrane-associated phenotypes upon PDF inhibition.

(A) and **(B)** Representative bright-field microscopy images of CAG12184 cells before (A) and after (B) 7 h of ACT treatment. Scale bars: 10 μm. **(C)** Quantification of the cell length from the microscopy images during PDF inhibition. Data are shown as median ± interquartile with individual values displayed. The number of cells quantified in each time point are shown in parentheses. **(D)-(G)** Time-dependent profiles of cell lysis by SDS. CAG12184 cells without (black) or with (blue) ACT treatment for the indicated times were

mixed with 0.05% SDS, and the cell density was monitored by OD_{600} for 20 min. Data are shown as individual values from 3 biological replicates. **(H)** Inner membrane integrity of CAG12184 (black) and Δ*fmt* (gray) cells grown in Luria-Bertani medium (LB) upon ACT treatment, measured by the fluorescence ratio between PI and Syto 9 and normalized to the value of untreated cells. Data are shown as individual values from three biological replicates, where the line represents the mean.

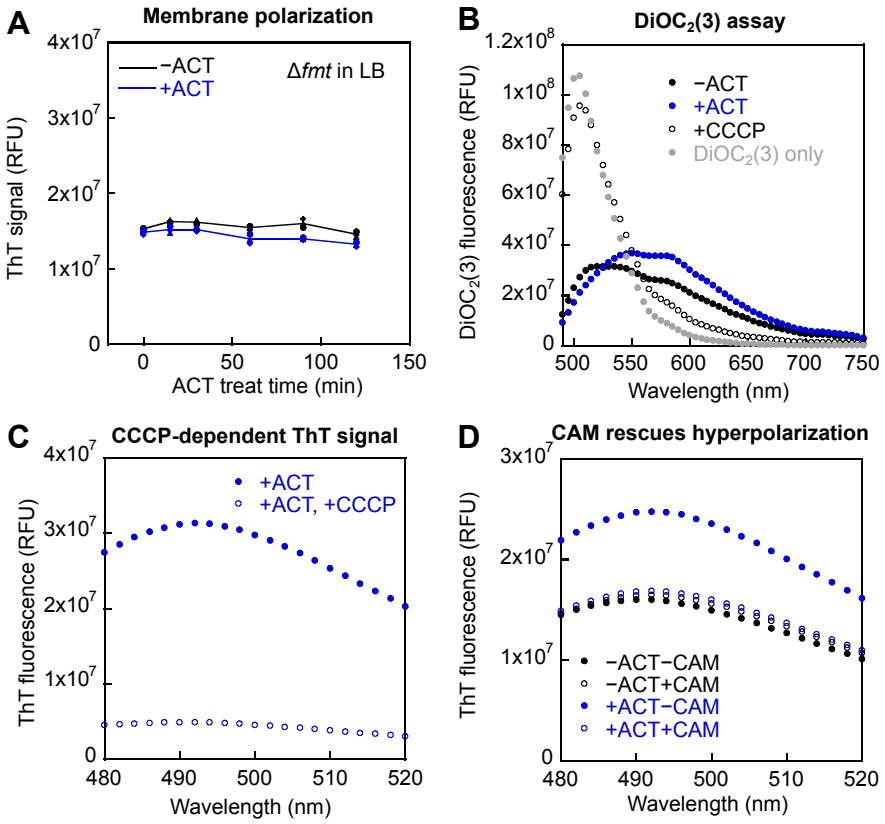

Figure S4.5. Membrane polarization upon PDF inhibition.

(A) Membrane potential of Δ*fmt* cells grown in LB without (black) and with (blue) ACT treatment, measured by the fluorescence signal of ThT at 485 nm. Data are shown as individual values from three replicates, where the line represents the mean. **(B)** $DiOC_2(3)$ fluorescence spectra measured with CAG12184 cells before (solid black) and after 2 h of 4 µg/mL ACT treatment (solid blue), and after 5 min of 5 µM CCCP treatment (open black). The spectrum of $DiOC_2(3)$ without cells is shown in gray. **(C)** ThT fluorescence spectra of

CAG12184 cells after 60 min of 4 µg/mL ACT treatment (solid blue), followed by the treatment with 5 µM CCCP for 5 min (open blue). **(D)** ThT fluorescence spectra with CAG12184 cells treated with the indicated combination of ACT (4 µg/mL) and chloramphenicol (CAM, 25 µg/mL) for 30 min.

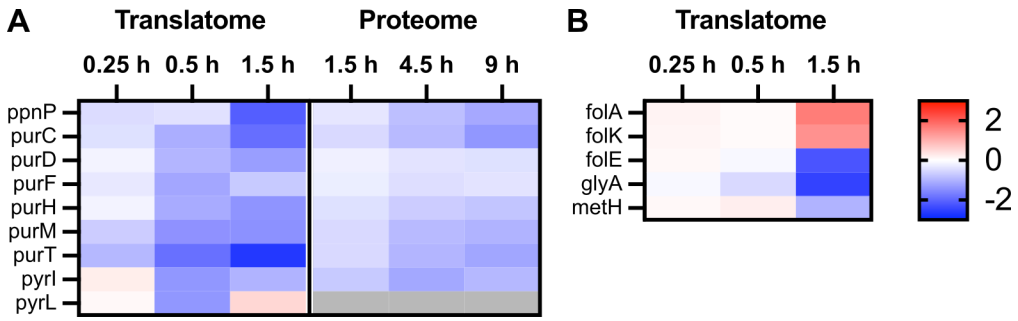

Figure S4.6. Inhibition of PDF perturbs nucleotide biosynthesis.

(A) Time-dependent changes (log_2FC) in the translation (left) and steady-state protein level (right) of genes involved in *de novo* purine and pyrimidine biosynthesis. **(B)** Time-dependent changes (log_2FC) in the translation of selected genes involved in tetrahydrofolate (THF) conversion.

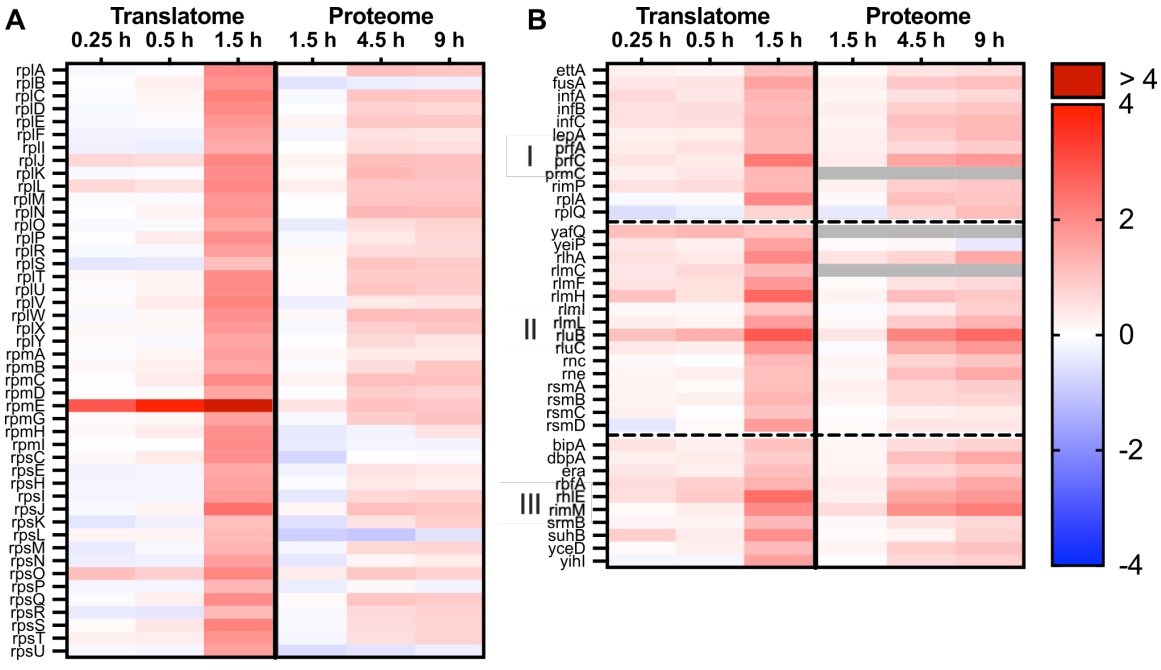

Figure S4.7. Inhibition of PDF induces the expression of translation machineries.

(A) Time-dependent changes of ribosomal proteins ($\log_2$ FC ≥ 1) after ACT treatment in the ribosome profiling (left) or proteomic (right) data. **(B)** Time-dependent changes ($\log_2$FC ≥ 1) of genes involved in translation (I), rRNA modification (II), and ribosome biogenesis (III).

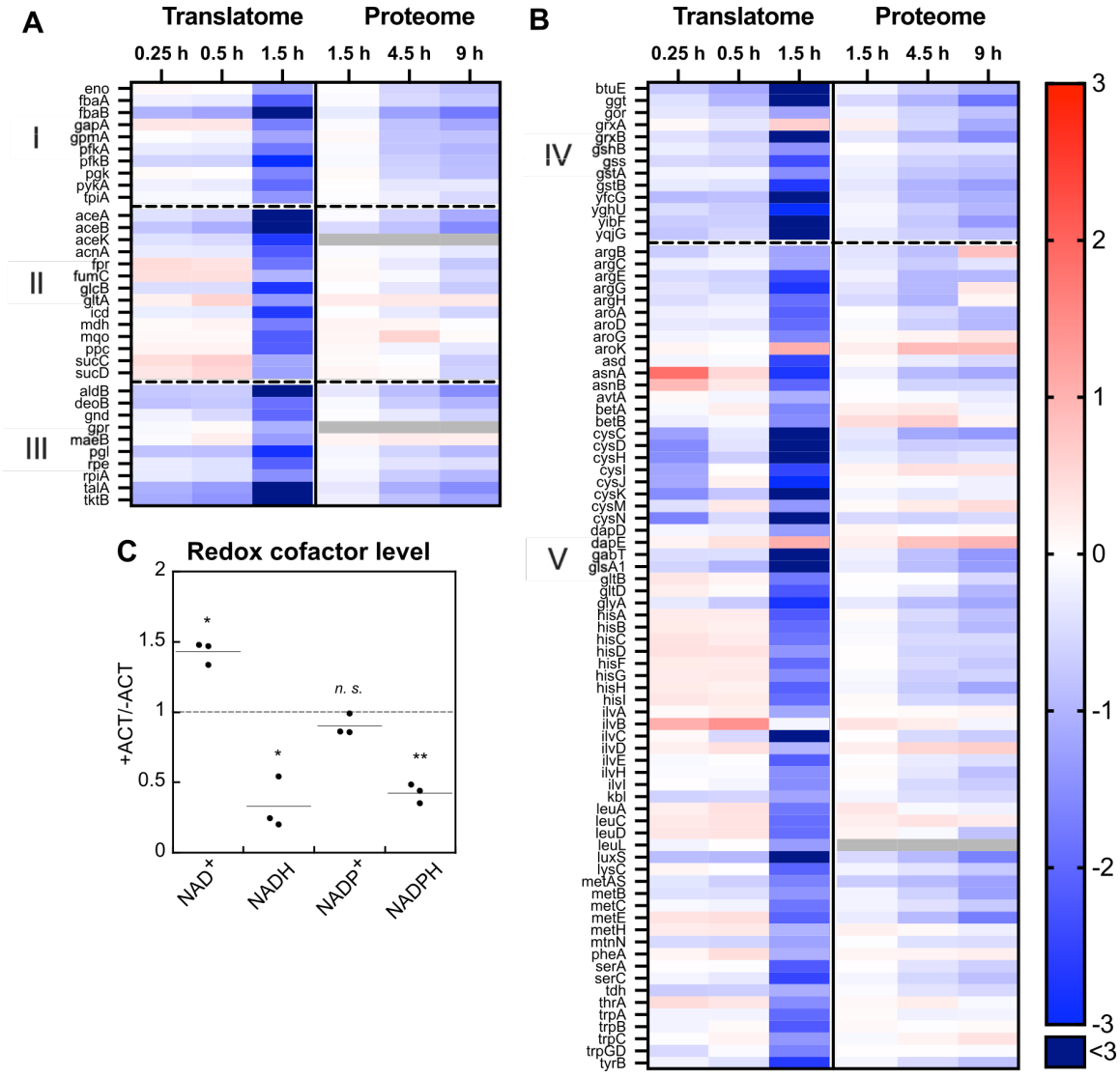

Figure S4.8. Inhibition of PDF disrupts cellular metabolism and redox homeostasis.

(A) Time-dependent changes ($log_2FC \leq -1$) in the translation (left) or steady-state protein level (right) of genes involved in glycolysis (I), TCA cycle (II) and NADPH biogenesis pathways (III). **(B)** Time-dependent changes ($log_2FC \leq -1$) of genes involved in glutathione metabolism (VI) and biosynthesis pathways of amino acids (V). **(C)** Cellular level of the indicated cofactors in CAG12184 cells after 9 h of ACT treatment, normalized to that of the cells grown without ACT. Data are shown as mean with individual values from 3 biological replicates. *: $p < 0.05$; **: $p < 0.01$; n. s.: $p \geq 0.05$.

BIBLIOGRAPHY

Adams, J.M. (1968). On the release of the formyl group from nascent protein. J Mol Biol *33*, 571–589.

Adams, J.M., and Capecchi, M.R. (1966). N-formylmethionyl-sRNA as the initiator of protein synthesis. PNAS *55*, 147–155.

Agashe, V.R., Guha, S., Chang, H.-C., Genevaux, P., Hayer-Hartl, M., Stemp, M., Georgopoulos, C., Hartl, F.U., and Barral, J.M. (2004). Function of Trigger Factor and DnaK in Multidomain Protein Folding: Increase in Yield at the Expense of Folding Speed. Cell *117*, 199–209.

Akbar, S., Bhakta, S., and Sengupta, J. (2021). Structural insights into the interplay of protein biogenesis factors with the 70S ribosome. Structure 755–767.

Akopian, D., Shen, K., Zhang, X., and Shan, S.O. (2013). Signal recognition particle: an essential protein-targeting machine. Annu. Rev. Biochem. *82*, 693–721.

Aksnes, H., Ree, R., and Arnesen, T. (2019). Co-translational, Post-translational, and Non-catalytic Roles of N-Terminal Acetyltransferases. Molecular Cell *73*, 1097–1114.

Antoun, A., Pavlov, M.Y., Lovmar, M., and Ehrenberg, M. (2006). How Initiation Factors Maximize the Accuracy of tRNA Selection in Initiation of Bacterial Protein Synthesis. Molecular Cell *23*, 183–193.

Ariosa, A., Lee, J.H., Wang, S., Saraogi, I., and Shan, S.O. (2015). Regulation by a chaperone improves substrate selectivity during cotranslational protein targeting. Proc. Natl. Acad. Sci. U.S.A. *112*, 3169–3178.

Barria, C., Malecki, M., and Arraiano, C.M. (2013). Bacterial adaptation to cold. Microbiology *159*, 2437–2443.

Baxter, R.L., and Scott, A.I. (1984). 1.04 - Biosynthesis of Some Heterocyclic Natural Products. In Comprehensive Heterocyclic Chemistry, A.R. Katritzky, and C.W. Rees, eds. (Oxford: Pergamon), pp. 83–109.

Bearne, S.L. (1996). Active Site-directed Inactivation of Escherichia coli Glucosamine-6-phosphate Synthase. J. Biol. Chem. *271*, 3052–3057.

Beck, K., Wu, L.F., Brunner, J., and Muller, M. (2000). Discrimination between SRP- and SecA/SecB-dependent substrates involves selective recognition of nascent chains by SRP and trigger factor. EMBO J. *19*, 134–143.

Ben-Bassat, A., Bauer, K., Chang, S.Y., Myambo, K., Boosman, A., and Chang, S. (1987). Processing of the initiation methionine from proteins: properties of the Escherichia coli methionine aminopeptidase and its gene structure. Journal of Bacteriology *169*, 751–757.

Benjamini, Y., and Hochberg, Y. (1995). Controlling the False Discovery Rate: A Practical and Powerful Approach to Multiple Testing. Journal of the Royal Statistical Society: Series B (Methodological) *57*, 289–300.

Bhakta, S., Akbar, S., and Sengupta, J. (2019). Cryo-EM Structures Reveal Relocalization of MetAP in the Presence of Other Protein Biogenesis Factors at the Ribosomal Tunnel Exit. J. Mol. Biol. *431*, 1426–1439.

Bienvenut, W.V., Giglione, C., and Meinnel, T. (2015). Proteome-wide analysis of the amino terminal status of Escherichia coli proteins at the steady-state and upon deformylation inhibition. Proteomics *15*, 2503–2518.

Bingel-Erlenmeyer, R., Kohler, R., Kramer, G., Sandikci, A., Antolic, S., Maier, T., Schaffitzel, C., Wiedmann, B., Bukau, B., and Ban, N. (2008). A peptide deformylase-ribosome complex reveals mechanism of nascent chain processing. Nature *452*, 108–111.

Boissel, J.P., Kasper, T.J., and Bunn, H.F. (1988). Cotranslational amino-terminal processing of cytosolic proteins. Cell-free expression of site-directed mutants of human hemoglobin. J. Biol. Chem. *263*, 8443–8449.

Bornemann, T., Holtkamp, W., and Wintermeyer, W. (2014). Interplay between trigger factor and other protein biogenesis factors on the ribosome. Nat. Commun. *5*, 4180.

Brannigan, J.A., Dodson, G., Duggleby, H.J., Moody, P.C.E., Smith, J.L., Tomchick, D.R., and Murzin, A.G. (1995). A protein catalytic framework with an N-terminal nucleophile is capable of self-activation. Nature *378*, 416–419.

Buskirk, A.R., and Green, R. (2017). Ribosome pausing, arrest and rescue in bacteria and eukaryotes. Philos. Trans. R. Soc. Lond., B, Biol. Sci. *372*, 20160183.

BUSSE, H.-J., WÖSTMANN, C., and BARKER, E.P.Y. 1992 (1992). The bactericidal action of streptomycin: membrane permeabilization caused by the insertion of mistranslated proteins into the cytoplasmic membrane of Escherichia coli and subsequent caging of the antibiotic inside the cells due to degradation of these proteins. Microbiology *138*, 551–561.

Cabrita, L.D., Cassaignau, A.M.E., Launay, H.M.M., Waudby, C.A., Wlodarski, T., Camilloni, C., Karyadi, M.-E., Robertson, A.L., Wang, X., Wentink, A.S., et al. (2016). A structural ensemble of a ribosome–nascent chain complex during cotranslational protein folding. Nature Structural & Molecular Biology *23*, 278–285.

Calhoun, K.A., and Swartz, J.R. (2006). Total amino acid stabilization during cell-free protein synthesis reactions. J Biotechnol *123*, 193–203.

Cassaignau, A.M.E., Włodarski, T., Chan, S.H.S., Woodburn, L.F., Bukvin, I.V., Streit, J.O., Cabrita, L.D., Waudby, C.A., and Christodoulou, J. (2021). Interactions between nascent proteins and the ribosome surface inhibit co-translational folding. Nat. Chem. 1–7.

Catanzariti, A.-M., Soboleva, T.A., Jans, D.A., Board, P.G., and Baker, R.T. (2004). An efficient system for high-level expression and easy purification of authentic recombinant proteins. Protein Science *13*, 1331–1339.

Chang, S.Y., McGary, E.C., and Chang, S. (1989). Methionine aminopeptidase gene of Escherichia coli is essential for cell growth. Journal of Bacteriology *171*, 4071–4072.

Chen, D.Z., Patel, D.V., Hackbarth, C.J., Wang, W., Dreyer, G., Young, D.C., Margolis, P.S., Wu, C., Ni, Z.J., Trias, J., et al. (2000). Actinonin, a naturally occurring antibacterial agent, is a potent deformylase inhibitor. Biochemistry *39*, 1256–1262.

Chiba, S., Akiyama, Y., Mori, H., Matsuo, E., and Ito, K. (2000). Length recognition at the N-terminal tail for the initiation of FtsH-mediated proteolysis. EMBO Reports *1*, 47–52.

Chiba, S., Akiyama, Y., and Ito, K. (2002). Membrane Protein Degradation by FtsH Can Be Initiated from Either End. Journal of Bacteriology *184*, 4775–4782.

Ciryam, P., Morimoto, R.I., Vendruscolo, M., Dobson, C.M., and O'Brien, E.P. (2013). In vivo translation rates can substantially delay the cotranslational folding of the Escherichia coli cytosolic proteome. Proc. Natl. Acad. Sci. U.S.A. *110*, 132–140.

Clatterbuck Soper, S.F., Dator, R.P., Limbach, P.A., and Woodson, S.A. (2013). In Vivo X-Ray Footprinting of Pre-30S Ribosomes Reveals Chaperone-Dependent Remodeling of Late Assembly Intermediates. Molecular Cell *52*, 506–516.

Cleland, W.W. (1975). Partition analysis and concept of net rate constants as tools in enzyme kinetics. Biochemistry *14*, 3220–3224.

Copik, A.J., Swierczek, S.I., Lowther, W.T., D'Souza V, M., Matthews, B.W., and Holz, R.C. (2003). Kinetic and spectroscopic characterization of the H178A methionyl aminopeptidase from Escherichia coli. Biochemistry *42*, 6283–6292.

Cruz-Vera, L.R., Rajagopal, S., Squires, C., and Yanofsky, C. (2005). Features of Ribosome-Peptidyl-tRNA Interactions Essential for Tryptophan Induction of tna Operon Expression. Molecular Cell *19*, 333–343.

Cumberlidge, A.G., and Isono, K. (1979). Ribosomal protein modification in Escherichia coli: I. A mutant lacking the N-terminal acetylation of protein S5 exhibits thermosensitivity. Journal of Molecular Biology *131*, 169–189.

Dai, X., Zhu, M., Warren, M., Balakrishnan, R., Patsalo, V., Okano, H., Williamson, J.R., Fredrick, K., Wang, Y.-P., and Hwa, T. (2017). Reduction of translating ribosomes enables *Escherichia coli* to maintain elongation rates during slow growth. Nat Microbiol *2*, 16231.

Datsenko, K.A., and Wanner, B.L. (2000). One-step inactivation of chromosomal genes in Escherichia coli K-12 using PCR products. Proc. Natl. Acad. Sci. U.S.A. *97*, 6640–6645.

Davis, B.D., Chen, L.L., and Tai, P.C. (1986). Misread protein creates membrane channels: an essential step in the bactericidal action of aminoglycosides. PNAS *83*, 6164–6168.

De Geyter, J., Portaliou, A.G., Srinivasu, B., Krishnamurthy, S., Economou, A., and Karamanou, S. (2020). Trigger factor is a bona fide secretory pathway chaperone that interacts with SecB and the translocase. EMBO Rep *21*, e49054.

Deckert, A., Cassaignau, A.M.E., Wang, X., Włodarski, T., Chan, S.H.S., Waudby, C.A., Kirkpatrick, J.P., Vendruscolo, M., Cabrita, L.D., and Christodoulou, J. (2021). Common sequence motifs of nascent chains engage the ribosome surface and trigger factor. Proc Natl Acad Sci U S A *118*, e2103015118.

Deuerling, E., Schulze-Specking, A., Tomoyasu, T., Mogk, A., and Bukau, B. (1999). Trigger factor and DnaK cooperate in folding of newly synthesized proteins. Nature *400*, 693–696.

Deuerling, E., Patzelt, H., Vorderwülbecke, S., Rauch, T., Kramer, G., Schaffitzel, E., Mogk, A., Schulze-Specking, A., Langen, H., and Bukau, B. (2003). Trigger Factor and DnaK possess overlapping substrate pools and binding specificities. Molecular Microbiology *47*, 1317–1328.

Doud, S.K., Chou, M.M., and Kendall, D.A. (1993). Titration of protein transport activity by incremental changes in signal peptide hydrophobicity. Biochemistry *32*, 1251–1256.

D'Souza V, M., and Holz, R.C. (1999). The methionyl aminopeptidase from Escherichia coli can function as an iron(II) enzyme. Biochemistry *38*, 11079–11085.

Dummitt, B., Micka, W.S., and Chang, Y.-H. (2003). N-terminal methionine removal and methionine metabolism in Saccharomyces cerevisiae. Journal of Cellular Biochemistry *89*, 964–974.

Duroc, Y., Giglione, C., and Meinnel, T. (2009). Mutations in Three Distinct Loci Cause Resistance to Peptide Deformylase Inhibitors in Bacillus subtilis. Antimicrobial Agents and Chemotherapy *53*, 1673–1678.

Duthie, S.J., Narayanan, S., Brand, G.M., Pirie, L., and Grant, G. (2002). Impact of Folate Deficiency on DNA Stability. The Journal of Nutrition *132*, 2444S-2449S.

Eisner, G., Moser, M., Schäfer, U., Beck, K., and Müller, M. (2006). Alternate Recruitment of Signal Recognition Particle and Trigger Factor to the Signal Sequence of a Growing Nascent Polypeptide. Journal of Biological Chemistry *281*, 7172–7179.

Ezraty, B., Vergnes, A., Banzhaf, M., Duverger, Y., Huguenot, A., Brochado, A.R., Su, S.-Y., Espinosa, L., Loiseau, L., Py, B., et al. (2013). Fe-S Cluster Biosynthesis Controls Uptake of Aminoglycosides in a ROS-Less Death Pathway. Science *340*, 1583–1587.

Fauvet, B., Fares, M.-B., Samuel, F., Dikiy, I., Tandon, A., Eliezer, D., and Lashuel, H.A. (2012). Characterization of Semisynthetic and Naturally Nα-Acetylated α-Synuclein in Vitro and in Intact Cells: IMPLICATIONS FOR AGGREGATION AND CELLULAR PROPERTIES OF α-SYNUCLEIN. Journal of Biological Chemistry *287*, 28243–28262.

Fedyukina, D.V., and Cavagnero, S. (2011). Protein Folding at the Exit Tunnel. Annu Rev Biophys *40*, 337–359.

Fedyukina, D.V., Jennaro, T.S., and Cavagnero, S. (2014). Charge Segregation and Low Hydrophobicity Are Key Features of Ribosomal Proteins from Different Organisms. Journal of Biological Chemistry *289*, 6740–6750.

Ferbitz, L., Maier, T., Patzelt, H., Bukau, B., Deuerling, E., and Ban, N. (2004). Trigger factor in complex with the ribosome forms a molecular cradle for nascent proteins. Nature *431*, 590–596.

Fersht, A. (1998). Measurement and Magnitude of Individual Rate Constants. In Structure and Mechanism in Protein Science: A Guide to Enzyme Catalysis and Protein Folding, M.R. Julet, and G.L. Hadler, eds. (W. H. Freeman), pp. 158–167.

Fieulaine, S., Boularot, A., Artaud, I., Desmadril, M., Dardel, F., Meinnel, T., and Giglione, C. (2011). Trapping Conformational States Along Ligand-Binding Dynamics of Peptide Deformylase: The Impact of Induced Fit on Enzyme Catalysis. PLOS Biology *9*, e1001066.

Flores-Kim, J., and Darwin, A.J. (2016). The Phage Shock Protein Response. Annu. Rev. Microbiol. *70*, 83–101.

Forte, G.M., Pool, M.R., and Stirling, C.J. (2011). N-terminal acetylation inhibits protein targeting to the endoplasmic reticulum. PLoS Biol *9*, e1001073.

Foster, J.W. (2004). Escherichia coli acid resistance: tales of an amateur acidophile. Nat Rev Microbiol *2*, 898–907.

Fox, N.K., Brenner, S.E., and Chandonia, J.-M. (2014). SCOPe: Structural Classification of Proteins—extended, integrating SCOP and ASTRAL data and classification of new structures. Nucleic Acids Research *42*, D304–D309.

Friedrich, U.A., Zedan, M., Hessling, B., Fenzl, K., Gillet, L., Barry, J., Knop, M., Kramer, G., and Bukau, B. (2021). Nα-terminal acetylation of proteins by NatA and NatB serves distinct physiological roles in Saccharomyces cerevisiae. Cell Reports *34*, 108711.

Frottin, F., Martinez, A., Peynot, P., Mitra, S., Holz, R.C., Giglione, C., and Meinnel, T. (2006). The proteomics of N-terminal methionine cleavage. Mol. Cell Proteomics *5*, 2336–2349.

Frottin, F., Espagne, C., Traverso, J.A., Mauve, C., Valot, B., Lelarge-Trouverie, C., Zivy, M., Noctor, G., Meinnel, T., and Giglione, C. (2009). Cotranslational Proteolysis Dominates Glutathione Homeostasis to Support Proper Growth and Development. The Plant Cell *21*, 3296–3314.

Frottin, F., Bienvenut, W.V., Bignon, J., Jacquet, E., Jacome, A.S.V., Dorsselaer, A.V., Cianferani, S., Carapito, C., Meinnel, T., and Giglione, C. (2016). MetAP1 and MetAP2 drive cell selectivity for a potent anti-cancer agent in synergy, by controlling glutathione redox state. Oncotarget *7*, 63306–63323.

Fujii, K., Susanto, T.T., Saurabh, S., and Barna, M. (2018). Decoding the Function of Expansion Segments in Ribosomes. Mol. Cell *72*, 1013-1020.e6.

Gasteiger, E., Hoogland, C., Gattiker, A., Duvaud, S., Wilkins, M.R., Appel, R.D., and Bairoch, A. (2005). Protein Identification and Analysis Tools on the ExPASy Server. In The Proteomics Protocols Handbook, J.M. Walker, ed. (Totowa, NJ: Humana Press), pp. 571–607.

Gibson, D.G., Young, L., Chuang, R.-Y., Venter, J.C., Hutchison, C.A., and Smith, H.O. (2009). Enzymatic assembly of DNA molecules up to several hundred kilobases. Nat. Methods *6*, 343–345.

Giglione, C., Pierre, M., and Meinnel, T. (2000). Peptide deformylase as a target for new generation, broad spectrum antimicrobial agents. Mol Microbiol *36*, 1197–1205.

Giglione, C., Boularot, A., and Meinnel, T. (2004). Protein N-terminal methionine excision. Cell Mol Life Sci *61*, 1455–1474.

Giglione, C., Fieulaine, S., and Meinnel, T. (2015). N-terminal protein modifications: Bringing back into play the ribosome. Biochimie *114*, 134–146.

Gordiyenko, Y., Deroo, S., Zhou, M., Videler, H., and Robinson, C.V. (2008). Acetylation of L12 increases interactions in the Escherichia coli ribosomal stalk complex. J Mol Biol *380*, 404–414.

Gordon, J.I., Duronio, R.J., Rudnick, D.A., Adams, S.P., and Gokel, G.W. (1991). Protein N-myristoylation. J. Biol. Chem. *266*, 8647–8650.

Gottesman, S., Roche, E., Zhou, Y., and Sauer, R.T. (1998). The ClpXP and ClpAP proteases degrade proteins with carboxy-terminal peptide tails added by the SsrA-tagging system. Genes Dev. *12*, 1338–1347.

Greenfield, N.J., Stafford, W.F., and Hitchcock-DeGregori, S.E. (1994). The effect of N-terminal acetylation on the structure of an N-terminal tropomyosin peptide and alpha alpha-tropomyosin. Protein Sci *3*, 402–410.

Griffith, E.C., Su, Z., Niwayama, S., Ramsay, C.A., Chang, Y.-H., and Liu, J.O. (1998). Molecular recognition of angiogenesis inhibitors fumagillin and ovalicin by methionine aminopeptidase 2. PNAS *95*, 15183–15188.

Gu, S.-Q., Peske, F., Wieden, H.-J., Rodnina, M.V., and Wintermeyer, W. (2003). The signal recognition particle binds to protein L23 at the peptide exit of the Escherichia coli ribosome. RNA *9*, 566–573.

Gualerzi, C.O., and Pon, C.L. (1990). Initiation of mRNA translation in prokaryotes. Biochemistry *29*, 5881–5889.

Guillon, J.M., Mechulam, Y., Schmitter, J.M., Blanquet, S., and Fayat, G. (1992). Disruption of the gene for Met-tRNA(fMet) formyltransferase severely impairs growth of Escherichia coli. Journal of Bacteriology *174*, 4294–4301.

Guimaraes, C.P., Witte, M.D., Theile, C.S., Bozkurt, G., Kundrat, L., Blom, A.E., and Ploegh, H.L. (2013). Site-specific C-terminal internal loop labeling of proteins using sortase-mediated reactions. Nat Protoc *8*, 1787–1799.

Guzman, L.M., Belin, D., Carson, M.J., and Beckwith, J. (1995). Tight regulation, modulation, and high-level expression by vectors containing the arabinose PBAD promoter. Journal of Bacteriology *177*, 4121–4130.

Guzman-Luna, V., Fuchs, A.M., Allen, A.J., Staikos, A., and Cavagnero, S. (2021). An intrinsically disordered nascent protein interacts with specific regions of the ribosomal surface near the exit tunnel. Commun Biol *4*, 1–17.

Hartl, F.U., Lecker, S., Schiebel, E., Hendrick, J.P., and Wickner, W. (1990). The binding cascade of SecB to SecA to SecY/E mediates preprotein targeting to the E. coli plasma membrane. Cell *63*, 269–279.

Hirel, P.H., Schmitter, M.J., Dessen, P., Fayat, G., and Blanquet, S. (1989). Extent of N-terminal methionine excision from Escherichia coli proteins is governed by the side-chain length of the penultimate amino acid. Proc. Natl. Acad. Sci. U.S.A. *86*, 8247–8251.

Hu, X., Addlagatta, A., Lu, J., Matthews, B.W., and Liu, J.O. (2006). Elucidation of the function of type 1 human methionine aminopeptidase during cell cycle progression. Proc. Natl. Acad. Sci. U.S.A. *103*, 18148–18153.

Hu, Y.J., Wei, Y., Zhou, Y., Rajagopalan, P.T., and Pei, D. (1999). Determination of substrate specificity for peptide deformylase through the screening of a combinatorial peptide library. Biochemistry *38*, 643–650.

Huang, D.W., Sherman, B.T., Tan, Q., Collins, J.R., Alvord, W.G., Roayaei, J., Stephens, R., Baseler, M.W., Lane, H.C., and Lempicki, R.A. (2007). The DAVID Gene Functional Classification Tool: a novel biological module-centric algorithm to functionally analyze large gene lists. Genome Biology *8*, R183.

Huang, D.W., Sherman, B.T., and Lempicki, R.A. (2009). Systematic and integrative analysis of large gene lists using DAVID bioinformatics resources. Nature Protocols *4*, 44–57.

Huber, D., Rajagopalan, N., Preissler, S., Rocco, M.A., Merz, F., Kramer, G., and Bukau, B. (2011). SecA interacts with ribosomes in order to facilitate posttranslational translocation in bacteria. Mol. Cell *41*, 343–353.

Huber, D., Jamshad, M., Hanmer, R., Schibich, D., Doring, K., Marcomini, I., Kramer, G., and Bukau, B. (2017). SecA Cotranslationally Interacts with Nascent Substrate Proteins In Vivo. Journal of Bacteriology *199*, e00622-16.

Hudson, M.A., Siegele, D.A., and Lockless, S.W. (2020). Use of a Fluorescence-Based Assay To Measure *Escherichia coli* Membrane Potential Changes in High Throughput. Antimicrobial Agents and Chemotherapy *64*.

Humbert, R., and Simoni, R.D. (1980). Genetic and biomedical studies demonstrating a second gene coding for asparagine synthetase in Escherichia coli. J Bacteriol *142*, 212–220.

Hwang, C.S., Shemorry, A., and Varshavsky, A. (2010). N-terminal acetylation of cellular proteins creates specific degradation signals. Science *327*, 973–977.

Ingolia, N.T., Brar, G.A., Rouskin, S., McGeachy, A.M., and Weissman, J.S. (2012). The ribosome profiling strategy for monitoring translation in vivo by deep sequencing of ribosome-protected mRNA fragments. Nat Protoc *7*, 1534–1550.

Jarvis, J.A., Ryan, M.T., Hoogenraad, N.J., Craik, D.J., and H∅j, P.B. (1995). Solution Structure of the Acetylated and Noncleavable Mitochondrial Targeting Signal of Rat Chaperonin 10 (∗). Journal of Biological Chemistry *270*, 1323–1331.

Jewett, M.C., and Swartz, J.R. (2004). Mimicking the Escherichia coli cytoplasmic environment activates long-lived and efficient cell-free protein synthesis. Biotechnol. Bioeng. *86*, 19–26.

Jiao, X., Sherman, B.T., Huang, D.W., Stephens, R., Baseler, M.W., Lane, H.C., and Lempicki, R.A. (2012). DAVID-WS: a stateful web service to facilitate gene/protein list analysis. Bioinformatics *28*, 1805–1806.

Jomaa, A., Boehringer, D., Leibundgut, M., and Ban, N. (2016). Structures of the E. coli translating ribosome with SRP and its receptor and with the translocon. Nat Commun *7*, 10471.

Jones, J.D., and O'Connor, C.D. (2011). Protein acetylation in prokaryotes. PROTEOMICS *11*, 3012–3022.

Jovanovic, G., Mehta, P., Ying, L., and Buck, M. 2014 Anionic lipids and the cytoskeletal proteins MreB and RodZ define the spatio-temporal distribution and function of membrane stress controller PspA in Escherichia coli. Microbiology *160*, 2374–2386.

Ju, H.-Q., Lin, J.-F., Tian, T., Xie, D., and Xu, R.-H. (2020). NADPH homeostasis in cancer: functions, mechanisms and therapeutic implications. Sig Transduct Target Ther *5*, 1–12.

Kaiser, C.M., Goldman, D.H., Chodera, J.D., Tinoco, I., and Bustamante, C. (2011). The Ribosome Modulates Nascent Protein Folding. Science *334*, 1723–1727.

Käll, L., Canterbury, J.D., Weston, J., Noble, W.S., and MacCoss, M.J. (2007). Semi-supervised learning for peptide identification from shotgun proteomics datasets. Nat Methods *4*, 923–925.

Kang, L., Moriarty, G.M., Woods, L.A., Ashcroft, A.E., Radford, S.E., and Baum, J. (2012). N-terminal acetylation of α-synuclein induces increased transient helical propensity and decreased aggregation rates in the intrinsically disordered monomer. Protein Science *21*, 911–917.

Karamyshev, A.L., Karamysheva, Z.N., Kajava, A.V., Ksenzenko, V.N., and Nesmeyanova, M.A. (1998). Processing of Escherichia coli alkaline phosphatase: role of the primary structure of the signal peptide cleavage region. Journal of Molecular Biology *277*, 859–870.

Kern, S.E., Price-Whelan, A., and Newman, D.K. (2014). Extraction and Measurement of NAD(P)+ and NAD(P)H. In Pseudomonas Methods and Protocols, A. Filloux, and J.-L. Ramos, eds. (New York, NY: Springer New York), pp. 311–323.

Kim, J.H., Krahn, J.M., Tomchick, D.R., Smith, J.L., and Zalkin, H. (1996). Structure and Function of the Glutamine Phosphoribosylpyrophosphate Amidotransferase Glutamine Site and Communication with the Phosphoribosylpyrophosphate Site. J. Biol. Chem. *271*, 15549–15557.

Kim, J.-M., Seok, O.-H., Ju, S., Heo, J.-E., Yeom, J., Kim, D.-S., Yoo, J.-Y., Varshavsky, A., Lee, C., and Hwang, C.-S. (2018). Formyl-methionine as an N-degron of a eukaryotic N-end rule pathway. Science eaat0174.

Koubek, J., Schmitt, J., Galmozzi, C.V., and Kramer, G. (2021). Mechanisms of Cotranslational Protein Maturation in Bacteria. Front. Mol. Biosci. *8*, 689755.

Kramer, G., Boehringer, D., Ban, N., and Bukau, B. (2009). The ribosome as a platform for co-translational processing, folding and targeting of newly synthesized proteins. Nat Struct Mol Biol *16*, 589–597.

Kramer, G., Shiber, A., and Bukau, B. (2019). Mechanisms of Cotranslational Maturation of Newly Synthesized Proteins. Annu. Rev. Biochem. *88*, 337–364.

Krulwich, T.A., Sachs, G., and Padan, E. (2011). Molecular aspects of bacterial pH sensing and homeostasis. Nat Rev Microbiol *9*, 330–343.

Kyte, J., and Doolittle, R.F. (1982). A simple method for displaying the hydropathic character of a protein. Journal of Molecular Biology *157*, 105–132.

Lal, R., Lin, H., and Quist, A.P. (2007). Amyloid beta ion channel: 3D structure and relevance to amyloid channel paradigm. Biochimica et Biophysica Acta (BBA) - Biomembranes *1768*, 1966–1975.

Larsen, T.M., Boehlein, S.K., Schuster, S.M., Richards, N.G.J., Thoden, J.B., Holden, H.M., and Rayment, I. (1999). Three-Dimensional Structure of Escherichia coli Asparagine Synthetase B: A Short Journey from Substrate to Product,. Biochemistry *38*, 16146–16157.

Leonhartsberger, S., Korsa, I., and Böck, A. (2002). The molecular biology of formate metabolism in enterobacteria. J Mol Microbiol Biotechnol *4*, 269–276.

Li, X., and Chang, Y.H. (1995). Amino-terminal protein processing in Saccharomyces cerevisiae is an essential function that requires two distinct methionine aminopeptidases. PNAS *92*, 12357–12361.

Li, C., Wen, A., Shen, B., Lu, J., Huang, Y., and Chang, Y. (2011). FastCloning: a highly simplified, purification-free, sequence- and ligation-independent PCR cloning method. BMC Biotechnol. *11*, 92.

Lowther, W.T., Zhang, Y., Sampson, P.B., Honek, J.F., and Matthews, B.W. (1999). Insights into the mechanism of Escherichia coli methionine aminopeptidase from the structural analysis of reaction products and phosphorus-based transition-state analogues. Biochemistry *38*, 14810–14819.

Lu, J., and Deutsch, C. (2008). Electrostatics in the Ribosomal Tunnel Modulate Chain Elongation Rates. Journal of Molecular Biology *384*, 73–86.

Margolis, P.S., Hackbarth, C.J., Young, D.C., Wang, W., Chen, D., Yuan, Z., White, R., and Trias, J. (2000). Peptide Deformylase in Staphylococcus aureus: Resistance to Inhibition Is Mediated by Mutations in the Formyltransferase Gene. Antimicrobial Agents and Chemotherapy *44*, 1825–1831.

Martinez, A., Traverso, J.A., Valot, B., Ferro, M., Espagne, C., Ephritikhine, G., Zivy, M., Giglione, C., and Meinnel, T. (2008). Extent of N-terminal modifications in cytosolic proteins from eukaryotes. Proteomics *8*, 2809–2831.

Masip, L., Veeravalli, K., and Georgiou, G. (2006). The Many Faces of Glutathione in Bacteria. Antioxidants & Redox Signaling *8*, 753–762.

Mazel, D., Pochet, S., and Marliere, P. (1994). Genetic characterization of polypeptide deformylase, a distinctive enzyme of eubacterial translation. The EMBO Journal *13*, 914–923.

Meinnel, T., and Giglione, C. (2008). Tools for analyzing and predicting N-terminal protein modifications. Proteomics *8*, 626–649.

Meinnel, T., Mechulam, Y., and Blanquet, S. (1993). Methionine as translation start signal: a review of the enzymes of the pathway in Escherichia coli. Biochimie *75*, 1061–1075.

Merz, F., Boehringer, D., Schaffitzel, C., Preissler, S., Hoffmann, A., Maier, T., Rutkowska, A., Lozza, J., Ban, N., Bukau, B., et al. (2008). Molecular mechanism and structure of Trigger Factor bound to the translating ribosome. EMBO J. *27*, 1622–1632.

Milligan, D.L., and Koshland Jr, D.E. (1990). The amino terminus of the aspartate chemoreceptor is formylmethionine. Journal of Biological Chemistry *265*, 4455–4460.

Moffatt, B.A., and Ashihara, H. (2002). Purine and Pyrimidine Nucleotide Synthesis and Metabolism. Arabidopsis Book *1*, e0018.

Mohammad, F., and Buskirk, A. (2019). Protocol for Ribosome Profiling in Bacteria. BIO-PROTOCOL *9*.

Mouilleron, S., Badet-Denisot, M.-A., and Golinelli-Pimpaneau, B. (2006). Glutamine binding opens the ammonia channel and activates glucosamine-6P synthase. J Biol Chem *281*, 4404–4412.

Muñoz, V., and Serrano, L. (1995). Elucidating the Folding Problem of Helical Peptides using Empirical Parameters. II. Helix Macrodipole Effects and Rational Modification of the Helical Content of Natural Peptides. Journal of Molecular Biology *245*, 275–296.

Nguyen, K.T., Kim, J.-M., Park, S.-E., and Hwang, C.-S. (2019). N-terminal methionine excision of proteins creates tertiary destabilizing N-degrons of the Arg/N-end rule pathway. J. Biol. Chem. *294*, 4464–4476.

Ninnis, R.L., Spall, S.K., Talbo, G.H., Truscott, K.N., and Dougan, D.A. (2009). Modification of PATase by L/F-transferase generates a ClpS-dependent N-end rule substrate in Escherichia coli.

Norrander, J., Kempe, T., and Messing, J. (1983). Construction of improved M13 vectors using oligodeoxynucleotide-directed mutagenesis. Gene *26*, 101–106.

Novo, D., Perlmutter, N.G., Hunt, R.H., and Shapiro, H.M. (1999). Accurate flow cytometric membrane potential measurement in bacteria using diethyloxacarbocyanine and a ratiometric technique. Cytometry *35*, 55–63.

O'Brien, E.P., Vendruscolo, M., and Dobson, C.M. (2012). Prediction of variable translation rate effects on cotranslational protein folding. Nat Commun *3*, 868.

O'Brien, E.P., Vendruscolo, M., and Dobson, C.M. (2014). Kinetic modelling indicates that fast-translating codons can coordinate cotranslational protein folding by avoiding misfolded intermediates. Nat Commun *5*, 2988.

Oh, E., Becker, A.H., Sandikci, A., Huber, D., Chaba, R., Gloge, F., Nichols, R.J., Typas, A., Gross, C.A., Kramer, G., et al. (2011). Selective ribosome profiling reveals the cotranslational chaperone action of trigger factor in vivo. Cell *147*, 1295–1308.

Oinonen, C., and Rouvinen, J. (2000). Structural comparison of Ntn-hydrolases. Protein Sci *9*, 2329–2337.

Oizel, K., Tait-Mulder, J., Fernandez-de-Cossio-Diaz, J., Pietzke, M., Brunton, H., Lilla, S., Dhayade, S., Athineos, D., Blanco, G.R., Sumpton, D., et al. (2020). Formate induces a metabolic switch in nucleotide and energy metabolism. Cell Death Dis *11*, 1–14.

Okura, A., Kinoshita, T., and Tanaka, N. (1971). Formation of fusidic acid-G factor-GDP-ribosome complex and the relationship to the inhibition of GTP hydrolysis. J. Antibiot. *24*, 655–661.

Old, I.G., Phillips, S.E.V., Stockley, P.G., and Saint Girons, I. (1991). Regulation of methionine biosynthesis in the enterobacteriaceae. Progress in Biophysics and Molecular Biology *56*, 145–185.

Orsburn, B.C. (2021). Proteome Discoverer—A Community Enhanced Data Processing Suite for Protein Informatics. Proteomes *9*, 15.

Padan, E., Bibi, E., Ito, M., and Krulwich, T.A. (2005). Alkaline pH homeostasis in bacteria: New insights. Biochimica et Biophysica Acta (BBA) - Biomembranes *1717*, 67–88.

Park, E., Lee, J.W., Eom, S.H., Seol, J.H., and Chung, C.H. (2008). Binding of MG132 or Deletion of the Thr Active Sites in HslV Subunits Increases the Affinity of HslV Protease for HslU ATPase and Makes This Interaction Nucleotide-independent*. Journal of Biological Chemistry *283*, 33258–33266.

Patzelt, H., Rüdiger, S., Brehmer, D., Kramer, G., Vorderwülbecke, S., Schaffitzel, E., Waitz, A., Hesterkamp, T., Dong, L., Schneider-Mergener, J., et al. (2001). Binding specificity of Escherichia coli trigger factor. Proc. Natl. Acad. Sci. U.S.A. *98*, 14244–14249.

Peluso, P., Shan, S.O., Nock, S., Herschlag, D., and Walter, P. (2001). Role of SRP RNA in the GTPase cycles of Ffh and FtsY. Biochemistry *40*, 15224–15233.

Peterson, J.H., Szabady, R.L., and Bernstein, H.D. (2006). An unusual signal peptide extension inhibits the binding of bacterial presecretory proteins to the signal recognition particle, trigger factor, and the SecYEG complex. The Journal of Biological Chemistry *281*, 9038–9048.

Peterson, J.H., Woolhead, C.A., and Bernstein, H.D. (2010). The conformation of a nascent polypeptide inside the ribosome tunnel affects protein targeting and protein folding. Molecular Microbiology *78*, 203–217.

Piatkov, K.I., Vu, T.T.M., Hwang, C.-S., and Varshavsky, A. (2015). Formyl-methionine as a degradation signal at the N-termini of bacterial proteins. Microb Cell *2*, 376–393.

Ping, L., Zhang, H., Zhai, L., Dammer, E.B., Duong, D.M., Li, N., Yan, Z., Wu, J., and Xu, P. (2013). Quantitative Proteomics Reveals Significant Changes in Cell Shape and an Energy Shift after IPTG Induction via an Optimized SILAC Approach for Escherichia coli. J. Proteome Res. *12*, 5978–5988.

Prindle, A., Liu, J., Asally, M., Ly, S., Garcia-Ojalvo, J., and Süel, G.M. (2015). Ion channels enable electrical communication in bacterial communities. Nature *527*, 59–63.

R Core Team (2018). R: A language and environment for statistical computing (R Foundation for Statistical Computing, Vienna, Austria).

Ragusa, S., Blanquet, S., and Meinnel, T. (1998). Control of peptide deformylase activity by metal cations. J. Mol. Biol. *280*, 515–523.

Ragusa, S., Mouchet, P., Lazennec, C., Dive, V., and Meinnel, T. (1999). Substrate recognition and selectivity of peptide deformylase. Similarities and differences with metzincins and thermolysin. J. Mol. Biol. *289*, 1445–1457.

Rajagopalan, P.T.R., Grimme, S., and Pei, D. (2000). Characterization of Cobalt(II)-Substituted Peptide Deformylase: Function of the Metal Ion and the Catalytic Residue Glu-133.

Ranjan, A., Mercier, E., Bhatt, A., and Wintermeyer, W. (2017). Signal recognition particle prevents N-terminal processing of bacterial membrane proteins. Nat Commun *8*, 15562.

Raue, U., Oellerer, S., and Rospert, S. (2007). Association of Protein Biogenesis Factors at the Yeast Ribosomal Tunnel Exit Is Affected by the Translational Status and Nascent Polypeptide Sequence. J. Biol. Chem. *282*, 7809–7816.

Rawat, S., Zhu, L., Lindner, E., Dalbey, R.E., and White, S.H. (2015). SecA drives transmembrane insertion of RodZ, an unusual single-span membrane protein. J. Mol. Biol. *427*, 1023–1037.

Ritchie, M.E., Phipson, B., Wu, D., Hu, Y., Law, C.W., Shi, W., and Smyth, G.K. (2015). limma powers differential expression analyses for RNA-sequencing and microarray studies. Nucleic Acids Research *43*, e47.

Rodnina, M.V. (2016). The ribosome in action: Tuning of translational efficiency and protein folding. Protein Sci *25*, 1390–1406.

Rohrwild, M., Coux, O., Huang, H.C., Moerschell, R.P., Yoo, S.J., Seol, J.H., Chung, C.H., and Goldberg, A.L. (1996). HslV-HslU: A novel ATP-dependent protease complex in Escherichia coli related to the eukaryotic proteasome. Proceedings of the National Academy of Sciences *93*, 5808–5813.

Saio, T., Guan, X., Rossi, P., Economou, A., and Kalodimos, C.G. (2014). Structural Basis for Protein Antiaggregation Activity of the Trigger Factor Chaperone. Science *344*, 1250494.

Sandikci, A., Gloge, F., Martinez, M., Mayer, M.P., Wade, R., Bukau, B., and Kramer, G. (2013). Dynamic enzyme docking to the ribosome coordinates N-terminal processing with polypeptide folding. Nat. Struct. Mol. Biol. *20*, 843–850.

Saraogi, I., Zhang, D., Chandrasekaran, S., and Shan, S.O. (2011). Site-specific fluorescent labeling of nascent proteins on the translating ribosome. J. Am. Chem. Soc. *133*, 14936–14939.

Schaffitzel, C., and Ban, N. (2007). Generation of ribosome nascent chain complexes for structural and functional studies. J Struct Biol *158*, 463–471.

Schaffitzel, C., Oswald, M., Berger, I., Ishikawa, T., Abrahams, J.P., Koerten, H.K., Koning, R.I., and Ban, N. (2006). Structure of the E. coli signal recognition particle bound to a translating ribosome. Nature *444*, 503–506.

Schibich, D., Gloge, F., Pohner, I., Bjorkholm, P., Wade, R.C., von Heijne, G., Bukau, B., and Kramer, G. (2016). Global profiling of SRP interaction with nascent polypeptides. Nature *536*, 219–223.

Schmidt, R., Zahn, R., Bukau, B., and Mogk, A. (2009). ClpS is the recognition component for Escherichia coli substrates of the N-end rule degradation pathway. Mol Microbiol *72*, 506–517.

Schuwirth, B.S., Borovinskaya, M.A., Hau, C.W., Zhang, W., Vila-Sanjurjo, A., Holton, J.M., and Cate, J.H.D. (2005). Structures of the Bacterial Ribosome at 3.5 Å Resolution. Science *310*, 827–834.

Sciacca, M.F.M., Kotler, S.A., Brender, J.R., Chen, J., Lee, D., and Ramamoorthy, A. (2012). Two-Step Mechanism of Membrane Disruption by Aβ through Membrane Fragmentation and Pore Formation. Biophysical Journal *103*, 702–710.

Sciacca, M.F.M., La Rosa, C., and Milardi, D. (2021). Amyloid-Mediated Mechanisms of Membrane Disruption. Biophysica *1*, 137–156.

Scott, D.C., Monda, J.K., Bennett, E.J., Harper, J.W., and Schulman, B.A. (2011). N-Terminal Acetylation Acts as an Avidity Enhancer Within an Interconnected Multiprotein Complex. Science *334*, 674–678.

Sebald, W., and Wachter, E. (1980). Amino acid sequence of the proteolipid subunit of the ATP synthase from spinach chloroplasts. FEBS Letters *122*, 307–311.

Seip, B., and Innis, C.A. (2016). How Widespread is Metabolite Sensing by Ribosome-Arresting Nascent Peptides? J. Mol. Biol. *428*, 2217–2227.

Shemorry, A., Hwang, C.-S., and Varshavsky, A. (2013). Control of Protein Quality and Stoichiometries by N-Terminal Acetylation and the N-End Rule Pathway. Mol. Cell *50*, 540–551.

Singer, J.M., and Shaw, J.M. (2003). Mdm20 protein functions with Nat3 protein to acetylate Tpm1 protein and regulate tropomyosin–actin interactions in budding yeast. PNAS *100*, 7644–7649.

Singer, M., Baker, T.A., Schnitzler, G., Deischel, S.M., Goel, M., Dove, W., Jaacks, K.J., Grossman, A.D., Erickson, J.W., and Gross, C.A. (1989). A collection of strains containing genetically linked alternating antibiotic resistance elements for genetic mapping of Escherichia coli. Microbiology and Molecular Biology Reviews *53*, 1–24.

Singh, D., Majumdar, A.G., Gamre, S., and Subramanian, M. (2021). Membrane damage precedes DNA damage in hydroxychavicol treated E. coli cells and facilitates cooperativity with hydrophobic antibiotics. Biochimie *180*, 158–168.

Singh, R., Kraft, C., Jaiswal, R., Sejwal, K., Kasaragod, V.B., Kuper, J., Burger, J., Mielke, T., Luirink, J., and Bhushan, S. (2014). Cryo-electron microscopic structure of SecA protein bound to the 70S ribosome. J. Biol. Chem. *289*, 7190–7199.

Solbiati, J., Chapman-Smith, A., Miller, J.L., Miller, C.G., and Cronan, J.E., Jr. (1999). Processing of the N termini of nascent polypeptide chains requires deformylation prior to methionine removal. J. Mol. Biol. *290*, 607–614.

Somerville, G.A., Cockayne, A., Dürr, M., Peschel, A., Otto, M., and Musser, J.M. (2003). Synthesis and Deformylation of Staphylococcus aureus δ-Toxin Are Linked to Tricarboxylic Acid Cycle Activity. J. Bacteriol. *185*, 6686–6694.

Spaans, S.K., Weusthuis, R.A., van der Oost, J., and Kengen, S.W.M. (2015). NADPH-generating systems in bacteria and archaea. Frontiers in Microbiology *6*.

Stocks, S.M. (2004). Mechanism and use of the commercially available viability stain, BacLight. Cytometry Part A *61A*, 189–195.

Sträuber, H., and Müller, S. (2010). Viability states of bacteria—Specific mechanisms of selected probes. Cytometry Part A *77A*, 623–634.

Sundari, R.M., Stringer, E.A., Schulman, L.H., and Maitra, U. (1976). Interaction of bacterial initiation factor 2 with initiator tRNA. J. Biol. Chem. *251*, 3338–3345.

Tabb, D.L. (2015). The SEQUEST Family Tree. J Am Soc Mass Spectrom *26*, 1814–1819.

Tanka, S., Matsushita, Y., Yoshikawa, A., and Isono, K. (1989). Cloning and molecular characterization of the generimL wich encodes an enzyme acetylating ribosomal protein L12 ofEscherichia coki K12. Molec. Gen. Genet. *217*, 289–293.

Thommen, M., Holtkamp, W., and Rodnina, M.V. (2017). Co-translational protein folding: progress and methods. Current Opinion in Structural Biology *42*, 83–89.

Tobias, J.W., Shrader, T.E., Rocap, G., and Varshavsky, A. (1991). The N-end rule in bacteria. Science *254*, 1374–1377.

Tomoyasu, T., Mogk, A., Langen, H., Goloubinoff, P., and Bukau, B. (2001). Genetic dissection of the roles of chaperones and proteases in protein folding and degradation in the Escherichia coli cytosol. Molecular Microbiology *40*, 397–413.

Tyanova, S., Temu, T., Sinitcyn, P., Carlson, A., Hein, M.Y., Geiger, T., Mann, M., and Cox, J. (2016). The Perseus computational platform for comprehensive analysis of (prote)omics data. Nature Methods *13*, 731–740.

Ullers, R.S., Houben, E.N.G., Raine, A., ten Hagen-Jongman, C.M., Ehrenberg, M., Brunner, J., Oudega, B., Harms, N., and Luirink, J. (2003). Interplay of signal recognition particle and trigger factor at L23 near the nascent chain exit site on the Escherichia coli ribosome. J Cell Biol *161*, 679–684.

Underwood, K.A., Swartz, J.R., and Puglisi, J.D. (2005). Quantitative polysome analysis identifies limitations in bacterial cell-free protein synthesis. Biotechnol. Bioeng. *91*, 425–435.

The UniProt Consortium (2017). UniProt: the universal protein knowledgebase. Nucleic Acids Research *45*, D158–D169.

Valent, Q.A., Kendall, D.A., High, S., Kusters, R., Oudega, B., and Luirink, J. (1995). Early events in preprotein recognition in E. coli: interaction of SRP and trigger factor with nascent polypeptides. EMBO J *14*, 5494–5505.

Van Aller, G.S., Nandigama, R., Petit, C.M., DeWolf, W.E., Jr., Quinn, C.J., Aubart, K.M., Zalacain, M., Christensen, S.B., Copeland, R.A., and Lai, Z. (2005). Mechanism of time-dependent inhibition of polypeptide deformylase by actinonin. Biochemistry *44*, 253–260.

Varshavsky, A. (2011). The N-end rule pathway and regulation by proteolysis. Protein Sci. *20*, 1298–1345.

Varshavsky, A. (2019). N-degron and C-degron pathways of protein degradation. Proc. Natl. Acad. Sci. U.S.A. *116*, 358–366.

vonHeijne, G. (1989). Control of topology and mode of assembly of a polytopic membrane protein by positively charged residues. Nature *341*, 456–458.

Wang, S., Yang, C.-I., and Shan, S. (2017). SecA mediates cotranslational targeting and translocation of an inner membrane protein. J. Cell Biol. *216*, 3639–3653.

Wang, S., Jomaa, A., Jaskolowski, M., Yang, C.-I., Ban, N., and Shan, S. (2019). The molecular mechanism of cotranslational membrane protein recognition and targeting by SecA. Nat Struct Mol Biol *26*, 919–929.

Watterson, S.J., Mitra, S., Swierczek, S.I., Bennett, B., and Holz, R.C. (2008). Kinetic and spectroscopic analysis of the catalytic role of H79 in the methionine aminopeptidase from Escherichia coli. Biochemistry *47*, 11885–11893.

Waudby, C.A., Dobson, C.M., and Christodoulou, J. (2019). Nature and Regulation of Protein Folding on the Ribosome. Trends in Biochemical Sciences *44*, 914–926.

Welle, K.A., Zhang, T., Hryhorenko, J.R., Shen, S., Qu, J., and Ghaemmaghami, S. (2016). Time-resolved Analysis of Proteome Dynamics by Tandem Mass Tags and Stable Isotope Labeling in Cell Culture (TMT-SILAC) Hyperplexing. Molecular & Cellular Proteomics *15*, 3551–3563.

Wilkins, J.C., Homer, K.A., and Beighton, D. (2001). Altered Protein Expression of Streptococcus oralis Cultured at Low pH Revealed by Two-Dimensional Gel Electrophoresis. Appl. Environ. Microbiol. *67*, 3396–3405.

Xiao, Q., Zhang, F., Nacev, B.A., Liu, J.O., and Pei, D. (2010). Protein N-terminal processing: substrate specificity of Escherichia coli and human methionine aminopeptidases. Biochemistry *49*, 5588–5599.

Yang, C.-I., Hsieh, H.-H., and Shan, S. (2019). Timing and specificity of cotranslational nascent protein modification in bacteria. Proc. Natl. Acad. Sci. U.S.A. *116*, 23050–23060.

Yap, M.-N., and Bernstein, H.D. (2009). The Plasticity of a Translation Arrest Motif Yields Insights into Nascent Polypeptide Recognition inside the Ribosome Tunnel. Mol. Cell *34*, 201–211.

Yin, J., Straight, P.D., McLoughlin, S.M., Zhou, Z., Lin, A.J., Golan, D.E., Kelleher, N.L., Kolter, R., and Walsh, C.T. (2005). Genetically encoded short peptide tag for versatile protein labeling by Sfp phosphopantetheinyl transferase. Proc Natl Acad Sci U S A *102*, 15815–15820.

Yoo, S.J., Shim, Y.K., Seong, I.S., Seol, J.H., Kang, M.-S., and Chung, C.H. (1997). Mutagenesis of two N-terminal Thr and five Ser residues in HslV, the proteolytic component of the ATP-dependent HslVU protease. FEBS Letters *412*, 57–60.

Yoshikawa, A., Isono, S., Sheback, A., and Isono, K. (1987). Cloning and nucleotide sequencing of the genes rimI and rimJ which encode enzymes acetylating ribosomal proteins S18 and S5 of Escherichia coli K12. Mol Gen Genet *209*, 481–488.

Zhang, D., Sweredoski, M.J., Graham, R.L., Hess, S., and Shan, S.O. (2012). Novel proteomic tools reveal essential roles of SRP and importance of proper membrane protein biogenesis. Molecular & Cellular Proteomics : MCP *11*, M111.011585.

Zhang, J., Kobert, K., Flouri, T., and Stamatakis, A. (2014). PEAR: a fast and accurate Illumina Paired-End reAd mergeR. Bioinformatics *30*, 614–620.

A p p e n d i x

SUPPLEMENTARY INFORMATION FOR CHAPTER 4

Note: Datasets are attached as individual .xlsx files.

Dataset 1. List of quantified and differentially expressed proteins in the proteomic experiment.

The log2(FC) values of quantified proteins at each time point relative to 0 h are reported. P-values, adjusted p-values and significance of differentially expressed proteins were calculated as described in Methods, with thresholds of $|log2FC| \geq 0.5$ at 1.5 h and $|log2FC| \geq 1$ at 4.5/9 h (adjusted $p \leq 0.05$). Functional annotations and other gene-specific information were extracted from Uniprot.

Dataset 2. DAVID analysis of the differentially expressed proteins upon PDF inhibition in the proteomic experiment.

Outputs of the DAVID functional annotation clustering on the up- or down-regulated proteins at 1.5, 4.5, or 9h after PDF inhibition. The P-value for individual term was computed using a modified Fisher's exact test, and the terms were clustered based on their similarity. Clusters with enrichment scores ≥ 1.3 are considered significant and shaded in green.

Dataset 3. List of quantified and differentially expressed genes in the ribosome profiling experiment.

The log2(FC) values of quantified genes at each time point of ACT treatment relative to those in the –ACT sample are reported. P-values and significance for differential expressed genes were determined as described in Methods, with thresholds of $|log2FC| \geq 1$ and $p < 0.05$. Functional annotations and other gene-specific information were extracted from Uniprot.

Dataset 4. DAVID analysis of the differentially expressed proteins upon PDF inhibition in the ribosome profiling experiment.

Outputs of the DAVID functional annotation clustering on the up- or down-regulated proteins at 0.25, 0.5 or 1.5 h after PDF inhibition. The P-value for individual term was computed using a modified Fisher's exact test, and the terms were clustered based on their similarity. Clusters with enrichment scores ≥ 1.3 are considered significant and shaded in green.